AN ABSTRACT OF THE DISSERTATION OF

Brandy T. Cervantes for the degree of Doctor of Philosophy in Oceanography presented on December 3, 2004.

Title: Numerical Model Investigations of Wind-driven Coastal Circulation.

Redacted for Privacy

Abstract approved: _____

John S. Allen

The effects of wind forcing on coastal ocean circulation are studied using a numerical modeling approach. The first region of interest is on the North Carolina shelf, where the Coastal Ocean Processes (CoOP) Inner Shelf Study (ISS) took place during August – November 1994. ISS observations are used to initialize, force, and compare results from a two-dimensional version (variations across-shore and with depth; uniformity alongshore) of the primitive equation Princeton Ocean Model. Both strongly stratified and weakly stratified conditions, found during August and October, respectively, are studied. An additional difference between these two periods is that August is characterized by fluctuating alongshelf winds, while October is dominated by downwelling-favorable winds. Momentum term balances, across-shelf transport values, and Lagrangian dynamics are contrasted for the August and October periods. The nonlinear advection terms contribute significantly to the alongshelf momentum balance in depths less than 10 m during upwelling, but not during downwelling.

This result regarding the asymmetry in the shelf response during upwelling and downwelling motivates further study in this region using the same model setup with forcing by periodic alongshelf wind stress. This periodicity allows further investigation of the upwelling-downwelling asymmetries and the Lagrangian characteristics of the flow. An important result of the asymmetric upwelling and downwelling responses is a non-zero mean Eulerian and Lagrangian velocity over the forcing period. These mean velocities differ, leading to a mean Stokes velocity that is largest in the complex region near the coast where parcel trajectories are irregular. A Lagrangian mapping technique and calculation of the largest Lyapunov exponent help identify the nature of fluid parcel displacements over many periods.

Focus of the modeling effort then shifts to the region of the northern California shelf, where the CoOP Wind Events and Shelf Transport (WEST) program collected measurements during January 2000 – May 2003. The three-dimensional Regional Ocean Modeling System (ROMS) primitive equation model is initialized and forced with WEST observations, and extensive model-data comparisons are made with three WEST datasets. The model compares reasonably well with moored velocity measurements, CODAR surface current observations, and shipboard hydrographic measurements. The mean response over the summer period is dominated by an upwelling circulation, including a coastal jet that separates off Pt. Arena and Pt. Reyes. Flow near Pt. Reyes during an upwelling and relaxation wind event is complicated and the response north and south of the cape is quite different. Lagrangian results reveal that the source of upwelled water near the coast south of Pt. Reyes is local, as compared to that north of Pt. Reyes, which has a signature of deeper water from farther north. Momentum term balances help to clarify the event

dynamics as a function of shelf location. The Lagrangian analyses include both a parcel tracking and label advection technique and provide detailed information on the upwelling response of fluid parcels on the shelf.

©Copyright by Brandy T. Cervantes

December 3, 2004

All Rights Reserved

Numerical Model Investigations of Wind-driven Coastal Circulation

by

Brandy T. Cervantes

A DISSERTATION

submitted to

Oregon State University

in partial fulfillment of
the requirements for the
degree of

Doctor of Philosophy

Presented December 3, 2004
Commencement June 2005

Doctor of Philosophy dissertation of Brandy T. Cervantes presented on December 3, 2004.

APPROVED:

Redacted for Privacy

Major Professor, representing Oceanography

Redacted for Privacy

Dean of the College of Oceanic and Atmospheric Sciences

Redacted for Privacy

Dean of the Graduate School

I understand that my dissertation will become part of the permanent collection of Oregon State University libraries. My signature below authorizes release of my dissertation to any reader upon request.

Redacted for Privacy

Brandy T. Cervantes, Author

ACKNOWLEDGMENTS

I would like to thank my advisor John Allen for providing me with excellent scientific guidance throughout my graduate school career. I also thank the members of my committee John A. Barth, Robert N. Miller, Roger Samelson, Rob Holman, and the graduate representative Todd S. Palmer.

Countless people have assisted in this effort by answering my many questions. Priscilla Newberger's expertise of the Princeton Ocean Model was extremely helpful, as was Scott Durski's knowledge of the Regional Ocean Modeling System. I also thank others who were always available to help out with a science, modeling, or programming discussion, including Paul Choboter, Mike Whitney, Alexander Kurapov, Renellys Perez, Jay Austin, and Peter Oke.

Murray Levine greatly enriched my COAS experience by letting me tag along on research cruises, serve as teaching assistant for his physical oceanography class, and attend official business lunches at American Dream Pizza. Irma Delson provided an invaluable service to students during her tenure as Director of Student Programs, and continues to be a very dear friend.

The friendships I formed while at COAS made my graduate experience incredibly rich, and I could not ask for a more supportive group than Renellys Perez, Jennifer Simeon, James Wheeler, Debbie Colbert, Sheila O'Keefe, Cidney Howard, Leah Bandstra, Brian Haley, and Nicolai Thum. Special thanks to Renellys Perez who, when all our other first-year cronies were gone, was there to give great advice over a tea.

Also incredibly important is the support system of my family. I thank my parents, Mike and Sara Kuebel, who always have encouraging words and never fail

to tell me they are proud of my accomplishments. My husband, Darren, has been all I could have ever hoped for in a partner, and his unfailing support never ceases to amaze me. I also thank our wonderful dogs, Diego and Max, who helped me get through stressful times just by making me laugh.

This work was supported by the Office of Naval Research (ONR) Coastal Dynamics Program through Grants N00014-93-1-1301 and N00014-02-1-0100 and the National Science Foundation Coastal Ocean Processes (CoOP) program under grant OCE-9907854.

CONTRIBUTION OF AUTHORS

Dr. Roger Samelson contributed scientific input and writing suggestions for Chapters 2 and 3.

TABLE OF CONTENTS

TABLE OF CONTENTS (Continued)

TABLE OF CONTENTS (Continued)

LIST OF FIGURES

LIST OF FIGURES (Continued)

LIST OF FIGURES (Continued)

LIST OF FIGURES (Continued)

LIST OF FIGURES (Continued)

LIST OF FIGURES (Continued)

LIST OF FIGURES (Continued)

LIST OF FIGURES (Continued)

LIST OF TABLES

Numerical Model Investigations of Wind-driven Coastal Circulation

1 Introduction

Wind forcing is of primary importance in the coastal ocean, the region of the oceanic continental margins and their slope toward the deep ocean. The coastal ocean closely impacts the large number of global inhabitants of coastal regions, economically affecting the industries of fishing, tourism, and recreation. Hence, coastal oceanography has long been an important topic in the field of oceanography. Because coastal regions are easily accessible for study, many large-scale observational programs have taken place off the eastern and western coasts of North America in recent decades. Two such programs, the Coastal Ocean Processes (CoOP) Inner Shelf Study (ISS) off North Carolina and the CoOP Wind Events and Shelf Transport (WEST) off Northern California, will be discussed in detail in connection to the modeling efforts of this dissertation.

In recent years, a significant increase in the use of numerical models in studies of the coastal ocean has occurred. The ability of models to reveal characteristics of flows that may be difficult to determine from observations is clearly advantageous, despite recognized imperfections in the models and their output. Application of the widely-used primitive equation Princeton Ocean Model to the coastal ocean for idealized studies of two-dimensional wind-driven upwelling and downwelling was first presented in Allen et al. (1995) Federiuk and Allen (1995) Allen and Newberger (1996) and later by Austin (1998) and Austin and Lentz (2002). These

studies argued that the wind-driven shelf flows in the regions of interest (Oregon and North Carolina, respectively) are sufficiently homogeneous along the shelf and that a two-dimensional model (variations across-shelf and with depth) can describe reasonably well the circulation associated with upwelling and downwelling. They also served as a useful starting point for model studies of more complex three-dimensional coastal flows.

Chapter 2 is an extension of the idealized modeling study of Austin (1998) and Austin and Lentz (2002) for the region of the CoOP ISS off Duck, North Carolina to include realistic model bathymetry, initial stratification, and forcing by observed winds and heat flux components followed by direct model/data comparisons. The ISS had the interdisciplinary goal of quantifying across-shelf transport and its impact on the planktonic larvae of inner-shelf benthic invertebrates (Austin, 1998). Therefore, an across-shelf array of sensors collected time series during August – November 1994 (Butman, 1994). The model domain selected for this study is given by this same two-dimensional section to allow for quantitative model-data comparisons.

Following the analysis of observed and modeled fields from an Eulerian perspective, the Lagrangian flow characteristics are also discussed. Although there is a natural interest in the behavior of fluid parcels in coastal flows, specifically in relation to physical forcing effects on biology, analysis of coastal models have traditionally not focused on this perspective. It is a complicated problem, but one that is approached in this work using two different techniques. The first method implements existing particle-tracking techniques as done, for example, by Chen and Beardsley (1998). In addition, we use an alternate method of advecting Lagrangian label fields by model velocities and make direct comparisons of the

modeled parcel tracks from the two techniques. The Lagrangian analysis of modeled flows is introduced in Chapter 2 with forcing by observed ISS winds and extended in Chapter 3 for the case of periodic wind stress forcing over short and long time scales. The work presented in Chapter 3 was motivated by asymmetries discovered in the upwelling and downwelling response during periods of fluctuating winds discussed in Chapter 2. Periodic forcing allows for the application of more detailed Lagrangian analysis tools, including a mapping technique for advecting the parcels over many forcing periods and calculation of the largest Lyapunov exponent.

While a two-dimensional approximation for the study of upwelling and downwelling circulation is appropriate for some coastal regions, the application of a full three-dimensional model necessarily includes more dynamics and is useful in areas with significant alongshelf variability, such as the northern California shelf. This region has been the focus of several large observational programs, including the Coastal Ocean Dynamics Experiment (CODE) (Beardsley and Lentz, 1987), Northern California Coastal Circulation Study (NCCCS) (Bray and Greengrove, 1993), Shelf Mixed Layer Experiment (SMILE) (Alessi et al., 1991), Coastal Transition Zone Experiment (CTZ) (Brink and Cowles, 1991), and most recently the CoOP WEST program. The shelf between Pt. Reyes and Pt. Arena experiences the strongest summer upwelling winds along the US west coast (Dorman and Winant, 1995). Interesting dynamics also result due to the region being bounded at the north and south by capes, especially the prominent cape of Pt. Reyes, which has been shown to experience poleward flow nearshore during relaxation from upwelling winds (Send et al., 1987) that is important in transporting larvae of benthic invertebrates northward from the Gulf of Farallones (Wing et al., 1995).

The goal of Chapter 4 is to document the Eulerian and Lagrangian analyses conducted using a three-dimensional numerical model developed in support of the WEST program. Specific topics of interest that address WEST objectives include the flow variability along and across the shelf, the behavior of the complex flow around Pt. Reyes, and the source and fate of upwelled water. The period of the modeling study is May–June 2001, during which WEST measurements, including shipboard hydrographic surveys, CODAR surface velocities, and moored temperature and velocity time series, are available. Quantitative comparisons of the model output with the WEST observations are made and generalizations of the summer upwelling period are presented with time-averaged model fields. The analyses of the time-variable aspects of the flow focus on the response to a particular wind event beginning with upwelling-favorable winds that relax to near zero.

2 A Modeling Study of Eulerian and Lagrangian Aspects of Shelf Circulation off Duck, North Carolina

Brandy T. Kuebel Cervantes, J. S. Allen, and R. M. Samelson

Journal of Physical Oceanography

45 Beacon Street, Boston, MA 02108-3693

Vol. 33, No. 10, October 2003

2.1 Abstract

The effects of wind-forced upwelling and downwelling on the continental shelf off Duck, North Carolina are studied through experiments with a two-dimensional numerical primitive equation model. Moored and shipboard measurements obtained during August–November 1994 as part of the Coastal Ocean Processes (CoOP) Inner Shelf Study (ISS) are used for model/data comparisons. The model is initialized with realistic stratification and forced with observed wind and heat flux data. Both strongly stratified and weakly stratified conditions, found during August and October, respectively, are studied. August is characterized by fluctuating alongshelf wind direction, while October is dominated by downwelling-favorable winds. The across-shelf momentum balance is primarily geostrophic on the continental shelf. The alongshelf momentum balance is mainly between the Coriolis force and vertical diffusion with additional contributions from the local acceleration and nonlinear advection terms. The model solutions are utilized to acquire detailed information on the time- and space-dependent variability of the across-shelf circulation and transport and to investigate the dependence of this circulation on the seasonal change in stratification. When the stratification breaks down, as in October, the across-shelf transport is reduced significantly compared to the theoretical Ekman transport for large wind stress values. The paths of individual model water parcels are traced using two methods: calculation of Lagrangian trajectories and time evolution of three Lagrangian label fields. The August period produces complex Lagrangian dynamics due to the switching between upwelling and downwelling winds. The October period illustrates a mean downwelling response which advects parcels across and along the shelf and vertically.

2.2 Introduction

The phenomena of wind-driven coastal upwelling and downwelling are of significant interest due to their widespread impacts on the physics and biology of many continental shelves throughout the world. Large observational efforts, such as the Coastal Ocean Dynamics Experiment (CODE) off San Francisco during 1981–82 and the Coastal Ocean Processes (CoOP) Inner Shelf Study (ISS) off Duck, NC in 1994, have been conducted with major goals of understanding wind-driven flows. The CoOP ISS had a primary inter-disciplinary purpose of quantifying the across-shelf transport of sediments and the planktonic larvae of inner shelf benthic invertebrates (Austin 1998). The central element of the field program was an across-shelf array of sensors to collect time series of biological, sedimentological, and physical variables for the period of August–November 1994 (Butman 1994). Dynamical analysis of the CoOP data can be found in Lentz et al. (1999), Lentz (2001), Austin and Lentz (1999), Austin (1999), and Rennie et al. (1999). In addition, modeling studies using the two-dimensional approximation (variations across-shelf and with depth; uniformity alongshelf) have been conducted with idealized upwelling and downwelling wind forcing (Austin and Lentz 2002).

The purpose of the present study is to understand basic characteristics of the shelf response to observed variable winds during the CoOP ISS for both stratified (August) and unstratified (October) conditions. We use the Blumberg-Mellor (1987) primitive equation model formulated for the two-dimensional situation. We force the model with measured hourly wind and heat flux data and make direct comparisons of model results with the CoOP observations. Estimates of across-shelf transport are computed and examined in detail during the stratified and unstratified

periods. Across-shelf transport is a primary element of wind-driven upwelling and downwelling, though it is not well understood (Dever 1997; Lentz 2001).

An additional goal is to examine the model solutions from a Lagrangian point of view. Existing particle tracking techniques are applied to the model shelf flow field to obtain insight into wind-forced fluid parcel transport. We also introduce a technique of advecting Lagrangian label fields by the model velocities for comparison with the modeled water parcel tracks. Lagrangian mean velocity fields (or mean velocity patchiness plots) provide information about the three-dimensional Lagrangian circulation.

The outline of the paper is as follows. The CoOP field study is described in Section 2.3. The numerical model setup and the particle tracking techniques are described in Section 2.4. Results from the model runs and the Eulerian analyses are discussed in Section 2.5. The Lagrangian results are presented in Section 2.6. A summary is given in Section 2.7.

2.3 Background

Observational data were collected near the U.S. Army Corps of Engineers Field Research Facility (FRF) at Duck, North Carolina (36.18 N) from August through November 1994 (Butman 1994). The location is midway between Cape Henry (36.92 N) and Cape Hatteras (35.27 N). Two rigid towers in 4 m and 8 m depth and three surface/subsurface mooring pairs in 13, 21, and 26 m depth were deployed along a 16 km across-shelf transect (Lentz et al. 1999), as shown in Figure 1. In addition, the 21 m site included a vector-averaging wind recorder meteorological package that measured air and near-surface water temperature, shortwave and longwave

radiation, wind velocity (3.5 m above the sea surface), barometric pressure, and relative humidity (Austin 1999). Wind velocity was also measured 19.5 m above the sea surface on the FRF pier. Additional hydrographic data were obtained through intensive shipboard surveys conducted along the same central mooring line during the months of August and October to provide better spatial resolution relative to the moored data (Waldorf et al. 1995; Waldorf et al. 1996).

All vector time series were rotated to a coordinate system based on the coastline orientation with the alongshelf coordinate y positive toward 340 N and the across-shelf coordinate x positive offshore. A detailed description of the data processing can be found in Lentz et al. (1999) and Alessi et al. (1996).

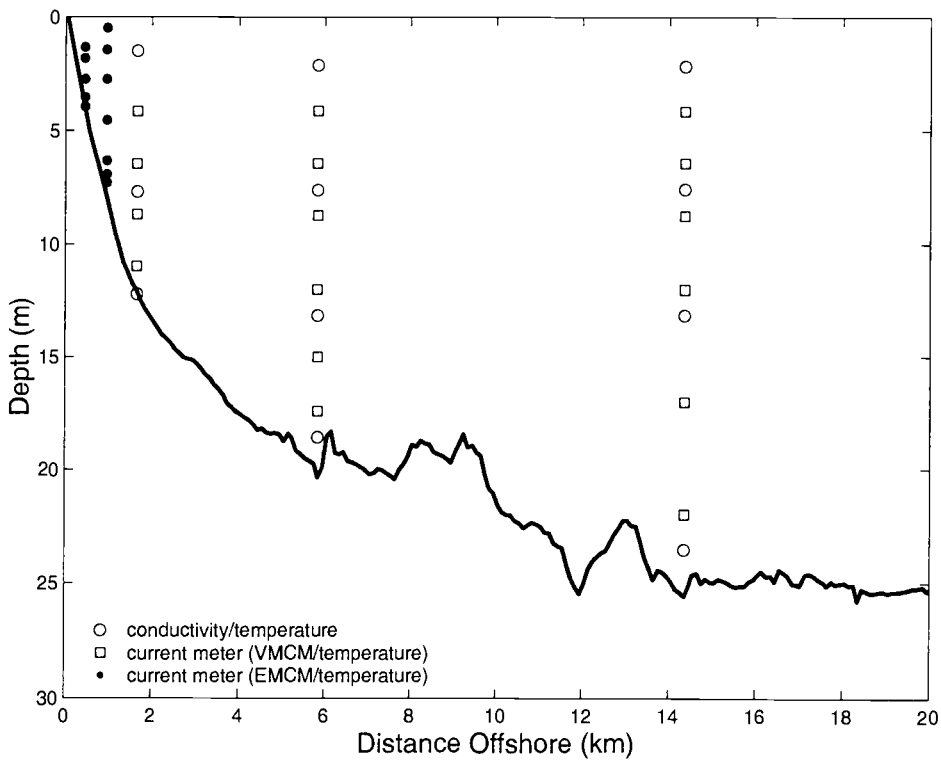

Figure 1. Across-shelf instrument transect during the CoOP field experiment Aug–Nov 1994. Figure is modified from *Figure 2* in Lentz et al. (1999).

Time series of winds, currents, surface heat flux, temperature, and salinity are shown in Figure 2 for the period August 7–November 15, 1994. To focus on subtidal dynamics that are of interest in this study, the time series have been low-pass filtered using a 38-hour half-power point filter (PL64 filter described in Rosenfeld (1983)). The winds vary on a time scale of 3–7 days between upwelling-favorable (northward) and downwelling-favorable (southward) during August and September, but in October and November are dominated by downwelling events. The heat flux time series (with a gap from September 4–October 7) illustrates more surface heating during the summer month of August than in October. The heat flux is significantly correlated with the alongshelf wind stress due to the passage of atmospheric cold fronts, which cause the fluctuating alongshelf wind direction in August and September (Austin and Lentz 1999). The depth-averaged currents from the 26 m site are southward and onshore in the mean. Also plotted in Figure 2 are temperature and salinity at three depths from the 26 m site. The evolution in vertical structure is evident in these time series. Strong vertical gradients in both temperature and salinity are observed throughout August until September 4, at which time a southward storm mixes the water column. After this event, the temperature and salinity show events of warm, fresh surface waters entering the region in September following southward winds.

2.4 Methods

2.4.1. Model Description

The numerical model is a two-dimensional version of the Princeton Ocean Model from Blumberg and Mellor (1987). The model equations are the hydrostatic

primitive equations in sigma coordinates. The Mellor-Yamada (1982) turbulence closure scheme, as modified in Galperin et al. (1988), is embedded. The model domain is an across-shelf (x,z) section bounded by vertical walls at the coast and offshore boundary. There are no variations in the alongshelf (y) direction. The boundary conditions on the velocity components at the coastal and offshore boundaries are no flow in the across-shelf direction (u=0) and free-slip in the alongshelf direction ($v_x = 0$).

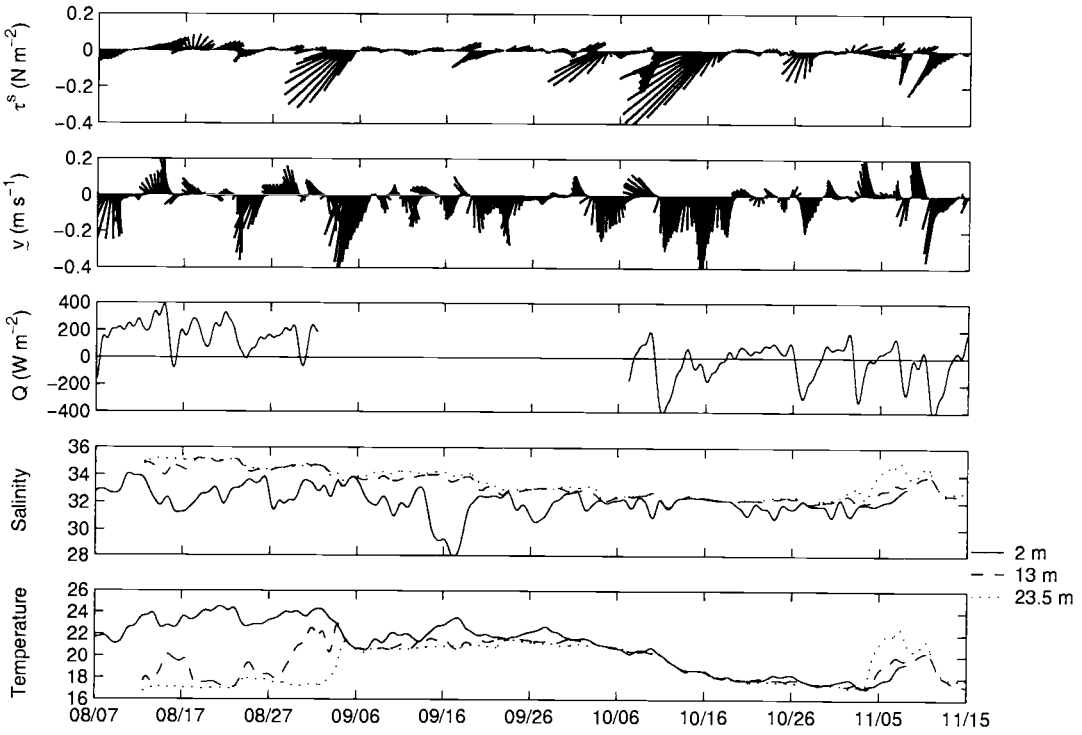

Figure 2. Time series of wind stress vectors calculated from measurements on the FRF pier; depth-averaged current vectors from mooring measurements in 26 m depth; total surface heat flux; salinity and temperature at three depths from mooring measurements in 26 m depth. The vectors are plotted in the x,y coordinate system described in the text where positive y is aligned along 340 N and is generally northwestward. All time series have been low-pass filtered using a 38-hour half power point filter.

2.4.2. Model Setup

The initial state of the model experiments is a coastal ocean at rest with horizontally uniform temperature and salinity fields. The model is forced by spatially independent wind stress components τ^{sx} and τ^{sy} computed from the winds measured at the FRF pier (using a wind-speed dependent drag coefficient as in Large and Pond (1981)) and shortwave radiative heat flux Q_{sw} and the sum of the longwave and turbulent fluxes (Q_{lw}+Q_{sen}+Q_{lat}) computed at the 21-m surface mooring (Austin and Lentz 1999). The wind and heat flux forcing is by the observed hourly values, which are interpolated to the model time step.

The model bathymetry is characteristic of that off Duck, NC (Figure 1) with a relatively steep slope from the coast to about 20 m depth and a gradual slope offshore of the 20 m isobath. The rather complex bathymetric features offshore of 20 m evident in Figure 1 are smoothed for the numerical experiments. Separate experiments are performed for August–September and for October. The initial temperature and salinity fields are discussed in Section 2.4.4 (Figure 3).

The model domain extends from the coastal boundary to a distance of 200 km offshore, with the water depth a constant value of 35 m offshore of 40 km. A uniform grid spacing is used in x with a resolution of 250 m and in σ with 30 σ levels. The horizontal kinematic eddy viscosity and diffusivity are chosen to be small constant values, $A_M = A_H = 2$ m^2 s^{-1}. The background vertical viscosity ν_M and diffusivity ν_H are set to 2.0×10^{-5} m^{2}s^{-1}. The external time step is 5 s and the internal time step is 75 s.

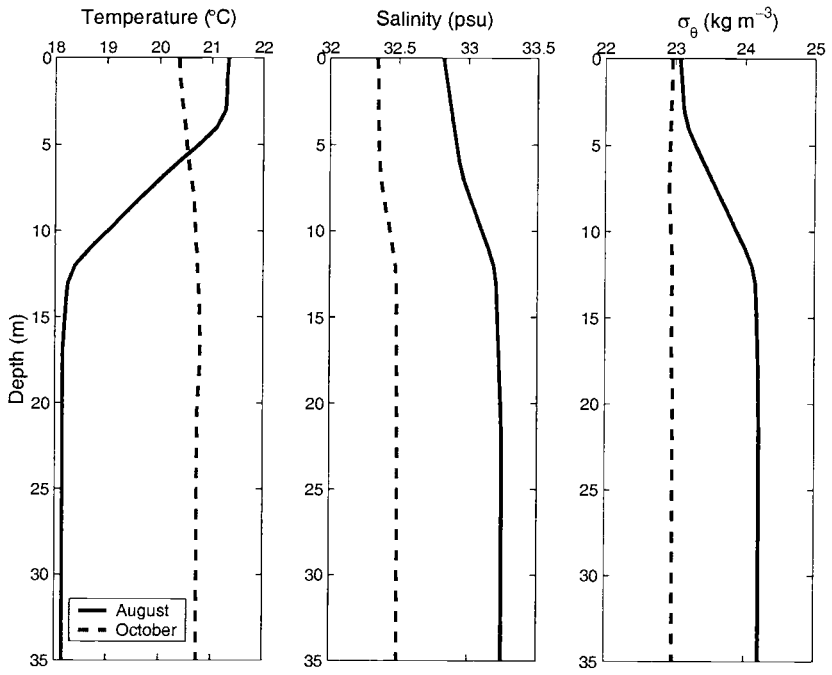

Figure 3. Initial temperature, salinity and σ_θ profiles with depth for the Aug and Oct model simulations. The initial temperature and salinity profiles are computed as the horizontal averages of the mooring measurements on 7 Aug 1994 and 6 Oct 1994.

2.4.3. Lagrangian Calculations

Coastal ocean models are typically formulated and analyzed in terms of Eulerian variables with little consideration given to a Lagrangian interpretation. Here, we pursue also a Lagrangian description. For that purpose, we utilize the Lagrangian information that is directly available from the model and consider the motion of model fluid parcels that are advected by the model-resolved velocity field. Since the model also includes a parameterization of small-scale turbulence, these Lagrangian parcel trajectories comprise only the resolved part of the full fluid motion represented in the model. The interaction between advection and diffusion is a rich aspect of classical fluid mechanics (e.g., Taylor 1953, 1954) and we believe that analysis of

explicit Lagrangian motion in models will be important to improved understanding of such interactions in the coastal ocean.

Lagrangian fluid motion is calculated using two different techniques. The first approach involves computing parcel trajectories by solving the differential equations

$$\frac{dx}{dt} = u, \qquad \frac{dy}{dt} = v, \qquad \frac{d\sigma}{dt} = \frac{\omega}{(H+\eta)}, \tag{1}$$

as done, for example, by Chen and Beardsley (1998). A set of parcels are indexed by their initial positions on a grid of 30 σ levels and 160 x positions (approximately 1 m resolution in z and 1.25 km resolution in x). Numerical solutions to Eq. 1 are calculated utilizing a fourth-order Runge-Kutta scheme. The time step used for the Runge-Kutta scheme is the model internal time step. The updated positions obtained from the equations are saved hourly for each initial parcel position. Interpolation of all three components of velocity to the parcel positions after each iteration is bilinear.

In addition to tracking individual water parcels, we utilize a second technique that gives Lagrangian trajectories for a continuous field of parcels. For calculations without errors, i.e., those performed in the limit of vanishing spatial grid sizes and time steps, the Lagrangian parcel trajectories obtained from both techniques would be equivalent. This second approach involves the definition of three Lagrangian label fields that are advected by the model velocities. The Lagrangian labels, $X(x,z,t)$, $Y(x,y,z,t)$, and $Z(x,z,t)$, satisfy the following equations:

$$\frac{DX}{Dt} = 0, \qquad \frac{DY}{Dt} = 0, \qquad \frac{DZ}{Dt} = 0, \tag{2}$$

where $\frac{D}{Dt} = \frac{\partial}{\partial t} + u\frac{\partial}{\partial x} + v\frac{\partial}{\partial y} + w\frac{\partial}{\partial z}$. The initial conditions are

$$X(x,z,t=0) = x, \quad Y(x,y,z,t=0) = y, \quad Z(x,z,t=0) = z. \tag{3}$$

With the two-dimensional approximation for the Eulerian flow we obtain

$$\frac{D}{Dt}\frac{\partial Y}{\partial y} = 0, \tag{4}$$

so we can write

$$Y(x, y, z, t) = y + Y'(x, z, t), \tag{5}$$

and we can determine Y by solving for Y', where

$$\frac{DY'}{Dt} + v = 0, \tag{6}$$

with

$$Y'(x, z, t = 0) = 0. \tag{7}$$

As will be shown in Section 2.6.1, examination of the time evolution of the label fields helps to provide insight into the Lagrangian characteristics of the flow. The labels X, Y and Z are calculated as fields on the model grid with the higher-order accurate advection scheme of Smolarkiewicz (1983) using three iterations of the corrective step. Displacements are obtained by differencing the initial and final values at a given grid point in x-z space. We note that the evolution of the Lagrangian label fields is completely determined by advection with the model-resolved velocity fields. Consequently, the behavior of the labels will differ from that of passive tracer fields that are diffused by the effects of small scale turbulence. This difference is shown explicitly by analysis of results from comparable experiments in Section 2.6.1.

Table 1. Summary of depth-averaged model/data correlation coefficients for alongshelf velocity and temperature. The first experiment was initialized with the monthly mean of the mooring data from Aug and Oct. The second experiment was initialized with the daily mean of the mooring data from Aug 7 and Oct 6. The third experiment was initialized with the shipboard data from Aug 11 and Oct 10.

Initial T,S Source		13-m mooring		21-m mooring		26-m mooring	
		V	T	V	T	V	T
Monthly mean	Aug	0.54	0.43	0.52	0.35	0.33	0.33
mooring data	Oct	0.71	0.89	0.71	0.96	0.69	0.92
7 Aug and 6 Oct	Aug	0.63	0.53	0.67	0.52	0.52	0.48
mooring data	Oct	0.71	0.85	0.66	0.93	0.68	0.91
11 Aug and 10 Oct	Aug	0.57	0.31	0.56	0.23	0.36	0.20
shipboard data	Oct	0.69	0.90	0.69	0.96	0.63	0.92

2.4.4. Model Sensitivity

To determine the sensitivity of the model to initial conditions, we initialize with three different temperature and salinity fields and compare the model results to alongshelf velocity and temperature data for the months of August and October. The three initialization fields consist of the monthly means of temperature and salinity from the mooring data, mooring data from August 7 and October 6 (the first day of the model experiments), and shipboard data from August 11 and October 10 (the first shipboard observations). A summary of the model sensitivity analysis and the resulting depth-averaged model-data correlation coefficients is shown in Table 1. It is apparent from this summary that the correlation coefficients are improved for

the month of August with the August 7 observed initial temperature and salinity. The remaining sections of the paper will therefore discuss the results using the initial fields from August 7. For the month of October, the differences in Table 1 are small. For consistency we use the October 6 observed initial temperature and salinity for the October run (Figure 3).

2.5 Eulerian Analysis

2.5.1. Model-Data Comparisons

We perform several model-data comparisons utilizing the data from the CoOP experiment. Hourly depth-averaged alongshelf currents from the model and the observations at the five mooring locations are shown in Figure 4 for August–September and October. Agreement is generally good in August, with the lowest correlation at the 26 m mooring. The model appears to underestimate the effect on the alongshelf current of downwelling-favorable winds ($\tau_y < 0$). Presumably, this is caused by the neglect of an alongshelf pressure gradient force in the model, which was shown to be important in forcing southward currents during downwelling-favorable winds by Lentz et al. (1999). The alongshelf pressure gradient is associated with the Chesapeake Bay plume waters that flow southward during the study period and reach Duck, NC about 1–1.5 days after the relaxations of upwelling winds (Rennie et al. 1999). Generally good agreement of alongshelf currents is also found in October. The observations have greater standard deviation values than the model for August and October at all locations (Table 2). The magnitudes of the October means from the observations are larger than those from the model, and both model and observations are southward in the mean at all mooring locations.

The August model means are northward at all sites, while the observations are southward, although the magnitudes are small compared to those in October. The root mean square error values are maximum at the 13 m mooring for both months and minimum at the 4 m mooring in August and the 8 m mooring in October. The modeled and observed alongshelf currents also agree well at all depths at each site. The modeled and observed across-shelf velocities have fair agreement in August, but poor agreement in October (Table 3).

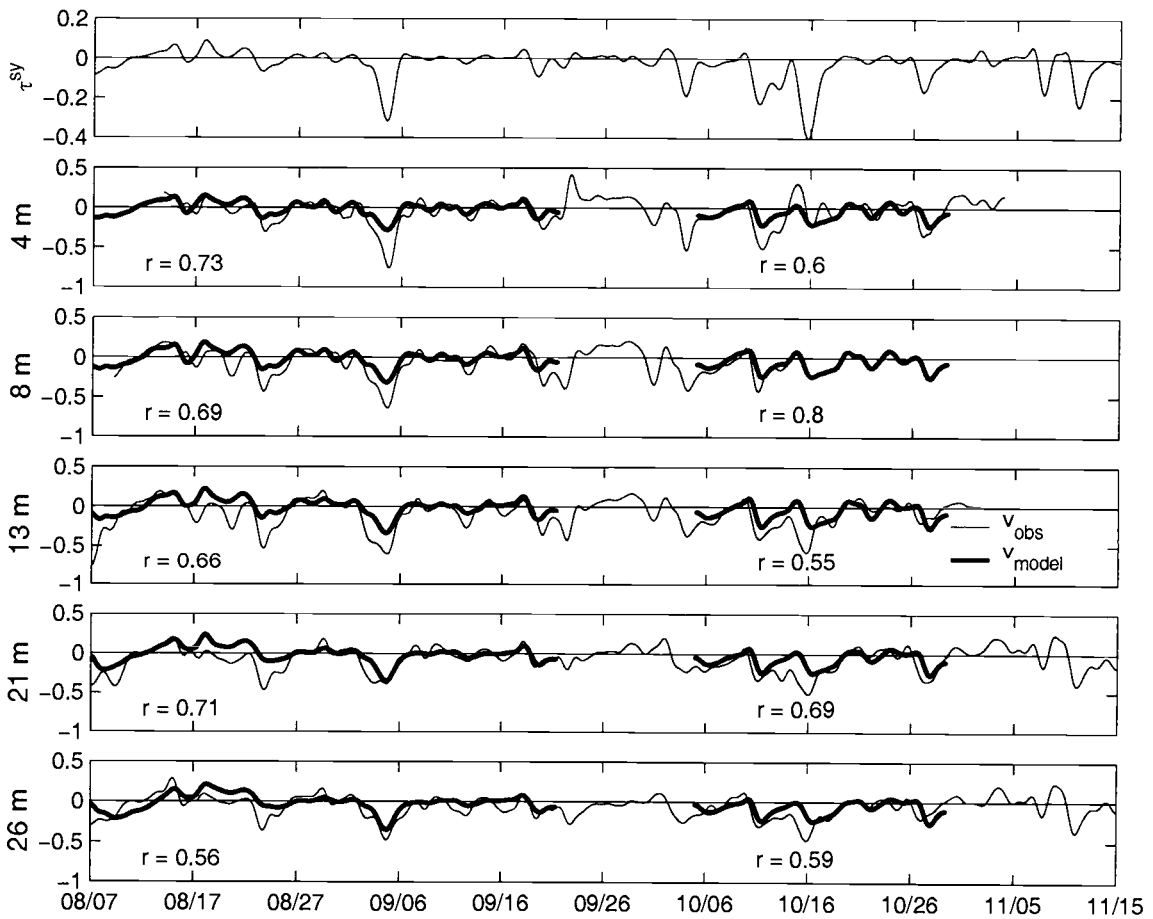

Figure 4. Model (thick line) - data (thin line) comparison of depth-averaged alongshelf current (m s^{-1}) for August and October at the five mooring locations. The alongshelf wind stress component (N m^{-2}) measured at the FRF pier is also plotted in the top panel. The correlation coefficients r are also given.

Table 2. Summary of model/data means, standard deviations, correlation coefficients, r, and root mean square errors, rmse (m s^{-1}), of the depth-averaged alongshelf velocity. The root mean square error is computed over n hours as $rmse = [\frac{1}{n}\sum_{i=1}^{n}(v_m - v_o)^2]^{1/2}$ where v_o denotes observations and v_m denotes model. The values are given for each mooring position for the months of Aug and Oct.

Mooring		Mean (m s^{-1})		Stdv (m s^{-1})		r	RMSE (m s^{-1})
		Model	Data	Model	Data		
4 m	Aug	0.026	-0.009	0.075	0.110	0.73	0.082
	Oct	-0.055	-0.066	0.082	0.164	0.60	0.132
8 m	Aug	0.026	-0.021	0.088	0.142	0.69	0.113
	Oct	-0.063	-0.129	0.089	0.118	0.80	0.097
13 m	Aug	0.022	-0.066	0.099	0.199	0.66	0.176
	Oct	-0.061	-0.121	0.101	0.159	0.55	0.147
21 m	Aug	0.019	-0.075	0.106	0.167	0.71	0.152
	Oct	-0.067	-0.142	0.092	0.158	0.69	0.138
26 m	Aug	0.004	-0.026	0.111	0.133	0.56	0.119
	Oct	-0.074	-0.105	0.086	0.131	0.59	0.111

Table 3. Summary of depth-averaged model/data means, standard deviations, correlation coefficients, r, and root mean square errors, rmse (m s^{-1}), of the across-shelf velocity. The values are averaged over the depths of the instrument locations at each mooring position for the months of Aug and Oct.

Mooring		Mean (m s^{-1})		Stdv (m s^{-1})		r	RMSE
		Model	Data	Model	Data		
4 m	Aug	-0.013	0.004	0.015	0.043	0.76	0.039
	Oct	0.008	0.065	0.014	0.092	0.24	0.107
8 m	Aug	-0.011	0.004	0.025	0.035	0.45	0.039
	Oct	0.002	0.003	0.022	0.025	0.23	0.044
13 m	Aug	-0.008	-0.002	0.027	0.025	0.37	0.033
	Oct	0.010	-0.011	0.018	0.018	0.02	0.035
21 m	Aug	-0.004	-0.001	0.028	0.036	0.45	0.037
	Oct	0.005	-0.009	0.019	0.034	-0.10	0.045
26 m	Aug	-0.002	-0.023	0.025	0.040	0.36	0.043
	Oct	0.000	-0.018	0.016	0.039	0.06	0.047

Shipboard across-shelf transects collected by Waldorf et al. (1995, 1996) are also compared to the model temperature field. These across-shelf sections occurred on seven days in August and eleven days in October and extended from 1 km to between 20 and 50 km offshore. The mean and standard deviation of temperature from these dates are computed from the model, the shipboard observations, and the mooring data. These results are plotted as contours in offshore distance and depth in Figure 5. Mean model temperature agrees well in August, capturing the observed

thermocline depth and upward tilt of isotherms near the coast. Variability in the depth of the thermocline throughout the month, as shown by the high standard deviation values between 10–15 m depth, is apparent in both the model and the data. However, the data show that this variability extends to the coastal boundary, and the model only displays high variability offshore of 20 km. In October, the model is warmer than the observations by about 2 degrees and shows less variability about the mean temperature field than is observed. The model and shipboard observations diverge on October 12, at which time a strong downwelling event and associated cooling is observed in the study region (Figure 2). The model temperature field does decrease during this period, but not as significantly as the observed temperature. Austin (1999) found that the drop in area-averaged water temperature observed in October was due to both surface heat loss and the alongshore transport of heat. The alongshore heat flux was significant during the period of October 10–13 and during 3 additional 1–3 day periods throughout October, though usually slightly less than the surface heat flux. The model contains a time-varying surface heat flux component, but no alongshore heat flux. The neglect of this process is likely the cause of the model's underprediction of the temperature decrease in October. Salinity comparisons (not shown) reveal variability in the observations at all mooring locations that is not captured by the model. The likely reason for this disagreement is again the neglect of three-dimensional effects, which leads to the exclusion of fresh Chesapeake Bay plume water observed in this region.

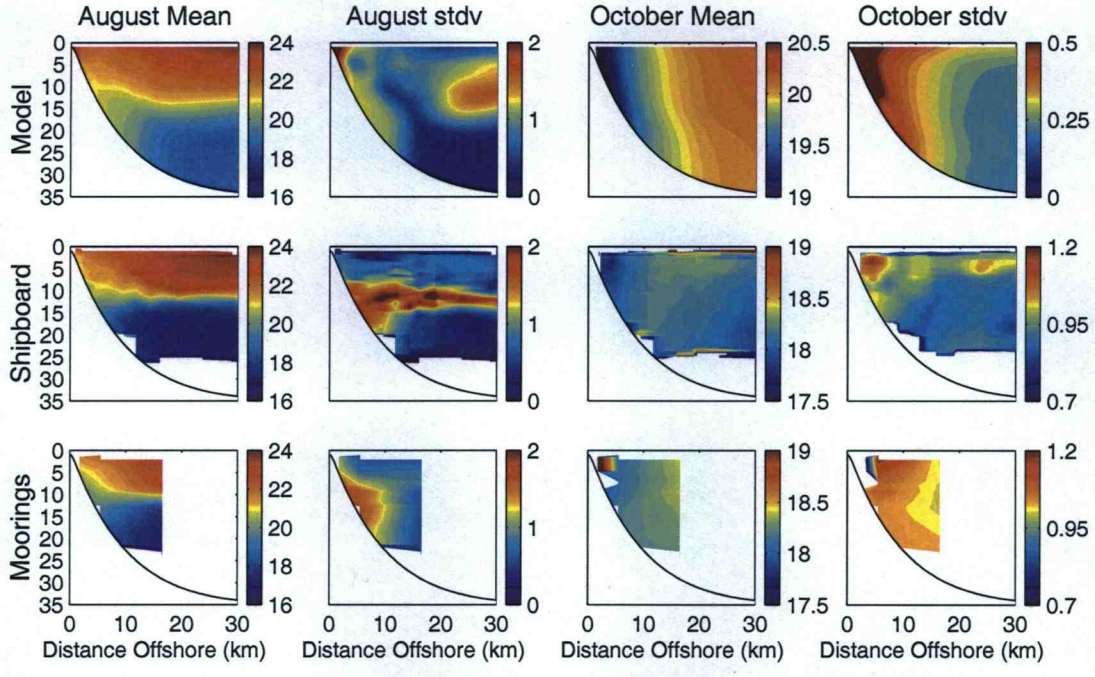

Figure 5. Mean and standard deviation of temperature from the model (top), shipboard observations (middle), and mooring data (bottom) for the months of August and October. The horizontal axis is distance offshore (km) and the vertical axis is depth (m). Note the different scales for the model and the observations in Oct.

2.5.2. Dynamical Analysis

Having demonstrated the model's ability to represent fields of interest, we now analyze the resulting flow behavior and the dynamics from each monthly simulation. An overview of the general flow behavior is shown by contour plots of the monthly mean and standard deviation of potential density σ_θ, streamfunction ψ, alongshelf velocity v, and across-shelf velocity u in Figure 6 for August 7–August 30 and October 6–October 29. It is clear that August is strongly stratified with a mean upwelling circulation, while October is weakly stratified with a mean downwelling circulation. August also has a mean northward coastal jet with velocities greater than 0.05 m s^{-1} and a region of southward velocities of 0.03 m s^{-1} just offshore of and below the coastal jet. This structure is due to upwelling winds modified by

the intermittent presence of downwelling-favorable winds throughout the month. October has southward velocities everywhere on the shelf, with the strongest values offshore of 20 km and from the surface to about 15 m depth. Mean offshore flow in August is concentrated in a 10 m surface Ekman layer. The mean onshore return flow is in a thin bottom boundary layer extending to 30 km and evenly distributed throughout the water column offshore of 30 km. In October, mean onshore surface flow and offshore bottom flow are in layers about 15 m thick, separated by a thin ($\leq$ 5 m) middle layer with little across-shelf motion.

Much of the variability in σ_θ lies within 10 km of the coast and in v within 20 km of the coast where the isopycnal advection and the alongshelf jet reverse direction in response to the changing winds. In August, a region of strong variability in σ_θ also occurs between 10-15 m depth offshore of 20 km due to the changing pycnocline depth. The width of variability in the density and alongshelf velocity fields depends on the forcing and initial stratification. In additional numerical experiments in which we vary the magnitude of the alongshelf wind stress from $0.125\tau^{sy}$ to $4\tau^{sy}$, we find the offshore scale of the jet varies with the smallest scale of 8 km for $0.125\tau^{sy}$ and the largest scale of 40 km for $4\tau^{sy}$. The scale of the fluctuations in the density field vary in a similar manner. For reference, we calculate the Rossby radius of deformation R_D for the first baroclinic mode as a function of offshore distance by solving the vertical eigenvalue problem using the local water depth and initial stratification and assuming a flat bottom. The value of R_D increases rapidly from less than 1 km near the coast ($x \leq 3$ km) to 7.5 km for $x \geq 40$ km and is independent of $|\tau^{sy}|$. Consequently, we conclude that the offshore scale of the fluctuations in the coastal jet is related to the magnitude of τ^{sy} and is not characterized by R_D alone.

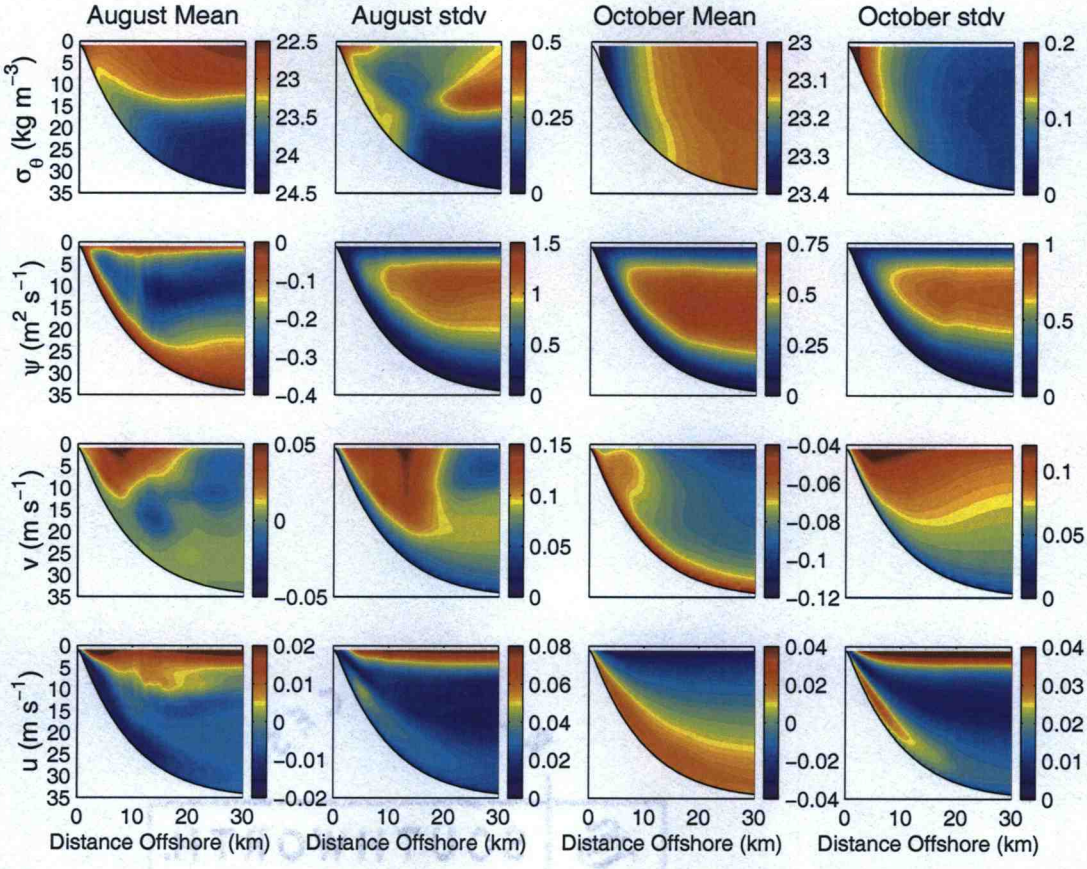

Figure 6. Mean model fields and standard deviations for the months of August and October. The fields contoured are σ_θ (row 1), streamfunction ψ (row 2), alongshelf velocity v (row 3), and across-shelf velocity u (row 4). All fields have been averaged over an inertial period.

The mean alongshelf momentum balance terms in August and October are plotted in Figure 7. For convenience in the following discussion, we write the terms in Cartesian coordinates (x, z) with velocity components (u, w). The alongshelf balance is dominated in both months by the Coriolis force fu and vertical diffusion $(K_M v_z)_z$, but in August, contributions from the nonlinear advection terms, $(uv)_x + (wv)_z$, are significant from the coast to about 10 km offshore (20 m depth), and the local acceleration term v_t plays a role in the balance offshore of 10 km. In a 2-D modeling study of upwelling on a stratified shelf with idealized wind forcing,

Austin (1998) found a balance between the Coriolis force and vertical diffusion with a contribution from the local acceleration term in the upper 10 m offshore of the upwelling front. The Austin (1998) dynamical balances are similar to those found in the present study with forcing by observed winds during August, with the exception of the importance here of the nonlinear terms. The mean across-shelf balance (not shown) is dominated by geostrophy in both months with contributions from vertical diffusion, nonlinear advection, and acceleration in August.

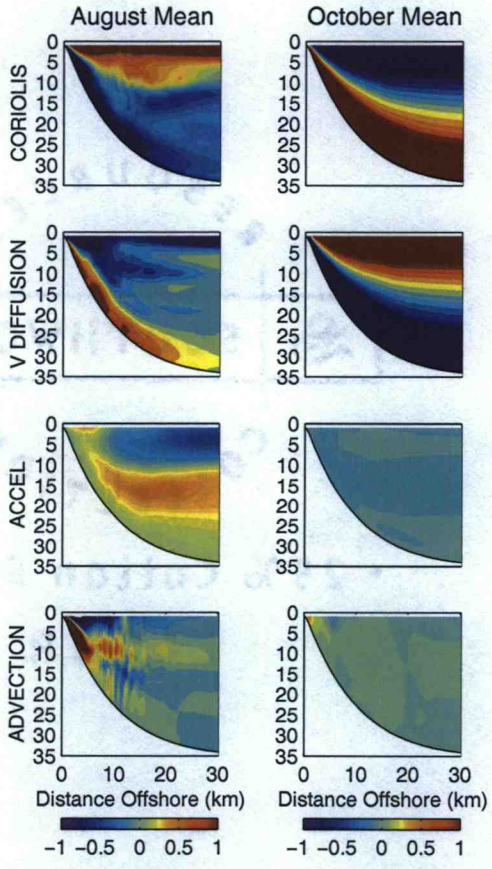

Figure 7. Mean model alongshelf momentum balance terms for the months of Aug (left) and Oct (right). The horizontal diffusion term is relatively small and is not plotted. The units for each term are 10^{-6} m s^{-2}. The signs of the terms correspond to all terms on the left-hand side of the equation. All terms have been averaged over an inertial period.

The nonlinear advection terms contribute to the depth-dependent alongshelf momentum balance during upwelling-favorable winds when the wind stress is greater than about 0.05 N m^{-2}. They make a much smaller contribution during downwelling with winds of comparable magnitude. The reasons for the different magnitudes of the nonlinear advection terms during upwelling and downwelling may be seen from plots of these terms together with the v field and streamfunction ψ during upwelling and downwelling events with similar τ^{sy} magnitude on August 18 and October 17, respectively (Figure 8). The nonlinear advection terms may be written as $\mathbf{u} \cdot \nabla v = uv_x + wv_z$, which corresponds to a spatial derivative of v in a direction tangent to the streamlines ψ=constant. The relative intensity of the across-shelf circulation can be estimated from the spacing of the streamlines. Thus the magnitude of the term $\mathbf{u} \cdot \nabla v$ can be qualitatively assessed from the streamline spacing and the gradient of v along streamlines. During upwelling, a narrow and well-defined northward coastal jet forms near the surface (Figure 8). A region of significant positive across-shelf and vertical gradients in v is found from the surface to about 15 m depth near the coast, an area of relatively concentrated upwelling circulation, resulting in large positive advection values. From 10 km to 25 km offshore, the nonlinear terms are negative in the top 10 m due to the negative across-shelf gradient in v. The structure of the nonlinear terms on August 18 (Figure 8) is typical of upwelling events throughout August and is consistent with the August mean (Figure 7). During downwelling on October 17, the jet-like structure of the alongshelf velocities is less pronounced than during August upwelling. Gradients of v are relatively weak in both x and z and the across-shelf downwelling circulation occurs over a larger region and is generally weaker than the August upwelling

circulation. The resulting nonlinear terms in October (Figure 8) are noticeably different from zero only in a small region near the coast where v_x is largest. This structure again mirrors that in the October mean (Figure 7). Similarly, the nonlinear terms are relatively unimportant during downwelling in August (Aug. 7–9 and Aug. 23–25), although the alongshelf velocity structure is complicated by the intermittent upwelling forcing.

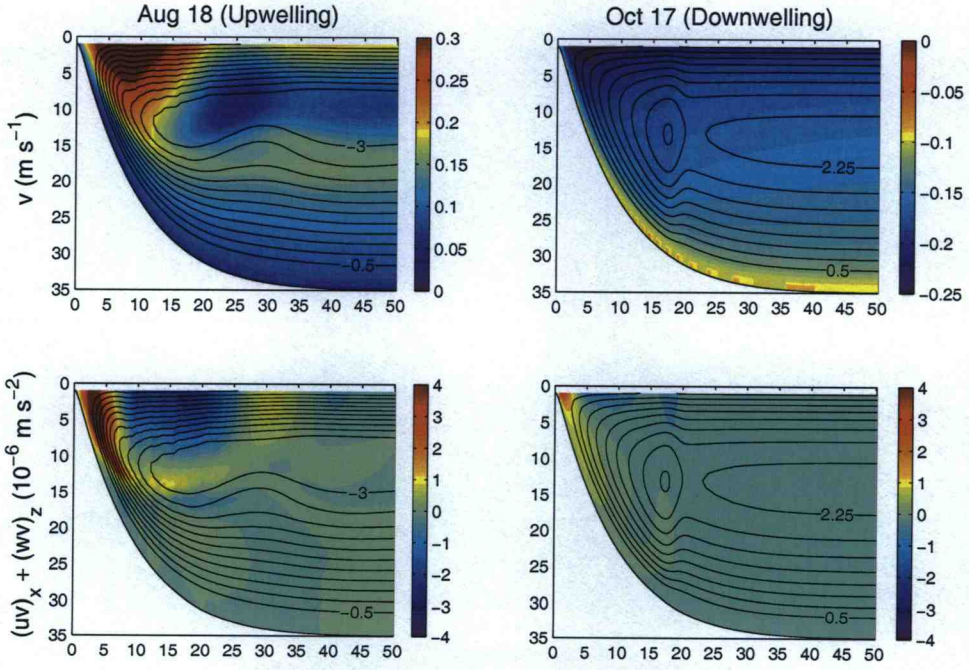

Figure 8. Contours of alongshelf velocity v (top) and the nonlinear advection term (bottom) for 18 Aug (left) and 17 Oct (right). The streamfunction ψ is also plotted as black lines with contour interval 0.25 m^2 s^{-1} for each day. On 18 Aug, the winds are upwelling-favorable, and on 17 Oct, the winds are downwelling-favorable. Notice the different scales for v on the two days.

It is also instructive to examine the time-dependent behavior of terms in the depth-averaged momentum balances. The depth-averaged alongshelf momentum balance is dominated at the 4 and 8 m moorings by the surface and bottom stress

terms with a contribution from nonlinear advection. The slope of the regression line between nonlinear advection and wind stress during upwelling conditions (positive wind stress) is close to 1 at both moorings, but is very small and negative during downwelling conditions (Figure 9). The regression slope between wind stress and bottom stress is almost 1 during downwelling, and smaller during upwelling. These results support the finding of an asymmetry in upwelling and downwelling dynamics described in the previous paragraph. During upwelling, nonlinear advection is of order 1 importance in the depth-averaged alongshelf balance at 4 and 8 m. In contrast, the balance during downwelling is mainly between wind stress and bottom stress. The local acceleration term also enters the balance at the three offshore moorings with increasing importance offshore. The alongshelf pressure gradient force, which is not represented in this model as discussed in Section 2.5.1, was found from analysis of the observations to be significant in the alongshelf momentum balance offshore of 13 m by Lentz et al. (1999). The depth-averaged across-shelf balance (not shown) is dominantly geostrophic at all sites. Note that we neglect the across-shelf gradient of the radiation stress term S_{xx} and the associated contribution of wave-driven setdown caused by non-breaking surface gravity waves or set-up inside the surf zone, which was found to be significant at depths of 13 m or less in the observations of Lentz et al. (1999).

In Figures 10 and 11, we examine the characteristics of a strong downwelling wind event that occurred during September 4–5. Prior to the event on September 2, the isopycnals are upwelled near the surface and downwelled near the bottom as a result of the time-varying alongshelf wind direction. The Coriolis and vertical diffusion terms show a surface Ekman layer with onshore velocities. This surface

layer deepens on September 3 in response to an increase in southward winds. A bottom Ekman layer is also apparent. By September 4, the isopycnals show the development of a sharp downwelling density front that has been advected 10 km offshore. The surface and bottom layers are almost 15 m deep. Strong downwelling circulation offshore of 15 km is apparent in ψ. The density front continues to move offshore, as seen on September 5, leaving a well mixed region with the least dense waters 10–15 km offshore. Vertical velocities in the strong downwelling region of the front are about 2×10^{-4} m s^{-1}. The position of the front is also clear from the Coriolis and vertical diffusion terms which show deep frictional Ekman layers offshore of 30 km with much smaller values onshore of 20 km in the well-mixed region. The acceleration and nonlinear advection terms (not shown) are much smaller than the Coriolis and vertical diffusion terms throughout the event (3×10^{-6} m s^{-2}).

The variations in the temperature field (Figure 11) are similar to those of density (Figure 10). The offshore advection of the temperature front is apparent. The dominant balance in the temperature equation is between vertical diffusion, $-(K_H T_z)_z$, and advection, $(uT)_x + (wT)_z$. In the surface layer throughout September 2–5, advection is positive and slightly larger than diffusion, producing a negative tendency T_t. The vertical advection term is of order 10^{-5} °C s^{-1}, so horizontal advection dominates. In the bottom layer, the signs are opposite, so T_t is positive and larger than in the surface layer. These surface and bottom layers grow throughout the event and move offshore just as the Ekman layers do (Figure 10). This deepening is due to increased vertical mixing and advection as the wind stress increases.

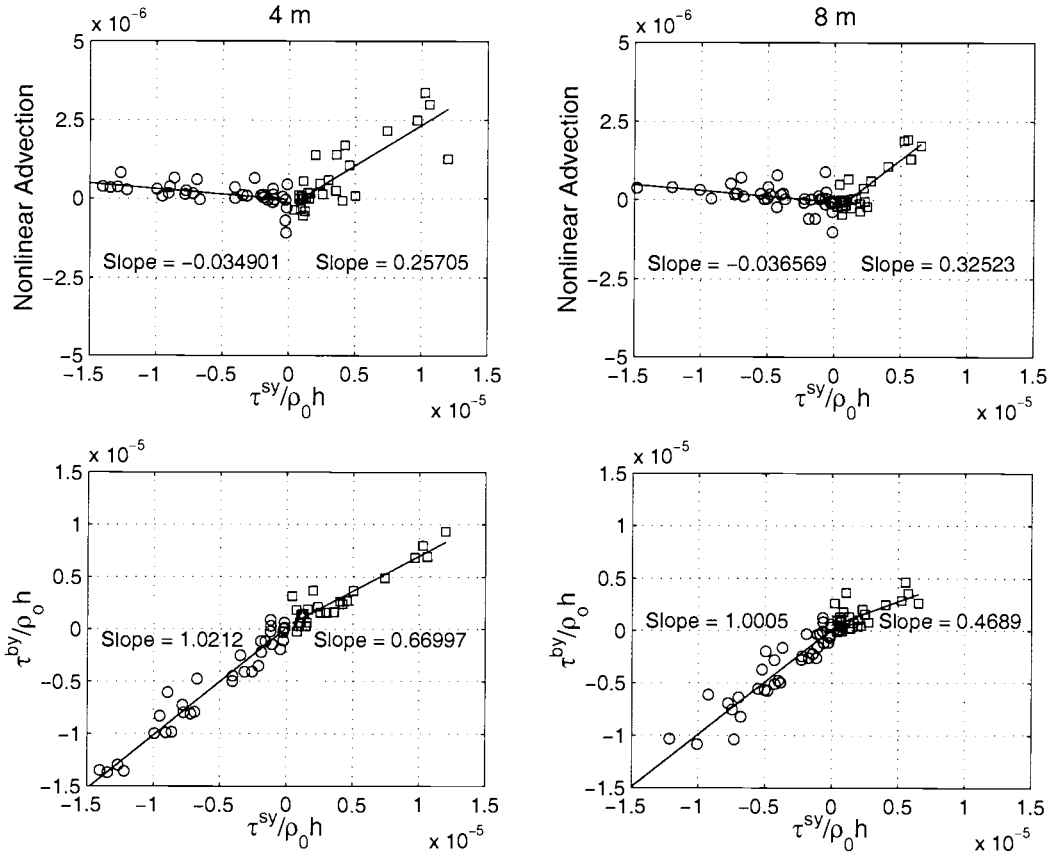

Figure 9. Scatter plots of terms ($m^3\ s^{-2}$) in the depth-averaged alongshelf momentum balance at 4 and 8 m from Aug–Sept and Oct. The upper panels show the nonlinear terms on the y-axis and wind stress on the x-axis. The lower panels show the bottom stress on the y-axis and wind stress on the x-axis. Points plotted as squares represent positive wind stress (upwelling) and circles denote negative wind stress (downwelling).

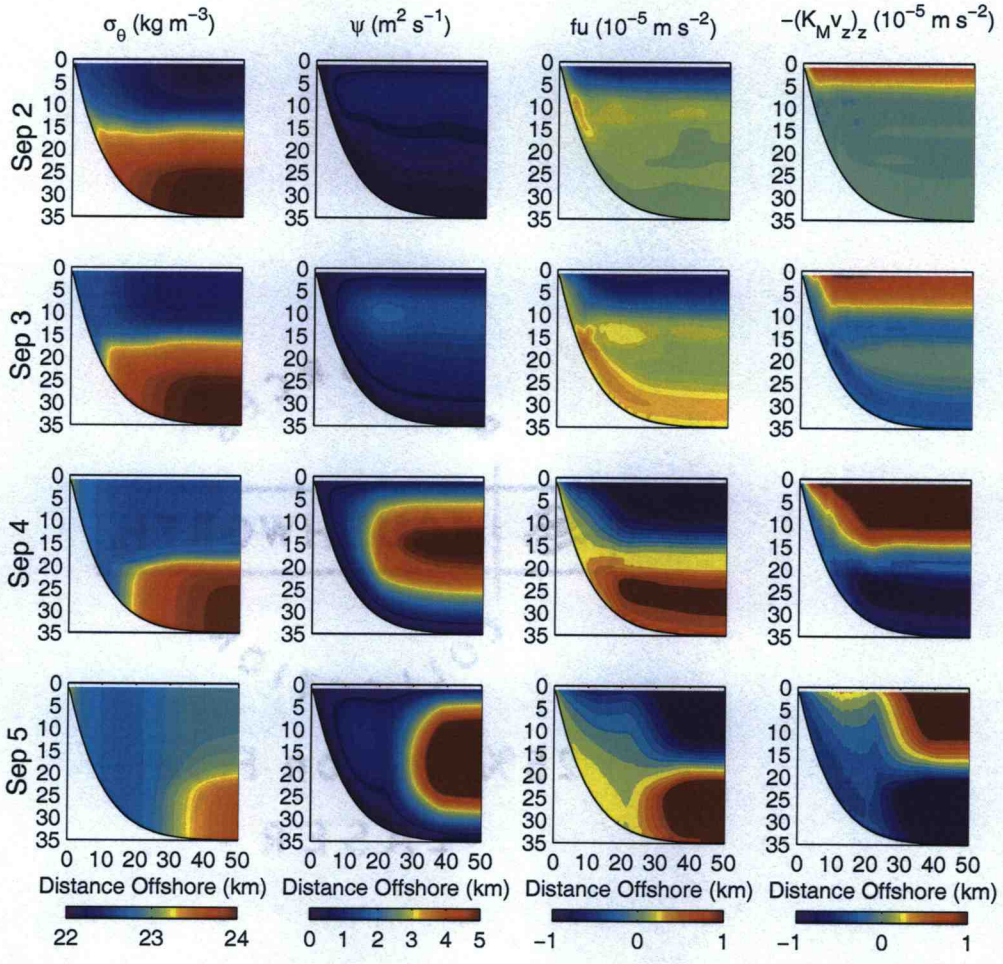

Figure 10. Contours of the σ_θ and ψ fields and the Coriolis and vertical diffusion terms from the alongshelf momentum balance during Sept 2–5. The signs of the terms correspond to all terms on the left-hand side of the alongshelf momentum equation. The fields and terms have been averaged over an inertial period.

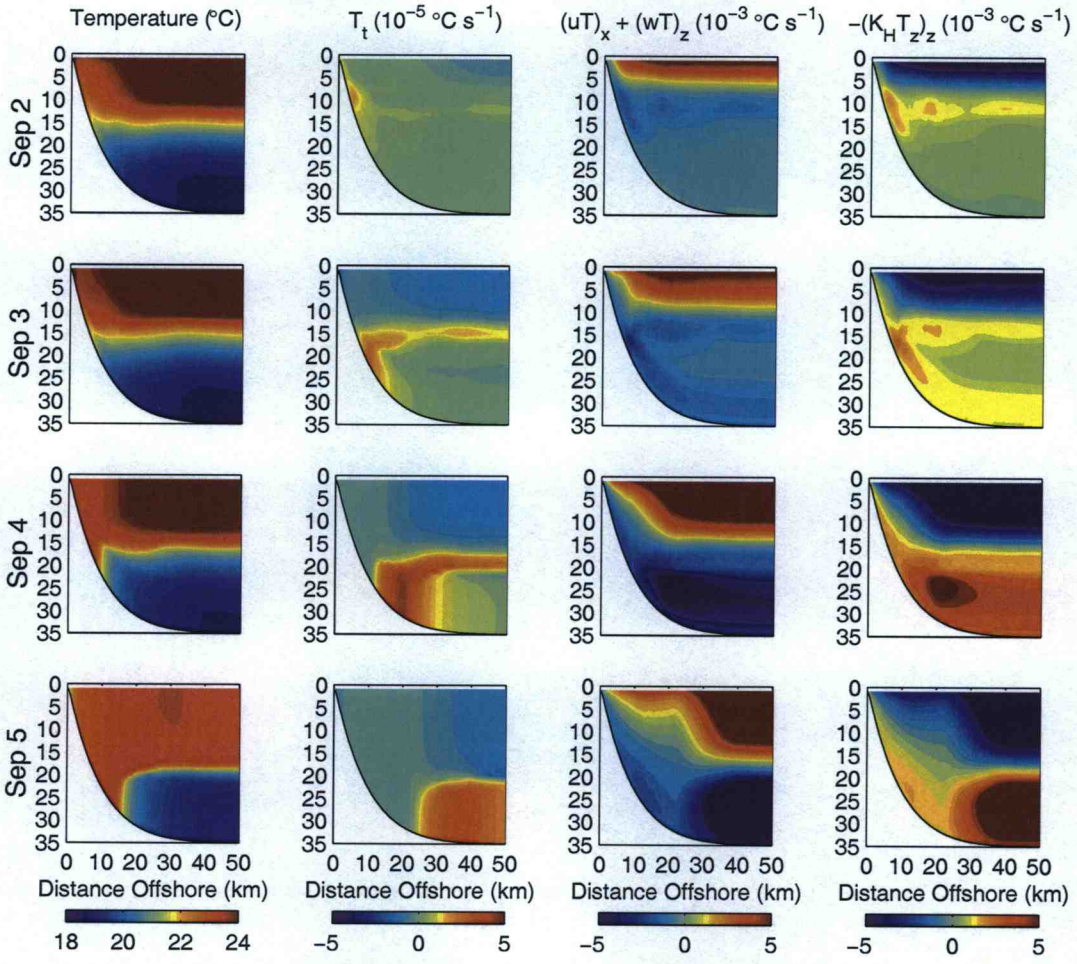

Figure 11. Contours of temperature and the tendency, advection, and vertical diffusion terms from the temperature equation during Sept 2–5. The horizontal diffusion term is quite small (10^{-6}) and is not plotted. The signs of the terms correspond to all terms on the left-hand side of the equation. The terms have been averaged over an inertial period. Note the different scale for the tendency term T_t.

The model simulations do not restratify following this strong downwelling event. The mooring data, which only extend to about 15 km offshore, agree with this result with the exception of warm, fresh surface waters that enter the region following southward winds (See Figure 2). Unfortunately, no shipboard data exist for the September time period.

2.5.3. Across-shelf Transport

One of the goals of this modeling study is to understand the nature of across-shelf transport during wind events. In order to investigate this, we look at the dependence of the across-shelf circulation on stratification. As expected, the low-pass filtered surface velocities at the 21 m and 8 m mooring positions are offshore during upwelling-favorable wind events and onshore during downwelling-favorable wind events (Figure 12). This surface flow is balanced at 8 m by a bottom flow in the opposite direction that is smaller in magnitude but extends over a greater depth. The vertical diffusion of across-shelf momentum extends throughout the water column at 8 m for $|\tau^{sy}|$ greater than about 0.05 Nm^{-2}. During upwelling $(K_M u_z)_z$ is positive and during downwelling it is negative. Before the September 4 storm, the velocity profile at 21 m is more complex than at 8 m. The vertical mixing layers extend only about 8 m from the surface and bottom, and values in the interior are close to zero. Depth-time contours of K_M (not shown) show a very similar spatial pattern to $(K_M u_z)_z$. The bottom panel of Figure 12 shows the breakdown of stratification in σ_θ at 21 m on September 4 and the weakly-stratified water column that is maintained following the storm. At 8 m, the water column becomes unstratified about 10 days earlier than at 21 m. After September 4, the across-shelf velocity structure at the two sites is more similar and mixing extends from the surface to the bottom during relatively weak wind events. This indicates that stratification plays an important role in the qualitative nature of the across-shelf circulation.

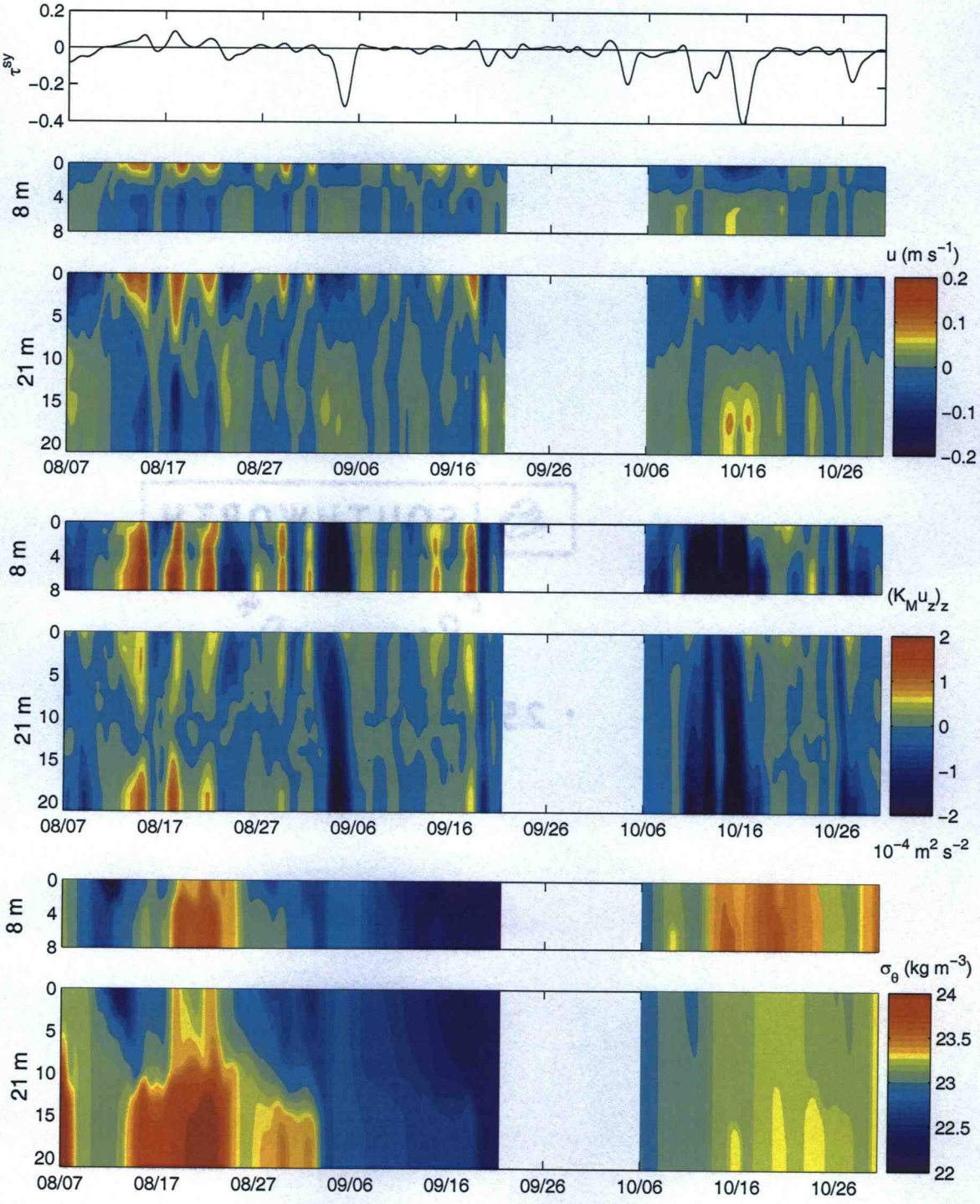

Figure 12. Low-pass filtered time series of across-shelf velocity, vertical diffusion of across-shelf velocity, and σ_θ from the model at the 8- and 21-m mooring locations. The alongshelf wind stress time series is also plotted in the top panel.

It is useful to examine the model output in a manner similar to the analysis of Lentz (2001), who shows that observed surface and bottom transports are reduced relative to theoretical Ekman transports during unstratified periods with $\tau^{sy} \geq 0.1$ N m^{-2}. The following discussion illustrates that the theoretical Ekman transport is a good approximation of the across-shelf transport for stratified conditions but is invalid for unstratified conditions. This is because the assumption that the internal stress is small compared to the surface and bottom stress is incorrect when the water column is unstratified. The theoretical Ekman transports, obtained from the depth-integrated alongshelf momentum balance for steady flows with small nonlinear terms, are

$$U^s = \frac{\tau^{sy}}{\rho_0 f}, \qquad U^b = -\frac{\tau^{by}}{\rho_0 f}. \tag{8}$$

These follow from integrating the alongshelf balance from the surface at $z = 0$ to a depth $z = -\delta^s$ and from the bottom, $z = -h$, to a height $-h + \delta^b$ and assuming the stresses vanish at -δ^s and $-h + \delta^b$. In a two-dimensional shelf flow, if the surface and bottom transports are smaller than the Ekman transports (Eq. 8), then the across-shelf circulation has been reduced (Lentz 2001). This typically occurs if frictional effects are important throughout the water column so that the surface and bottom boundary layers merge. The wind stress τ^{sy} is computed as described in Section 2.4.2. The bottom stress, τ^{by}, is computed in the model using a quadratic drag law,

$$\frac{\tau^{by}}{\rho_0 f} = C_D v_b \sqrt{u_b^2 + v_b^2}, \tag{9}$$

with

$$C_D = \kappa^2 [ln(\Delta z_b / z_0)]^{-2}, \tag{10}$$

where subscribt b on the velocity components designates values at the center of the bottom grid cell, $\kappa = 0.4$ is the von Karman constant, $z_0 = 1$ cm is the bottom roughness parameter, and $\Delta z_b = 1/2(\Delta\sigma_b H)$, with $\Delta\sigma_b$ the bottom σ grid cell size.

We compute the total offshore transport from the model, denoted as T_+ and defined as the depth integral of the quantity U_+ multiplied by the sign of u at the surface, where $U_+ = u$ for $u \geq 0$ and $U_+ = 0$ for $u < 0$ (Figure 13). Positive values indicate offshore transport in the surface layer (upwelling), and negative values indicate offshore transport in the bottom layer (downwelling). The value of T_+ during downwelling events on August 24 and September 4 are shown at the top of Figure 13. The offshore transport is less between 3–7 km during the strong downwelling event on September 4 when the stratification breaks down even though the August 24 event has a smaller wind stress magnitude. T_+ is much less than the Ekman transport $\tau^y/\rho_0 f$ on September 4 out to 15 km offshore, at which point it begins to increase and reaches the Ekman transport value (3 m^2 s^{-1}) at 30 km offshore. This is also reflected in the time series of T_+ and $\tau^y/\rho_0 f$ in Figure 13 (bottom), in which the theoretical Ekman transport (thin lines) is much larger than that from the model at both mooring locations. During stratified conditions throughout August, the theoretical and modeled transports are very similar at 21 m. At 8 m, the modeled transports are smaller, consistent with the values of T_+ increasing offshore. Consequently, the August 15 upwelling event at the top of Figure 13 shows comparable values of T_+ and $\tau^y/\rho_0 f$ offshore of 6 km (15 m depth).

In October, when the shelf is weakly stratified, the offshore Ekman transport is significantly larger than T_+ during three periods (October 12, October 14-18, and October 28-29), all strong downwelling events. The event on October 12 is shown

at the top of Figure 13 with much larger Ekman transport than T_+. The vertical diffusion of momentum is important throughout the water column during these periods (Figure 12), in contrast to the stratified periods during which it is restricted to the surface and bottom Ekman layers.

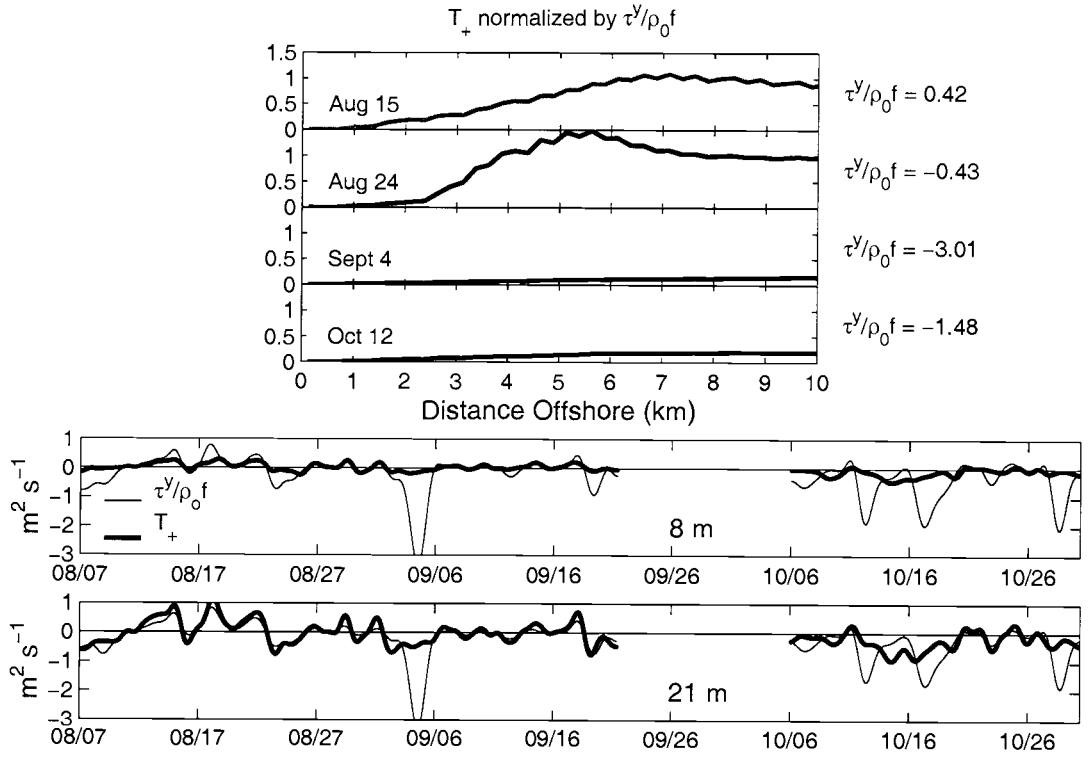

Figure 13. Total offshore transport, T_+, calculated from modeled across-shelf velocities and normalized by the Ekman transport. Positive values, denoted by a gray line (15 Aug), indicate offshore transport in the surface layer. Negative values, denoted by a black line, indicate offshore transport in the bottom layer. The value given to the right of each day is the Ekman transport value. Plotted below is the low-pass filtered time series of theoretical Ekman transport (thin line) and model-calculated total offshore transport (thick line) at 8 m (top) and 21 m (bottom) ($m^2\ s^{-1}$).

Similar results were found first by Lentz (2001) using across-shelf transports calculated from the mooring data in the CoOP experiment. He estimates the

resulting dependence of the across-shelf transport on $\tau^{sy}/\rho_0 f$ for stratified and unstratified conditions. The numerical model used in this study allows for the direct calculation of across-shelf transport and vertical stress fields. The results show that following the stratification breakdown on September 4, the across-shelf transport is significantly less than the theoretical Ekman transport for strong winds (Figure 13). The vertical mixing in the interior also increases during these conditions (Figure 12). This is consistent with the conclusions of Lentz (2001).

2.6 Lagrangian Analysis

2.6.1. Lagrangian Label Fields

In order to understand the impact of wind events on model water parcels on the shelf, we examine the Lagrangian labels and parcel trajectories described in Section 2.4.3 during August and October. Comparison of the X and Z distributions throughout August (Figure 14) and October (Figure 16) with the initial distribution (top row) shows significant motion across the shelf and vertically. The label Y, plotted as distance in km for parcels initially at $y = 0$ (Eq. 5), shows alongshelf motion of up to 40 km in each direction. During the first few days of August, when downwelling winds persist, parcels in the surface layer are advected onshore from x=50 km to x=10 km, vertically downward to 25 m depth near the coast, and southward 40 km. The interaction between downwelling and upwelling responses results in complex features, such as the filament of high X values that remains onshore at depths of 5–10 m after downwelling at the beginning of August. Although the filament retreats slightly on August 19–23 during upwelling, it grows again on August 27 as downwelling winds return. This feature corresponds to the

large positive Y values (southward advection) in the same location, also due to downwelling. The low X values that begin the simulation onshore of 10 km also experience significant across-shelf, alongshelf, and vertical motion. The location of these X values near the coast on August 27 corresponds with large negative Y values (northward advection), illustrating that parcels in this region are being advected northward 40 km, as well as being pushed upward and offshore. In Z, a filament of high Z values upwells to the surface on August 19–23 and remains near the surface on August 27 after the onset of downwelling winds.

The difference in surface Ekman layer thickness during upwelling and downwelling (Figure 14) is an additional example of asymmetry between upwelling and downwelling responses. This is also observed in the mean Eulerian velocities (Figure 6). While differences in stratification play an important role in the dynamical contrasts between August and October seen in Figure 6, the stratified shelf in August reacts differently to upwelling and downwelling. On August 11, the surface layer extends to 10 m depth during downwelling forcing. On August 23, the surface layer is only about half as deep during upwelling forcing of similar magnitude and duration.

We examine the impact of the September 4 storm on the motion of model water parcels by initializing the Lagrangian label fields on September 1 and following their evolution through September 5 (Figure 15). The storm has a significant effect on the motion of model water parcels. Surface parcels are moved up to 40 km onshore during September 2–5 and parcels from the coast to 40 km offshore are moved down as much as 20 m. Water parcels in the bottom layer move as much as 30 km offshore, as shown in the filament of blue X values on September 4–5. We also

utilize the storm period to compare the time evolution of the label fields with that of passive tracer fields that directly feel the effects of model-parameterized vertical turbulent mixing. Three passive tracer fields are initialized on September 1 in the same manner as the label fields. The results of this experiment are shown in the right columns of Figure 15. A comparison of the evolution of the label and the tracer fields illustrates the differences in their behavior. The apparent across-shelf motion is greatly decreased for the tracers and occurs in vertically mixed surface and bottom layers. Filament structures such as those shown for the labels do not develop in the across-shelf direction. However, isolated features extending in the vertical are apparent for the tracers on September 4 and 5. The yellow feature on September 4 located about 20 km offshore corresponds to a downward bend in the contours of the label X in the far left column. Similarly, a dark red feature in the X tracer on September 5 at 40 km offshore corresponds to a feature extending to 30 m depth in the X label. Advection is responsible for the across-shelf movement of the labels; the small-scale structures result due to across-shelf and vertical variability in model velocities. The Z tracer field shows the results of offshore advection of water parcels in the bottom 20 m on September 3–5 and vertical mixing onshore. Turbulent mixing processes in the tracer equations act to break down the vertical structure that appears in the label fields, but the X tracer examples show that filament-like features may still develop in the tracer fields.

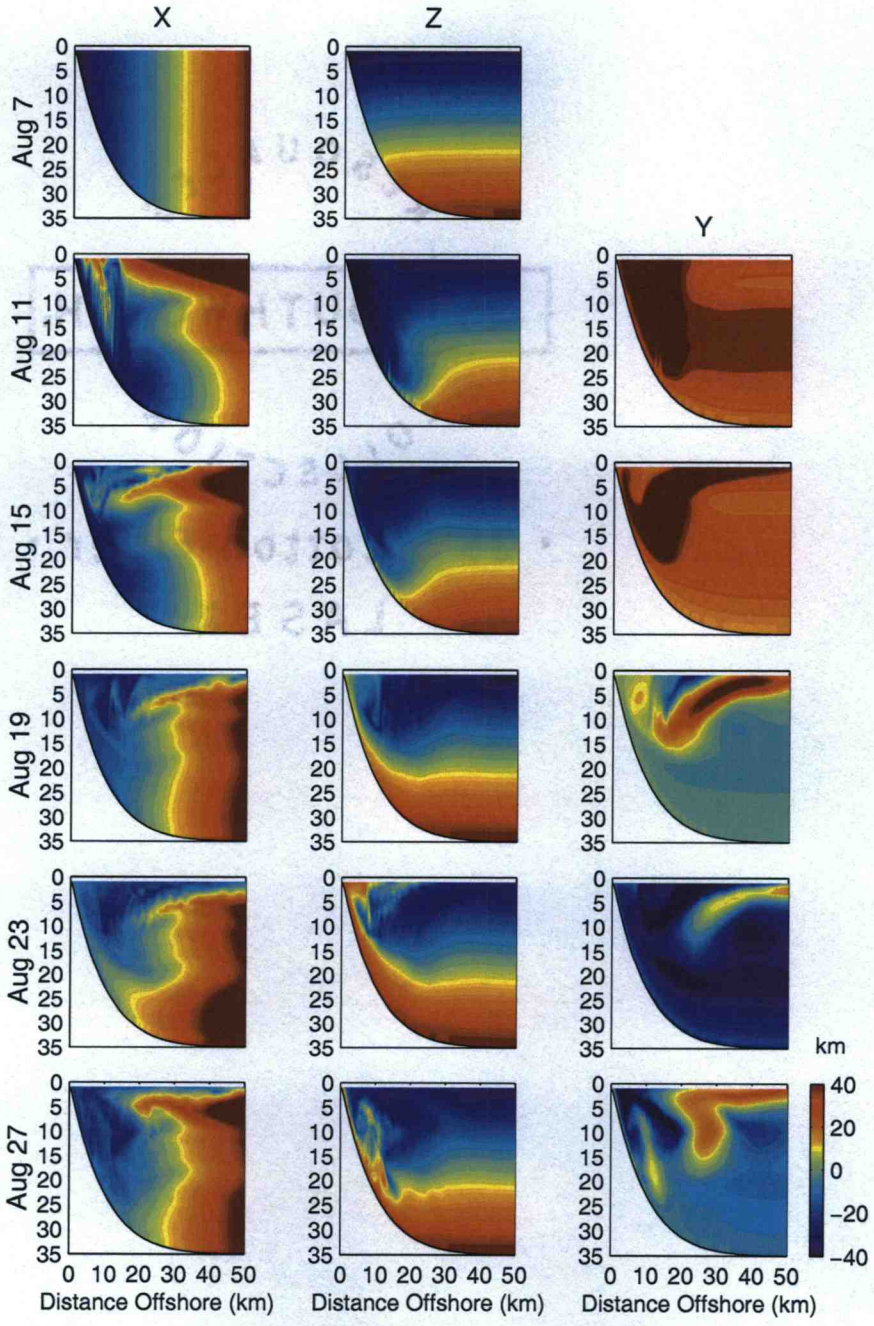

Figure 14. Contours of X (left), Z (center), and Y (right) for selected days in Aug. The simulation begins at 0100 UTC 7 Aug 1994. The initial field for Y is zero. The colorbar is for the Y label only.

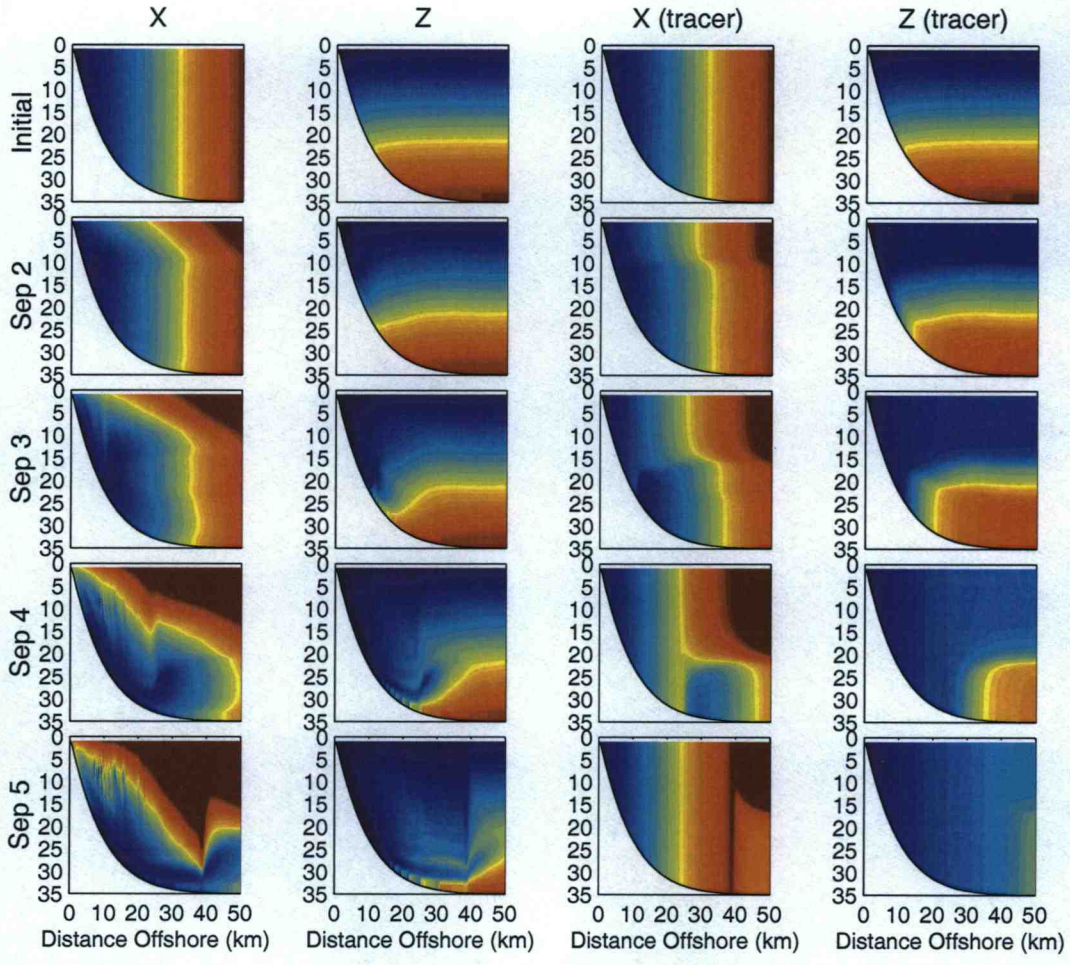

Figure 15. Contours of the X and Z label fields (two left columns) and passive tracers (two right columns) during the 2–5 Sept event. The labels and tracers are initialized with the distribution shown in the top row at 1200 UTC 1 Sept.

In October, the motion of parcels reflects the dominance of downwelling winds (Figure 16). High X values initially at 30–50 km in the surface layer move all the way to the coast and are then advected vertically downward, as seen on October 18. The Y label shows the development of a wide region of southward alongshelf velocities extending from 20 km offshore and from the surface to 25 m depth. A striking response of the low X values initially within 10 km of the coast, and the low Z values initially within 10 m of the surface, to the persistent downwelling winds

is also seen on October 18–26. As parcels in these regions are advected downward and offshore, a small patch is advected upward again at about 20 km offshore. This patch becomes trapped in the interior region. Meanwhile, the surface fluid continues to be advected onshore and the bottom fluid offshore. By October 26, almost all of the Z values initially below 20 m have been advected offshore of 40 km. The region onshore of these Z values on October 26 corresponds to smaller values of southward advection in Y. The parcels that are being advected vertically down the shelf and offshore in the bottom layer by downwelling forcing are advected less in the alongshelf direction than those parcels being pushed onshore in the surface layer.

2.6.2. Lagrangian Mean Velocities

Lagrangian mean velocities at time t for a fluid parcel with coordinates $(x(t), y(t), z(t))$, located initially at $(x(0), y(0), z(0))$, are given by

$$u_l(t) = \frac{x(t) - x(0)}{t}, \quad v_l(t) = \frac{y(t) - y(0)}{t}, \quad w_l(t) = \frac{z(t) - z(0)}{t}. \tag{11}$$

The Lagrangian mean velocities are contoured as a function of $(x(0),z(0))$ for the months of August (Figure 17) and October (Figure 18). In the dynamical systems field, this type of presentation is labeled a 'mean-velocity patchiness' (Malhotra et al. 1998) plot. These plots are created from both the trajectories of the parcels (rows 1 and 3) and the final distribution of the X, Z and Y labels (rows 2 and 4). For each method, the mean velocity is contoured as both a function of its initial position $(x(0),z(0))$ (top 2 rows) and also of its final position $(x(t),z(t))$ (bottom 2 rows). This presentation provides two different perspectives on the mean motion of fluid parcels. One can determine both the mean velocity of a parcel initialized at a given location and the mean velocity of a parcel that ends up in a given location.

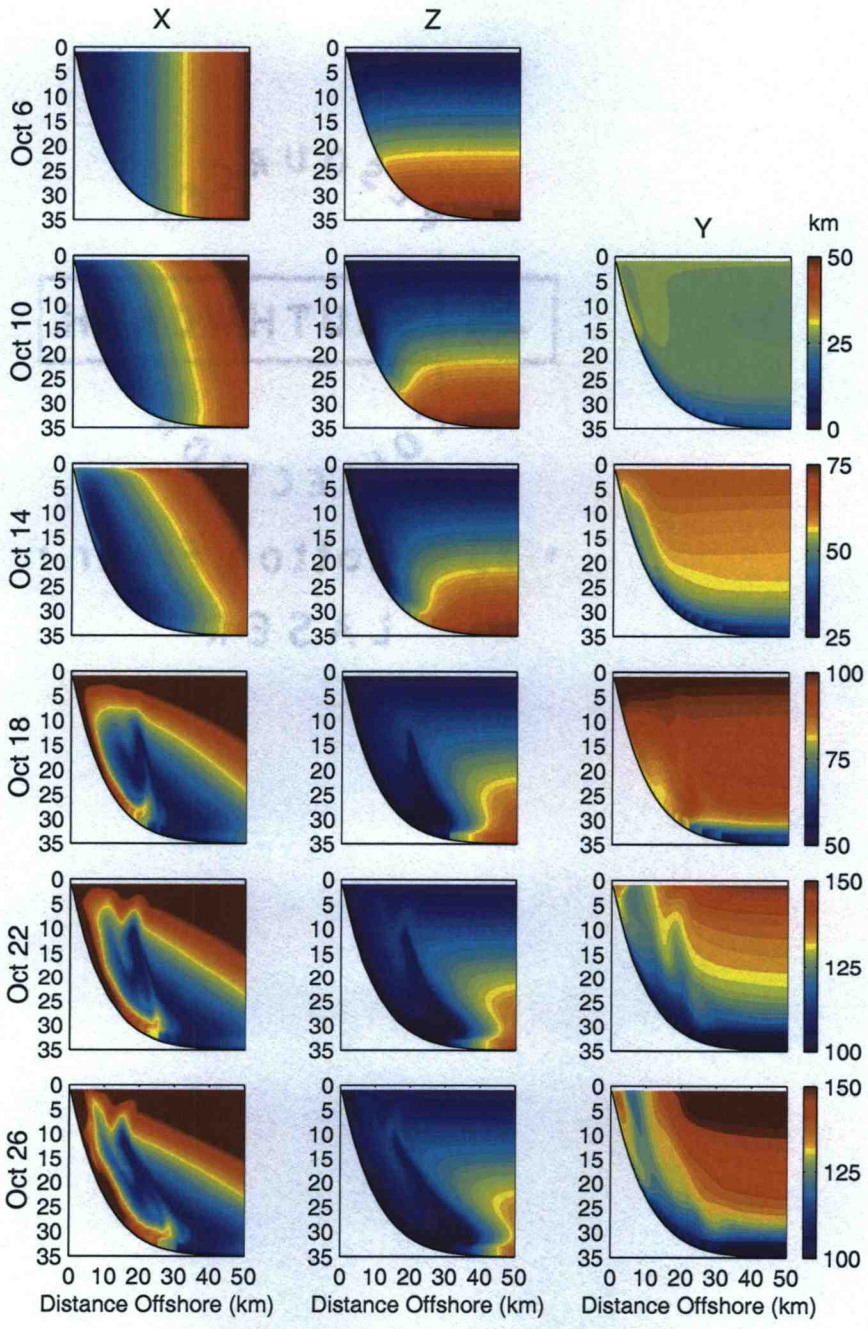

Figure 16. Contours of X (left), Z (center), and Y (right) for selected days in Oct. The simulation begins at 0100 UTC 6 Oct 1994. The initial field for Y is zero. The colorbar is for the Y label only.

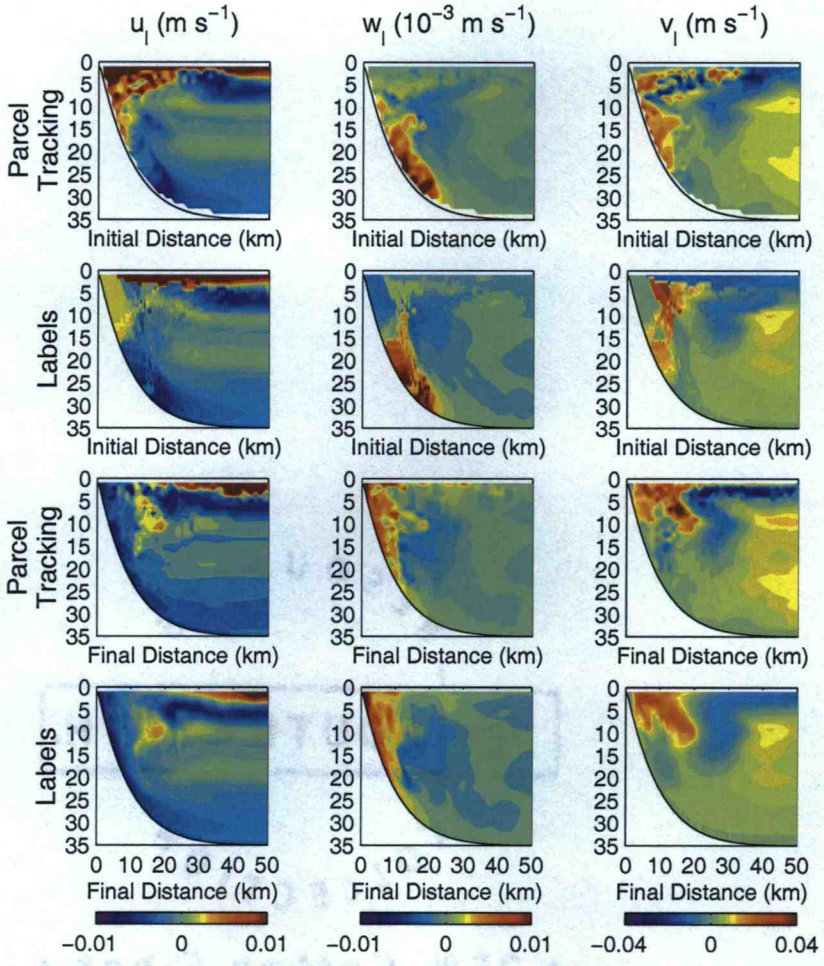

Figure 17. Lagrangian mean velocities for the month of Aug obtained from parcel trajectories (rows 1 and 3) and from the Lagrangian label fields (rows 2 and 4). The Lagrangian mean velocities are plotted as functions of both initial and final positions.

An important characteristic to notice is the general similarity between the parcel tracking and label methods, giving confidence in the consistency of the Lagrangian parcel tracking scheme and the label advection technique. As a check, additional parcel tracking experiments were performed by adapting a fourth-order Milne Predictor-Hamming Corrector method implemented in the Regional Ocean Model System (ROMS) for use here. Differences in Lagrangian mean velocities obtained from the Runge-Kutta and Milne-Hamming methods were small compared to the velocity magnitudes.

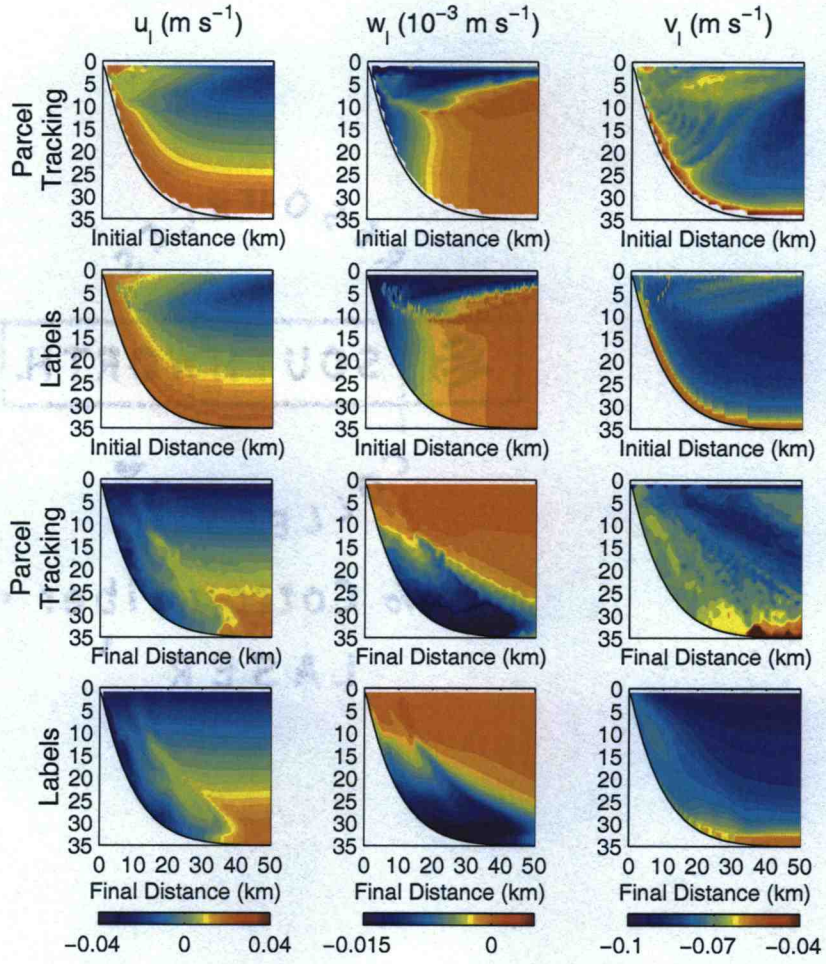

Figure 18. Lagrangian mean velocities for the month of Oct obtained from parcel trajectories (rows 1 and 3) and from the Lagrangian label fields (rows 2 and 4). The Lagrangian mean velocities are plotted as functions of both initial and final positions.

In the patchiness plots, areas of significantly different mean velocity from the surrounding region are called patches. Patches can give insight into some important aspects of the Lagrangian characteristics of the flow, such as locations in which fluid parcels disperse at higher speeds and the presence of coherent structures (Malhotra et al. 1998). In our application, we identify patches resulting from the numerical simulation of wind-driven flows, and attempt to understand the significance of these patches and their locations in terms of the Eulerian dynamics discussed in Section

2.5.2. In August (Figure 17), three distinct regions of significant Lagrangian mean velocity are apparent as a function of initial position. In the top 5 m, the mean u_l is large and positive and v_l is large and mostly negative. Regions of opposite sign of both u_l and v_l are present just below this surface layer. A large patch of positive w_l near the coast from 10 m to 30 m depth coincides with a patch of negative u_l. These patches are also present when the velocities are contoured as a function of final position. A comparison of the initial and final position plots allows a straightforward look at where patches, beginning at some initial location on the shelf, were displaced. The patch of positive u_l in the surface layer is displaced offshore, illustrating that these parcels are advected offshore about 50 km over the August period. The region of negative u_l below this is displaced only about 10 km onshore of its initial location because it is advected onshore at a much slower mean velocity. The positive w_l patch near the coast is found from the surface to 15 m depth, having been advected upward and onshore by upwelling velocities during August.

The resulting 3D response of fluid parcels to upwelling and downwelling winds in August is thus the following: parcels originating in the patch from 5 km to 20 km offshore and extending 5 m from the bottom are advected upward and onshore; parcels originating in the top 5 m are advected offshore and southward; and parcels originating just below this surface layer and onshore of 20 km are advected offshore and northward, while parcels originating below the surface layer and offshore of 30 km are advected onshore and southward. The existence of a region of onshore and southward mean velocity near the surface is a result of the downwelling winds. There are also parcels that move downward. The label and parcel tracking results both show a region of negative w_l offshore of the large positive patch. This downwelling

patch is offshore of the upwelling patch because the downwelling response extends farther offshore than the upwelling response. The magnitude of the downwelling vertical velocities is less than that of the upwelling vertical velocities because upwelling dominates during the month of August. However, the dominant upwelling forcing does not obscure the effect of downwelling in this region.

In October (Figure 18), the existence of patches is less clear because of the persistence of downwelling winds, and hence, the overall larger range of mean Lagrangian velocities compared to August. A region of large negative u_l is found for initial positions in the top 10 m offshore of 30 km, but the positive u_l values in the bottom layer occur over a much broader region in both x and z. There is also a patch of significant downward vertical velocity in the top 5 m. A patch is not obvious in the mean alongshelf velocity on the scale shown, though evidence of larger v_l is seen below 5 m and offshore of 30 km in the labels. This is the signature of a patch that exists from 30 km offshore to 200 km, the model boundary, signifying the southward movement of parcels in this region. In the plots as a function of final position, the surface negative u_l region extends offshore of the coastal boundary and the positive u_l patch in the bottom is offshore of 30 km. In contrast with August, this illustrates a more nearly symmetric response of parcels in the surface and bottom layers, which are advected about the same distance over similar layer depths. The negative w_l patch is found from 25 m depth to the bottom as these parcels were advected downward along the entire sloping extent of the shelf (from 0 to 30 km offshore) during October. This downwelling response can be seen in the alongshelf Lagrangian velocity also. The final position of the region of v_l=-0.07 m s^{-1} that is initially near the surface is near the bottom and slightly offshore, illustrating the same pattern as

found in the vertical Lagrangian velocity.

In October, parcels originating in the offshore surface region are thus advected onshore and southward, and parcels originating onshore of this patch in the surface are advected downward. Clearly, since the parcels in the October simulation are subject to a much more consistent forcing of downwelling winds than those in August, the Lagrangian behavior in October is more straightforward.

2.7 Summary

The response on the continental shelf to upwelling and downwelling wind forcing is discussed and comparisons are made between modeled and observed fields. During stratified conditions in August, the mean upwelling response consists of a 5 m thick surface layer advected offshore and a bottom layer of onshore velocities extending from the coast to 20 km offshore. A northward coastal jet is also present from the coast to 20 km offshore. The presence of intermittent downwelling winds complicates the overall dynamics in August. During unstratified conditions in October, the downwelling response is 15 m thick surface (onshore advection) and bottom (offshore advection) layers and southward alongshelf velocities everywhere on the shelf, with the largest values at the surface offshore of 20 km. Asymmetries between the upwelling and downwelling response include a deeper surface mixed layer during downwelling and significant contribution of the nonlinear advection terms to the alongshelf momentum balance in depths less than 10 m during upwelling, but not during downwelling. In each month the region of high density variability extends from the coast to 10 km offshore and high alongshelf velocity variability from the coast to 20 km.

The details of a strong downwelling wind event during September 4–5 illustrate offshore advection of the density front and a shutdown of the across-shelf circulation in the region onshore of the front, where the water column is well-mixed. The results from the downwelling event are in general agreement with those from the idealized downwelling study of Austin (1998). The dominant alongshelf momentum balance is between the Coriolis and vertical diffusion terms, with a slight contribution from acceleration and advection. The surface and bottom Ekman layers grow throughout the event and merge in the region of the front. The vertical diffusion and advection of temperature dominate the balance in the temperature equation during this event, with a contribution from the tendency term in the frontal region. This event and other downwelling events in October are characterized by a decreased transport relative to the theoretical Ekman transport in both the surface and bottom layers.

In addition to the Eulerian analysis, the Lagrangian aspects of the shelf flow are explored. This is accomplished by utilizing the Lagrangian information that is directly available from the model solutions, i.e., by calculating the motion of idealized fluid parcels that are advected by the model-resolved velocity field. Since small-scale turbulence is parameterized in the model, the direct effect of turbulence on fluid parcel trajectories is not represented. Nevertheless, determination of the model parcel trajectories provides new information about the three-dimensional Lagrangian characteristics of the model shelf flows that complements that obtained from the Eulerian analysis. The Lagrangian results give a useful, but incomplete, quantitative measure of fluid parcel displacements; the corresponding transport of passive tracers would be complicated by the effects of small-scale turbulent mixing processes. Two Lagrangian techniques are employed. These techniques produce similar results for

the mean motion over each month of August and October, providing support for the Lagrangian label approach as a method for tracking fluid parcels. The label fields display significant advection in all three dimensions. In August, surface fluid is advected from the coast to 50 km offshore. The surface fluid initially within 20 km of the coast is advected northward about 100 km, while that initially offshore of 20 km is advected southward about 80 km. Deep fluid is advected upward and onshore near the coast. In October, fluid is advected as far as 100 km onshore in the top 10 m and 100 km offshore in the bottom 10 m. Southward displacements of up to 150 km are found, and fluid initially within 5 m of the surface and 20 km of the coast is advected downward and offshore along the sloping bottom boundary.

2.7 Acknowledgments

This research was supported by the Office of Naval Research (ONR) Coastal Dynamics Program through grants N00014-93-1-1301 and N00014-02-1-0100. Additional support was provided for R.M.S. by the ONR Ocean Modeling and Prediction Program through ONR grant N00014-98-1-0813. We thank S. Lentz and S. Elgar for making the CoOP data available, J. Austin for providing the data and for several helpful suggestions, and P. Newberger for invaluable assistance with use of the Princeton Ocean Model. The authors also thank two anonymous reviewers for useful comments.

2.8 References

Alessi, C.A., S.J. Lentz, and J. Austin, 1996: Coastal Ocean Processes Inner-Shelf Study: Coastal and moored physical oceanographic measurements, *Tech. Rep. WHOI-96-06*, Woods Hole Oceanogr. Inst., Woods Hole, MA, 142 pp.

Austin, J.A., 1998: Wind-driven Circulation on a Shallow, Stratified Shelf, *Ph.D. Thesis*, MIT/WHOI, 246 pp.

Austin, J.A., 1999: The role of the alongshore wind stress in the heat budget of the North Carolina inner shelf, *J. Geophys. Res.*, **104**, 18,187-18,203.

Austin, J.A. and S.J. Lentz, 1999: The relationship between synoptic weather systems and meteorological forcing on the North Carolina inner shelf, *J. Geophys. Res.*, **104**, 18,159-18,185.

Austin, J.A. and S.J. Lentz, 2002: The Inner Shelf Response to Wind-driven Upwelling and Downwelling, *J. Phys. Oceanogr.*, **32**, 2171-2193.

Blumberg, A.F. and G.L. Mellor, 1987: A Description of a Three-Dimensional Coastal Ocean Circulation Model, *Three-Dimensional Coastal Ocean Models*, Coastal and Estuarine Science Series, Vol. 4, N. Heaps Ed., Amer. Geophys. Union, 1-16.

Butman, C.A., 1994: CoOP: Coastal Ocean Processes Study - Interdisciplinary approach, new technology to determine coupled biological, physical, geological processes affecting larval transport on inner shelf, *Sea Technol.*, **35**, 44-49.

Chen, C. and R.C. Beardsley, 1998: Tidal mixing and cross-frontal particle exchange over a finite amplitude asymmetric bank: A model study with application to Georges Bank, *J. Mar. Res.*, **56**, 1163-1201.

Dever, E.P., 1997: Wind-Forced Cross-Shelf Circulation on the Northern California Shelf, *J. Phys. Oceanogr.*, **27**, 1566-1580.

Galperin, B., L.H. Kantha, S. Hassid, and A. Rosati, 1988: A quasi-equilibrium turbulent energy model for geophysical flows, *J. Atmos. Sci.*, **45**, 55-62.

Large, W.G. and S. Pond, 1981: Open Ocean Momentum Flux Measurements in Moderate to Strong Winds, *J. Phys. Oceanogr.*, **11**, 324-336.

Lentz, S.J., 2001: The Influence of Stratification on the Wind-Driven Cross-shelf Circulation over the North Carolina Shelf, *J. Phys. Oceanogr.*, **31**, 2749-2760.

Lentz, S.J., R.T. Guza, S. Elgar, F. Feddersen, and T.H.C. Herbers, 1999: Momentum balances on the North Carolina inner shelf, *J. Geophys. Res.*, **104**, 18,205-18,226.

Malhotra, N., I. Mezic, and S. Wiggins, 1998: Patchiness: A New Diagnostic for Lagrangian Trajectory Analysis in Time-Dependent Fluid Flows, *Int. J. Bifurcation and Chaos*, **8**, 1053-1093.

Mellor, G.L. and T. Yamada, 1982: Development of a Turbulence Closure Model for Geophysical Fluid Problems, *Rev. Geophys. and Space Phys.*, **20**, 851-875.

Rennie, S.E., J.L. Largier, and S.J. Lentz, 1999: Observations of a pulsed buoyancy current downstream of Chesapeake Bay, *J. Geophys. Res.*, **104**, 18,227-18,240.

Smolarkiewicz, P.K., 1983: A Simple Positive Definite Advection Scheme with Small Implicit Diffusion, *Mon. Wea. Rev.*, **111**, 479-486.

Taylor, G.I., 1953: Dispersion of solute matter in solvent flowing slowly through a tube, *Proc. Roy. Soc.* (London), Series A, **219**, 186-203.

Taylor, G.I., 1954: The dispersion of matter in turbulent flow through a pipe, *Proc. Roy. Soc.* (London), Series A, **223**, 446-468.

Waldorf, B.W., J.L. Largier, S. Rennie, J. Austin, and C. Greengrove, 1995: Coastal Ocean Processes (CoOP) pilot project data report: R/V *Cape Hatteras* shipboard measurements; underway, CTD, and ADCP data August 1994, *Tech. Rep. SIO Ref. Ser. 95-29*, Scripps Inst. of Oceanogr., La Jolla, CA, 419 pp.

Waldorf, B.W., J.L. Largier, S. Rennie, and J. Austin, 1996: Coastal Ocean Processes (CoOP) pilot project data report: R/V *Cape Hatteras* shipboard measurements; underway, CTD, and ADCP data October 1994, *Tech. Rep. SIO Ref. Ser. 96-9*, Scripps Inst. of Oceanogr., La Jolla, CA, 407 pp.

3 Lagrangian characteristics of continental shelf flows forced by periodic wind stress

Brandy T. Kuebel Cervantes, J. S. Allen, and R. M. Samelson

Nonlinear Processes in Geophysics

Max-Planck-Str. 13

37191 Katlenburg-Lindau, Germany

Vol. 11, February 2004

3.1 Abstract

The coastal ocean may experience periods of fluctuating alongshelf wind direction, causing shifts between upwelling and downwelling conditions with responses that are not symmetric. We seek to understand these asymmetries and their implications on the Eulerian and Lagrangian flows. We use a two-dimensional (variations across-shelf and with depth; uniformity alongshelf) primitive equation numerical model to study shelf flows in the presence of periodic, zero-mean wind stress forcing. The model bathymetry and initial stratification is typical of the broad, shallow shelf off Duck, NC during summer. After an initial transient adjustment, the response of the Eulerian fields is nearly periodic. Despite the symmetric wind stress forcing, there exist both mean Eulerian and Lagrangian flows. The mean Lagrangian displacement of parcels on the shelf depends both on their initial location and on the initial phase of the forcing. Eulerian mean velocities, in contrast, have almost no dependence on initial phase. In an experiment with sinusoidal wind stress forcing of maximum amplitude 0.1 N m^{-2} and period of 6 days, the mean Lagrangian across-shelf displacements are largest in the surface and bottom boundary layers. Parcels that originate near the coast in the top 15 m experience complicated across-shelf and vertical motion that does not display a clear pattern. Offshore of this region in the top 10 m a rotating cell feature exists with offshore displacement near the surface and onshore displacement below. A mapping technique is used to help identify the qualitative characteristics of the Lagrangian motion and to clarify the long time nature of the parcel displacements. The complexity of the Lagrangian motion in a region near the coast and the existence of a clear boundary separating this region from a more regular surface cell feature offshore are quantified by a

calculation from the map of the largest Lyapunov exponent.

3.2 Introduction

In this study we examine the Lagrangian characteristics of two-dimensional, time-periodic, wind-driven coastal flows. The wind-driven processes of upwelling and downwelling are of considerable interest to coastal oceanographers studying the physics and biology of these highly productive regions. Most modeling studies of coastal flows have been analyzed in terms of a traditional Eulerian formulation. The Lagrangian aspects of these flows typically have not been considered. A description of the Lagrangian behavior of wind-driven shelf flow has recently been pursued by Kuebel Cervantes et al. (2003), hereafter denoted as KC2003, which motivated this work. The study by KC2003 utilized numerical experiments to examine the Eulerian and Lagrangian characteristics of wind-driven coastal upwelling and downwelling forced by measured winds at Duck, North Carolina during the Coastal Ocean Processes (CoOP) Inner Shelf Study (ISS). The ISS took place off Duck from August–November 1994. Interesting Lagrangian behavior was found during the month of August that resulted from the varying alongshelf wind stress direction. The present study further investigates the impact of the fluctuating alongshelf winds on fluid parcels in the coastal ocean using periodic wind forcing with zero time mean. We use a Lagrangian parcel tracking technique to study fluid parcel displacements over one period and many periods, as well as to compute mean Lagrangian velocities. We also employ a technique utilized by KC2003 of advecting Lagrangian label fields by the model velocities for further Lagrangian analyses.

Eulerian dynamics are discussed as well. The Eulerian fields are approximately

periodic after an initial adjustment of a few periods. Although the forcing is periodic, mean Eulerian velocities exist after one period. Asymmetries between upwelling and downwelling, including the thickness of the surface and bottom mixed layers and the relative importance of nonlinear advection, were discussed by KC2003 and are revisited here.

The present investigation has relevance to two different scientific communities: coastal oceanography and dynamical systems. While these fields are traditionally unrelated, studies in recent years have bridged the gap between the two fields through the application of dynamical systems techniques to oceanographic flows. Ridderinkhof and Loder (1994) and Loder et al. (1997) identify hyperbolic fixed points and their associated stable and unstable manifolds in tidal flows over submarine banks. More recently, Poje et al. (2002) use an ocean model to determine optimal Lagrangian drifter launch sites by tracking hyperbolic points in the flow field and Kirwan et al. (2003) apply ideas of invariant manifolds to flow in the Gulf of Mexico using a data assimilating model. Early work combining fluid mechanics and dynamical systems, such as that of Weiss and Knobloch (1989) and Rom-Kedar et al. (1990), consider transport properties of fluid in modulated traveling waves and unsteady vortical flow, respectively. Many studies from the dynamical systems perspective, including Coulliette and Wiggins (2001), Miller et al. (1997), and Poje and Haller (1999), apply dynamical systems theory to study lobe geometry and dynamics and invariant manifolds in velocity fields from ocean circulation models. Most recently, these techniques have also been developed for application to two-dimensional time-dependent ocean velocity measurements (Ide et al., 2002 and Haller 2002). These examples indicate that the study of oceanic

flows using dynamical systems methods is clearly of interest to oceanographers and applied mathematicians, however coastal ocean flows over the continental shelf have generally not been the focus of these studies.

The outline of the paper is as follows. The numerical model methods and particle tracking techniques are described in Section 3.3. The dynamical analysis of the Eulerian mean velocity and momentum balance fields is discussed in Section 3.4. The Lagrangian results are presented in Section 3.5. A summary is given in Section 3.6.

3.3 Methods

3.3.1. Model Description

The numerical model is a two-dimensional version of the finite-difference Princeton Ocean Model (POM) (Blumberg and Mellor, 1987). The model equations are the hydrostatic primitive equations with the Mellor-Yamada (1982) turbulence closure scheme for vertical mixing, as modified in Galperin et al. (1988), embedded.

The model domain, described in terms of Cartesian coordinates (x, y, z), is a section with variations in the across-shelf (x) and vertical (z) directions. The flow is assumed to be uniform in the alongshelf (y) direction, so that the Eulerian variables have no y dependence. The velocity components in the (x, y, z) directions are (u, v, w). Note that although the flow is uniform in y, the alongshelf velocity component v is generally not zero. The domain is bounded by vertical walls at the coast and at the offshore boundary with boundary conditions of no flow in the across-shelf direction (u=0) and free-slip in the alongshelf direction ($v_x = 0$).

For application over variable bottom topography, the POM model is formulated

in sigma coordinates (x, y, σ). The relationship between σ and the Cartesian vertical coordinate z is given by

$$\sigma = \frac{z - \eta}{H + \eta}, \tag{12}$$

where $D = H + \eta$, $H(x)$ is the depth and $\eta(x, t)$ is the surface elevation, so that σ=0 at the surface ($z = \eta$) and σ=-1 at the bottom ($z = -H$). Consequently, when discretized, the same number of σ levels exist independent of the local depth and the vertical resolution increases as the depth decreases. In σ coordinates, ω is a velocity normal to σ surfaces that enters the equations naturally and replaces the vertical velocity w. The relationship between ω and w is

$$\omega = w - u(\sigma\frac{\partial D}{\partial x} + \frac{\partial \eta}{\partial x}) - \sigma\frac{\partial D}{\partial t} - \frac{\partial \eta}{\partial t}. \tag{13}$$

In the analysis of model solutions, we present the results in terms of the original Cartesian coordinates to facilitate physical interpretation.

3.3.2 Model Setup

The model bathymetry, initial stratification, and forcing correspond to August conditions observed at Duck during the ISS. The initial state of the model experiments is a coastal ocean at rest with horizontally uniform temperature and salinity fields compiled from the horizontal average of those observed with an across-shelf mooring array at Duck on 7 August 1994. The model is forced by a sinusoidal, spatially independent wind stress component τ^{sy} and by constant heat flux components (shortwave radiative heat flux, Q_{sw}, and the sum of the longwave and turbulent fluxes, Q_{lw}+Q_{sen}+Q_{lat}) computed from the mean heat flux values observed at Duck in August (Austin and Lentz 1999). The period of τ^{sy} is chosen

to be 6 days based on the approximate period of maximum wind-forced energy observed during August. The maximum amplitude of τ^{sy}, 0.1 N m^{-2}, is also typical of August values.

The model bathymetry is characteristic of that off Duck with a relatively steep slope from the coast to about 20 m depth and a gradual slope offshore of the 20 m isobath. The model domain extends from the coastal boundary to a distance of 200 km offshore, with constant water depth of 35 m offshore of 40 km. A uniform grid spacing is used in x with a resolution of 250 m and in σ with 30 σ levels. The horizontal kinematic eddy viscosity and diffusivity are chosen to be small constant values, $A_M = A_H = 2$ m^2 s^{-1}. The background vertical viscosity ν_M and diffusivity ν_H are set to 2.0×10^{-5} m^{2}s^{-1}. The model has both an "external" time step to integrate the barotropic (depth-integrated) momentum equations and an "internal" time step to integrate the baroclinic (depth-dependent) momentum equations. The external time step is 5 s and is governed by fast surface waves, whereas the internal time step is much longer, 75 s, because the baroclinic response is governed by slower internal waves.

The model is spun up for several forcing periods after which the Eulerian fields are nearly periodic. In Section 3.5.2, we present results for parcels initialized at different phases in the forcing period. The net parcel displacements and Lagrangian mean velocities over one period are highly sensitive to this initial phase. Results from the model simulations are referenced according to the start time, t_i, given as the number of periods in the long spinup run. Results will be presented for four different initialization times; t_i=8.5T, t_i=8.75T, t_i=9T, and t_i=9.25T (Figure 19). Most of the results will focus on the simulation beginning at t_i=9.25T, at which time the

wind forcing is in the middle of an upwelling-favorable half-cycle and the amplitude is maximum. The near periodicity of the Eulerian fields after several forcing periods is illustrated by the time-dependence of the depth-averaged alongshelf velocity in 8 m water depth during a 9-period spinup run in Figure 20. The density values (not shown) decrease slightly with each period due to positive surface heat flux forcing, however the vertical gradient in density remains nearly periodic.

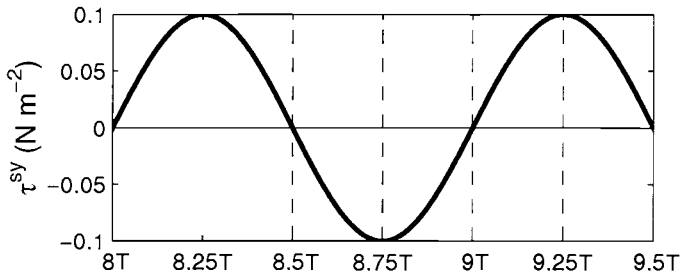

Figure 19. Sinusoidal alongshelf wind stress forcing for a portion of the spinup run duration (shown after 8 periods). The dotted lines show the times in the forcing period at which model simulations with t_i=8.5T, t_i=8.75T, t_i=9T, and t_i=9.25T are initialized.

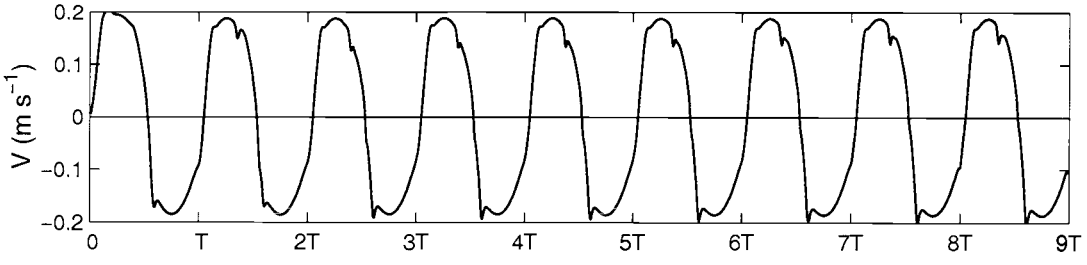

Figure 20. Depth-averaged alongshelf velocity at 8 m depth (approximately 2.7 km from the coast) for a 9-period spinup run.

Contour plots of the Eulerian across-shelf velocity u, alongshelf velocity v, and potential density σ_θ during a simulation beginning at t_i=9.25T show the evolution of the model fields over a forcing period (Figure 21). The upwelling response of u with offshore flow in the surface and onshore flow in the bottom boundary layers is apparent initially at 9.25T. The v field shows a northward coastal upwelling jet and σ_θ shows most of the isopycnals intersect the bottom and a few intersect the surface. The across-shelf flow then weakens and shifts to downwelling with surface onshore flow and offshore flow in the bottom layer at 9.75T. The u field at 9.75T is not equal and opposite that at 9.25T, but is characterized by a slightly thinner surface layer from 10-20 km offshore and a more structured flow below the surface layer inshore of 20 km. Differences in the structure of u during transition between upwelling and downwelling conditions are seen at 9.5T and 10T. The alongshelf velocity changes rather suddenly from northward at 9.5T to southward at 9.75T. The isopycnals are upwelled along the bottom at 9.5T and then move back down the shelf at 9.75T. After 9.75T, the across-shelf flow weakens again and returns to the upwelling response at 10.25T. The alongshelf velocity also becomes dominantly northward once again and the isopycnals return to their initial location at 9.25T.

Time series of the Eulerian fields during a 10 period simulation beginning at t_i=9.25T reveal the nearly periodic nature of the flow (Figure 22). The area-averaged alongshelf velocity, defined as

$$\overline{v} = \frac{1}{A}\int_0^{x_b}\int_{-H}^{\eta} v dx dz, \tag{14}$$

where A is the cross-sectional area of the model domain, follows the sinusoidal wind forcing with a lag of about 19 hours, which is approximately the inertial period $2\pi/f$. A slight increase in the maximum magnitude of $\overline{v}$ during upwelling forcing

relative to downwelling forcing is seen. This difference magnifies when v is squared (third panel); $\overline{v^2}$ is significantly higher during upwelling than during downwelling. The plot of $\overline{v^2}$ also reveals more clearly than the plot of $\overline{v}$ that the periodicity is only approximate.

A phase-plane diagram of the area-averaged kinetic energy $\overline{KE}$ versus the time derivative of kinetic energy $\partial\overline{KE}/\partial t$ (Figure 22, bottom panel) shows the difference in upwelling and downwelling energy responses. The area-averaged kinetic energy is calculated as

$$\overline{KE} = \frac{1}{A}\int_0^{x_b}\int_{-H}^{\eta}\frac{1}{2}(u^2+v^2)dxdz. \tag{15}$$

A time series of $\overline{KE}$ is very similar to the time series of $A^{-1}\int\int v^2 dxdz$ since $A^{-1}\int\int u^2 dxdz$ does not make a significant contribution. For the cycle beginning at t_i=9.25T, the time derivative of $\overline{KE}$ decreases from the initial time to the value at $t = t_i + T/4$, at which point the wind stress becomes negative. The time derivative of $\overline{KE}$ then increases until $t = t_i + T/2$, the point of maximum wind stress in the downwelling forcing phase. This kinetic energy cycle repeats approximately for the next half period. Thus, at every $t = t_i + nT/4$, when τ^{sy} is either at a maximum/minimum value or $\tau^{sy} = 0$, there is a transition in the rate of increase or decrease of the total energy. Note that in the phase-plane diagram the final point of the cycle does not coincide exactly with the initial point, although it is close, again demonstrating the approximate periodicity of the motion.

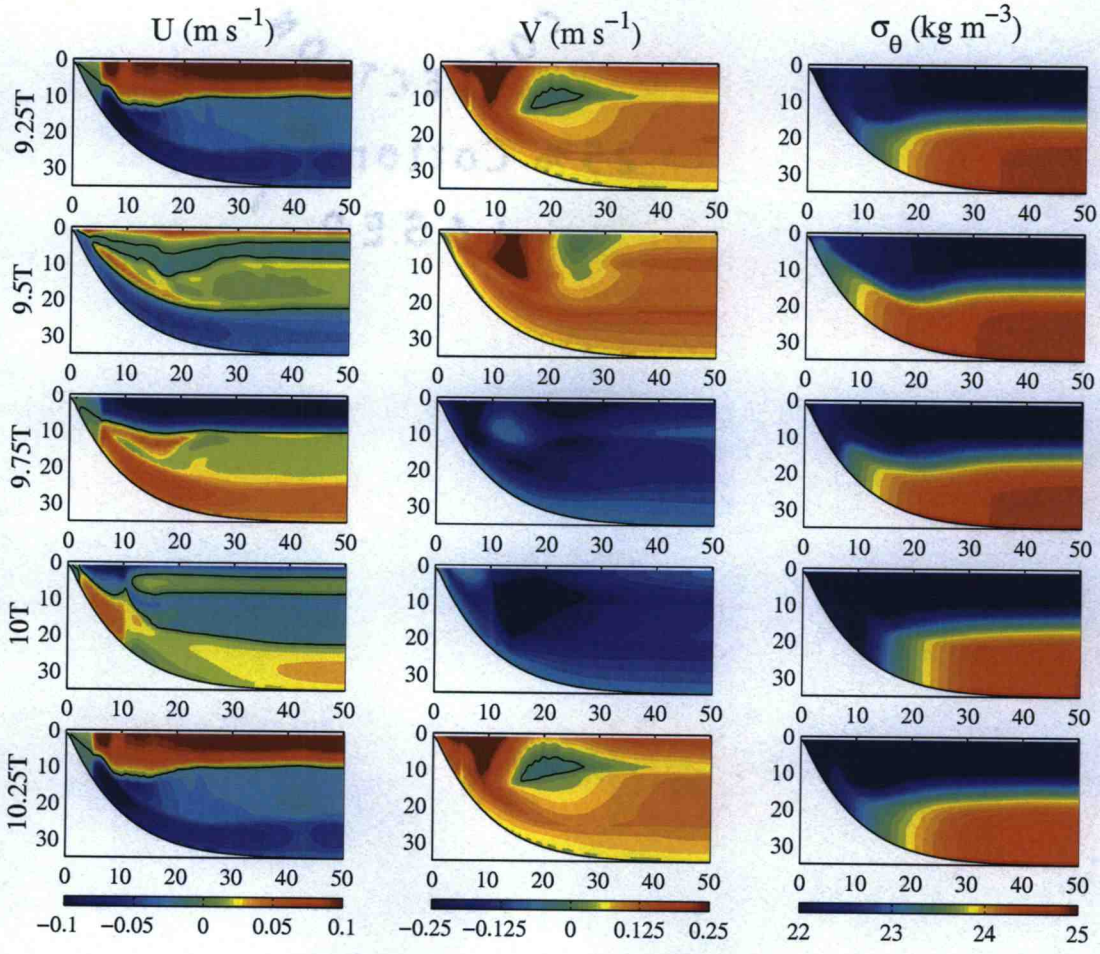

Figure 21. Eulerian across-shelf velocity u, alongshelf velocity v, and potential density σ_θ during one period beginning at t_i=9.25T. The black line denotes the 0 contour for u and v.

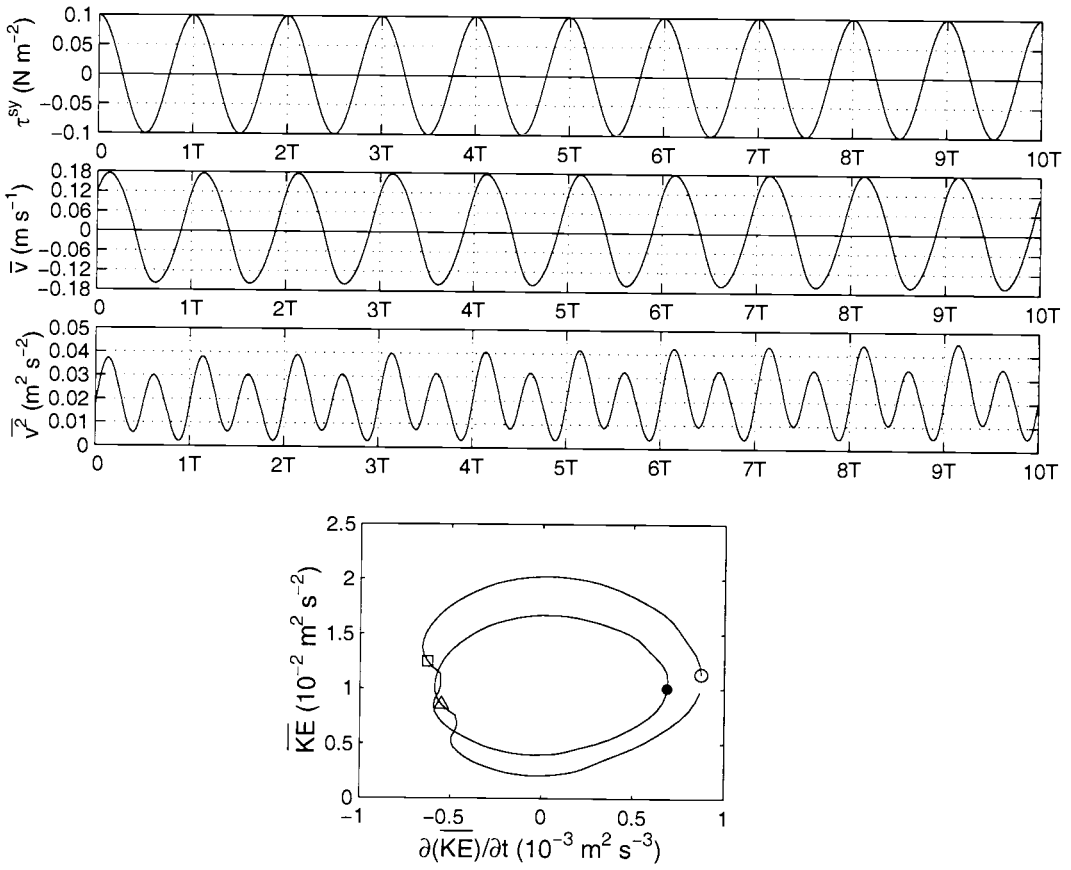

Figure 22. Top three panels are time series of alongshelf wind stress (top), area-averaged alongshelf velocity (Eq. 14)(middle), and area-averaged alongshelf velocity squared (bottom) during a 10 period simulation beginning at t_i=9.25T. Bottom panel is the area-averaged kinetic energy $\overline{KE}$ (Eq. 15) vs. the time derivative $\partial\overline{KE}/\partial t$ for the first period during the same simulation. The symbols in the bottom right plot correspond to t_i=9.25T (open circle), t_i+T/4 (square), t_i+T/2 (filled circle), and t_i+3T/4 (triangle).

3.3.3 Lagrangian Techniques

We utilize the Lagrangian information that is directly available from the model and consider the motion of model fluid parcels that are advected by the model-resolved velocity field. Since the model also includes a parameterization of small-scale turbulence, these Lagrangian parcel trajectories comprise only the resolved part of the full fluid motion represented in the model.

Lagrangian fluid motion is calculated using two different techniques. The first approach involves computing parcel trajectories by solving the differential equations

$$\frac{dx}{dt} = u, \qquad \frac{dy}{dt} = v, \qquad \frac{d\sigma}{dt} = \frac{\omega}{(H+\eta)}. \tag{16}$$

Parcels are indexed by their initial positions on the model grid of 30 σ levels and 800 x positions. We require the parcels to stay within the grid at which the interior Eulerian velocities are defined so that they remain at least $\Delta\sigma/2$ from the surface and bottom boundaries and $\Delta x/2$ from the coast and offshore boundaries. Numerical solutions to Eq. 16 are calculated utilizing a fourth-order Runge-Kutta scheme for x and σ and a backward Euler method for y. The time step used for the Runge-Kutta scheme is the model internal time step (Δt_i). To determine the effect of the time step used to solve Eq. 16, we also computed results using $\Delta t = \Delta t_i/2$, which involves interpolation of the model velocities to this time. The results were quantitatively similar for both cases.

The updated positions obtained by solving Eq. 16 are saved hourly for each initial parcel position. Interpolation of all three components of velocity to the parcel positions after each iteration is bilinear. Lagrangian results from additional experiments using bicubic interpolation of the velocity fields to the parcel positions were quantitatively similar to those using bilinear interpolation. Although many of

the model parcel paths exhibit considerable complexity, they are closely similar from one period to the next (Figure 23). The only region in which significant discrepancy exists is near the coastal boundary from about 5-15 m depth. This region will be shown in Section 3.5 to produce complex and irregular parcel displacement patterns.

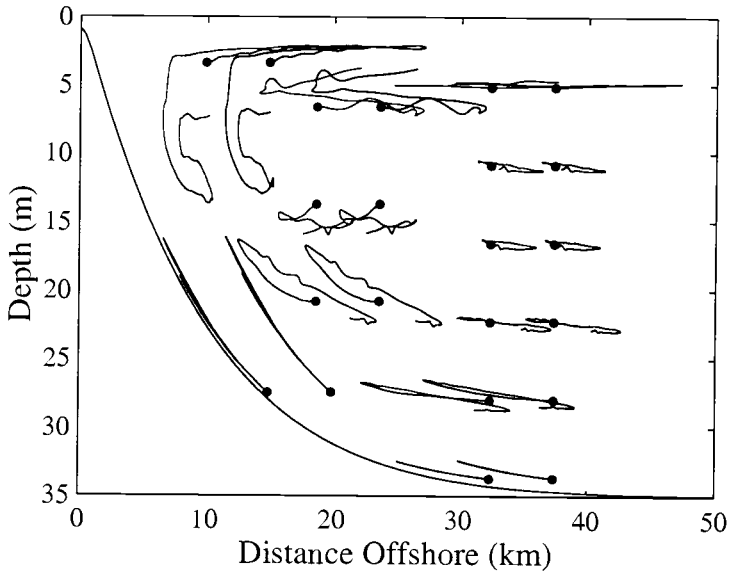

Figure 23. Lagrangian parcel paths during one period beginning at t_i=9.25T (red). The paths during a second period beginning at t_i=10.25T are shown in blue with a 5 km offset. The dots denote the initial locations of the parcels.

In addition to tracking individual water parcels, we utilize a second technique that gives Lagrangian trajectories for a continuous field of parcels. This approach involves the definition of three Lagrangian label fields that are advected by the model velocities. The Lagrangian labels, $X(x,z,t)$, $Y(x,y,z,t)$, and $Z(x,z,t)$, satisfy the following equations:

$$\frac{DX}{Dt} = 0, \qquad \frac{DY}{Dt} = 0, \qquad \frac{DZ}{Dt} = 0, \tag{17}$$

where $\frac{D}{Dt} = \frac{\partial}{\partial t} + u\frac{\partial}{\partial x} + v\frac{\partial}{\partial y} + w\frac{\partial}{\partial z}$. The initial conditions are

$$X(x,z,t=0) = x, \quad Y(x,y,z,t=0) = y, \quad Z(x,z,t=0) = z. \tag{18}$$

With the two-dimensional approximation for the Eulerian flow we obtain

$$\frac{D}{Dt}\frac{\partial Y}{\partial y} = 0. \tag{19}$$

Thus, we can write

$$Y(x,y,z,t) = y + Y'(x,z,t), \tag{20}$$

and we can determine Y by solving for Y', where

$$\frac{DY'}{Dt} + v = 0, \tag{21}$$

with

$$Y'(x,z,t=0) = 0. \tag{22}$$

The labels X, Y and Z are calculated as fields on the model grid with the higher-order accurate advection scheme of Smolarkiewicz (1983) using three iterations of the corrective step. We note that the evolution of the Lagrangian label fields is completely determined by advection with the model-resolved velocity fields. Consequently, the behavior of the labels will differ from that of passive tracer fields that are diffused by the effects of small scale turbulence. This difference is shown explicitly by analysis of results from related solutions in KC2003.

3.4 Dynamical Analysis

3.4.1. Mean Velocities

The one-period means of the Eulerian, Lagrangian and Stokes velocities (Figure 24) show a response to both upwelling and downwelling forcing. The mean

Stokes velocity is defined here as the difference between the mean Lagrangian and Eulerian velocities:

$$\bar{\mathbf{u}}_S(x(t_i), z(t_i)) = \bar{\mathbf{u}}_L(x(t_i), z(t_i)) - \bar{\mathbf{u}}_E(x(t_i), z(t_i)), \tag{23}$$

where

$$\bar{\mathbf{u}}_E(x(t_i), z(t_i)) = \frac{1}{T}\int_{t_i}^{t_f} \mathbf{u}_E(x(t_i), z(t_i), t)\, dt, \tag{24}$$

$$\bar{u}_L(x(t_i), z(t_i)) = \frac{x(t_f) - x(t_i)}{T}, \qquad \bar{w}_L(x(t_i), z(t_i)) = \frac{z(t_f) - z(t_i)}{T},$$

$$\bar{v}_L(x(t_i), z(t_i), y(t_i)) = \frac{y(t_f)}{T}. \tag{25}$$

and $T = t_f - t_i$.

The mean Eulerian across-shelf velocity u shows onshore flow of 2 cm s^{-1} in the bottom layer and offshore flow at about 5-15 m depth from 0-20 km offshore. A classical steady upwelling response would exhibit offshore flow in the surface layer and onshore return flow in the bottom layer (as in Figure 3 at t=9.25T). The response here resembles such an upwelling circulation, but the location of the maximum offshore velocity is shifted from the surface layer downward due to the downwelling phase of the circulation. There also exists a region of onshore flow in the top 5 m and a region of offshore flow between 20-25 m depth from 10-20 km offshore. The pattern of mean onshore surface u and offshore u below arises because the surface layer during upwelling is thicker than that during downwelling from 10-20 km offshore. The dynamics of this response are described in Section 3.5.1.

The Lagrangian across-shelf velocity computed from the parcel tracking technique shows a similar pattern. The Stokes velocity quantifies the differences

between the Eulerian and Lagrangian mean velocities. The most significant difference is located near the bottom from the coast to 8 km offshore. The mean Lagrangian u is offshore in this region, whereas the Eulerian u is onshore, leading to large positive Stokes drift values. Parcels that are initialized in this region have a net offshore displacement, despite the mean onshore Eulerian velocity, because they are advected vertically up the shelf and then offshore over a forcing period.

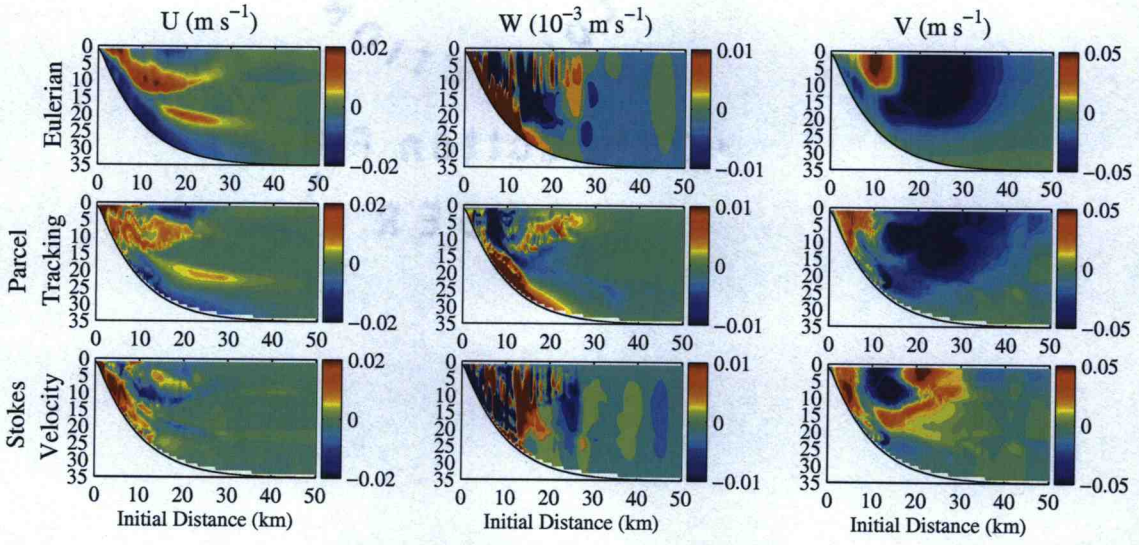

Figure 24. Mean Eulerian (Eq. 24) (top), Lagrangian (Eq. 25) (middle), and Stokes (Eq. 23) (bottom) velocities computed over one period beginning at t_i=9.25T. u is across-shelf, w is vertical, and v is alongshelf.

The mean Eulerian alongshelf velocity v shows a northward coastal upwelling jet of 5 cm s^{-1} and a region of similar magnitude southward velocities from 20–40 km offshore and extending to 20 m depth. This is evidence again of the impact of both upwelling- and downwelling-favorable wind forcing with a narrow northward coastal jet during upwelling and a broader southward current during downwelling. The Lagrangian alongshelf velocity pattern is similar, although the northward coastal jet

is distorted in x and z and located closer to the coast. The Stokes velocity reflects this difference, as well as the larger southward Eulerian v values offshore of 15 km. The Eulerian vertical velocity w is rather noisy, but shows upward velocities near the coast due to upwelling, and downward velocities just offshore due to downwelling. The Lagrangian vertical velocity shows a similar pattern from the coast to 12 km offshore, without the small-scale features seen in the Eulerian field. The vertical Stokes velocity reflects the consistently larger Eulerian w values and the patch of negative Eulerian w from 12–20 km that is not found in the mean Lagrangian w.

3.4.2 Nonlinear Advection

The dominant balance in the one-period mean of the alongshelf momentum balance for a cycle beginning at t_i=9.25T is between the Coriolis and vertical diffusion terms (Figure 25). Within the first 12 km of the coast, the nonlinear advection term also plays an important role. The nonlinear term is also important in the explanation of dynamical differences between the upwelling and downwelling responses (KC2003). We investigate these differences further by looking at mean fields computed over each half period with upwelling and downwelling forcing beginning at t_i=9T (Figure 26). The streamfunction ψ is defined as $\psi_\sigma = uD$, $\psi_x = -\omega$. The nonlinear advection term may be written as $\mathbf{u} \cdot \nabla v = uv_x + wv_z$, which corresponds to a spatial derivative of v in a direction tangent to the streamlines ψ=constant. The relative intensity of the across-shelf circulation can be estimated from the spacing of the streamlines. Thus the magnitude of the term $\mathbf{u} \cdot \nabla v$ can be qualitatively assessed from the streamline spacing and the gradient of v along streamlines.

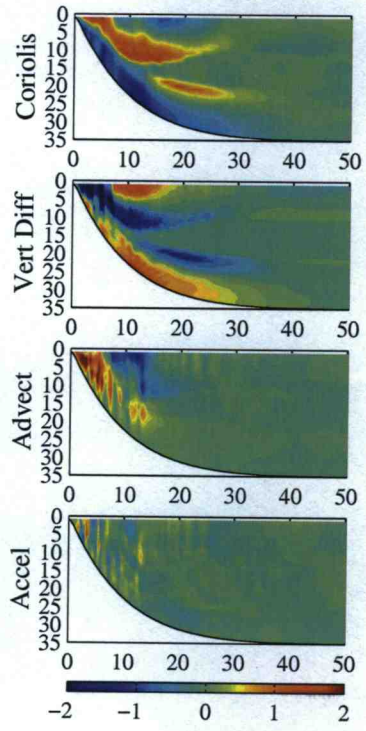

Figure 25. Mean alongshelf momentum balance terms over one period beginning at t_i=9.25T. The signs of the terms correspond to all terms on the left-hand side of the equation. The units for each term are 10^{-6} m s^{-2}.

The streamlines show very similar across-shelf circulation values during upwelling and downwelling, with opposite signs to indicate the reversed sense of circulation between upwelling and downwelling. The alongshelf velocity during upwelling shows a northward coastal jet from 0-15 km offshore and a region of southward velocities just offshore. During downwelling, however, the strongest alongshelf velocity values extend to 35 km offshore, with a region of much weaker velocity from 5-10 km offshore. This structure exhibits weaker across-shelf and vertical gradients in v, which lead to smaller magnitude values for the nonlinear term during downwelling. The nonlinear term during downwelling is only significantly

different from zero in a few small bands of about 1 km width (Figure 26, bottom right panel). During upwelling, the nonlinear term is large and positive from 2-6 km offshore, and large and negative from 10-20 km offshore. The structure of the nonlinear advection term during upwelling also closely resembles that of the mean field over a period (Figure 25). Therefore, the nonlinear advection term makes a significant contribution to the alongshelf momentum balance during the upwelling phase of the forcing period, but a relatively small contribution during the downwelling phase.

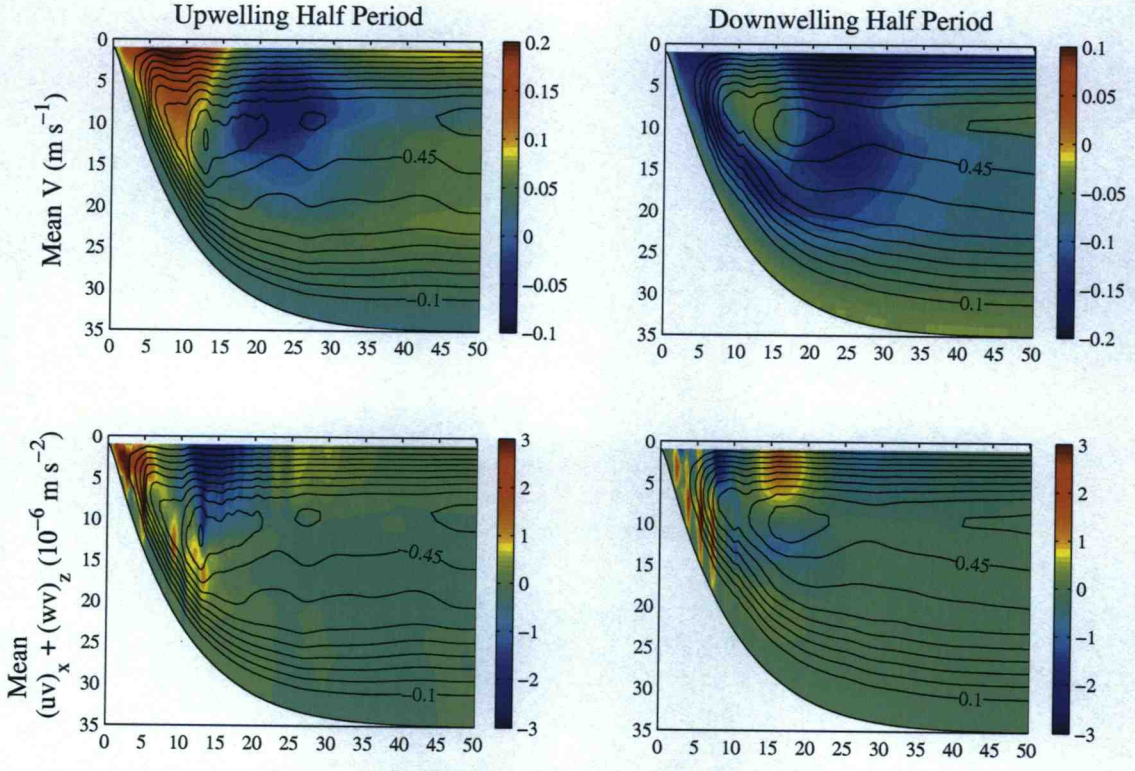

Figure 26. Mean of alongshelf velocity (top) and the nonlinear advection term from the alongshelf momentum balance (bottom) over the half period with upwelling forcing, t=9 T–9.5 T (left), and downwelling forcing, t=9.5 T–10 T (right). The streamlines are also plotted as black contours.

3.5 Lagrangian Parcel Paths

3.5.1. Lagrangian Label Field Results

The time evolution of the Lagrangian label fields X, Y, and Z introduced in Section 3.3.3 provide an effective way to examine the across-shelf, alongshelf, and vertical displacements of water parcels on the shelf. We show the evolution of these fields throughout a forcing period beginning at t_i=9.25T by plotting their distributions at t=9.5T, 9.75T, 10T, and 10.25T (Figure 27). At 9.5T, the X label shows surface parcels have moved about 10 km offshore, while bottom parcels have moved about 5 km onshore as the response in the bottom layer is slower than that in the surface. Parcels near the surface move onshore close to their initial locations at 9.75T while most of the bottom layer parcels have not moved significantly since 9.5T. At 10T, parcels in the surface layer are displaced 10 km onshore and parcels in the bottom layer have retreated offshore toward their initial across-shelf location. After a full period, surface parcels are advected offshore again near their initial positions. The final distribution of X shows a feature of offshore displacement at 20 m depth from 15–35 km offshore and several interlacing features inshore of 20 km. The former is due to the thicker bottom boundary layer that is present during downwelling than during upwelling, ascribed by Lentz and Trowbridge (1991) to the upslope (upwelling) or downslope (downwelling) transport of buoyancy along the bottom. During upwelling, the upslope transport of denser water under lighter water enhances the stratification and inhibits growth of the bottom boundary layer. In contrast, the downslope transport of lighter water under heavier water during downwelling tends to enhance mixing and thus, leads to growth of the bottom boundary layer. During downwelling, parcels are displaced offshore in a 10–15 m

thick bottom layer. However, during upwelling, the bottom layer is only 5–10 m thick, therefore parcels in this thinner bottom boundary layer are displaced onshore and parcels just above it are displaced offshore relative to their initial positions after one period.

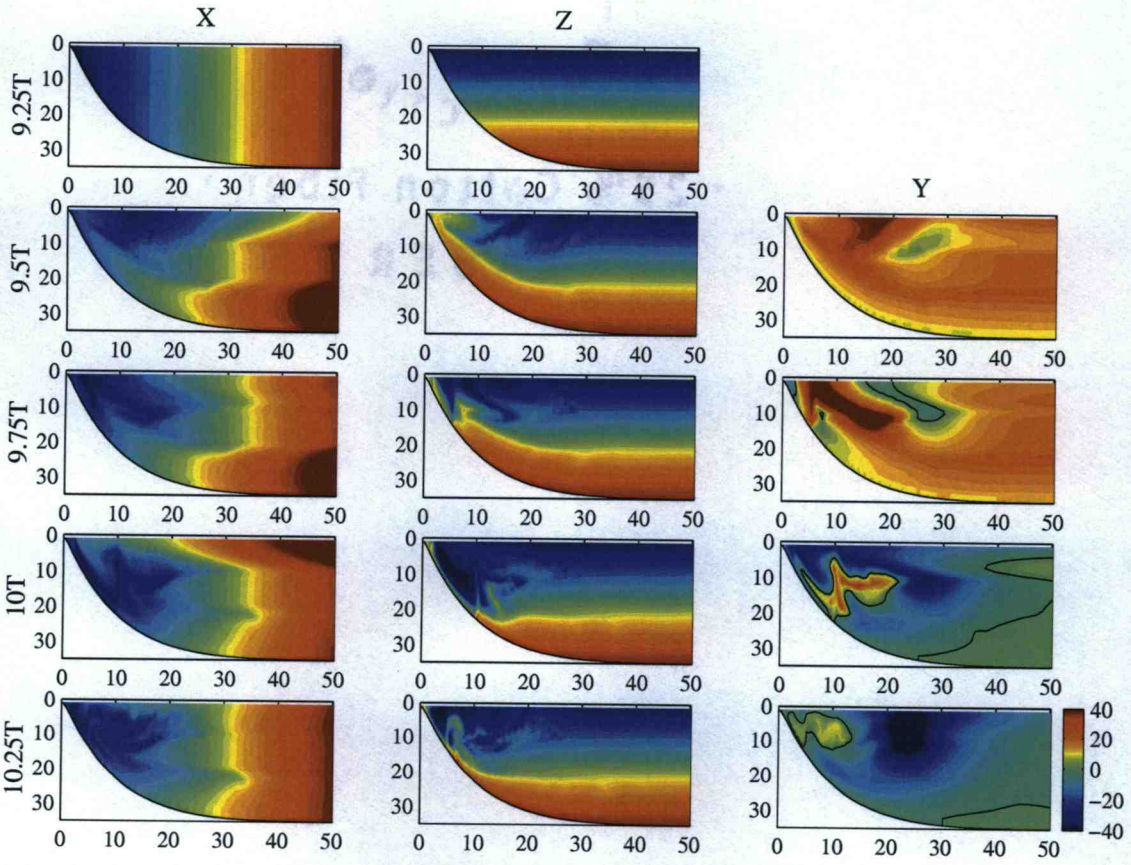

Figure 27. Contours of Lagrangian label fields every quarter period during one period beginning at t_i=9.25T. The Y label has units of km and the black line marks the 0 contour for Y.

A similar physical argument applied to the surface layer supports the pattern of u in Figure 21 and the feature of offshore displacement of X just below the surface from 10–20 km offshore in Figure 27. In this case, upwelling transports heavier water to the surface, enhancing mixing and producing a thicker surface boundary layer. Downwelling transports lighter water onshore which inhibits mixing and leads to the net onshore displacement of green X labels at the surface from 10–20 km offshore (Figure 27).

The evolution of Z in Figure 27 shows complicated structures that develop during both upwelling and downwelling. At 9.75T, a thin layer of parcels initialized at mid-depth has been advected upward toward the coast due to upwelling. After downwelling begins, the 10T distribution shows part of this thin layer of Z parcels remains trapped at the coast because the downwelling response is weak inshore of about 5 km.

The Y label field shows alongshelf advection of up to 40 km to the north (red) and south (blue). The region of northward parcel advection in the coastal upwelling jet moves onshore and increases in magnitude from 9.5T–9.75T. After a quarter-period of downwelling forcing (10T), however, the region of northward displacements has decreased significantly in size and magnitude and southward displacements are found offshore near the surface. The quarter-period of upwelling forcing from 10T–10.25T does not significantly increase the northward displacements in this region, as might be expected, but only moves the jet up the shelf. Southward displacements exist over a region of relatively large offshore extent from x=15–35 km. The Y response reflects the lag of alongshelf parcel advection after the alongshelf wind changes direction discussed in Section 3.3.2 (Figure 22).

Net displacements of water parcels over many forcing periods, or several upwelling and downwelling events, can also be described by the evolution of the Lagrangian label fields X, Y, and Z (Figure 28). After two periods, the distributions of X, Y, and Z look very similar to those after one period in Figure 27. The feature at 20 m depth in X that was described due to the difference in bottom boundary layer thickness during upwelling and downwelling becomes more pronounced with each additional forcing period. It also appears in the Z field after 4 periods (t=13.25T). The region of trapped parcels near the coast, as shown by Z, grows in time and the initial position of the trapped parcels becomes deeper (colors near the coast change from yellow to red). Net onshore displacement of X occurs at about 5-10 m depth offshore of 30 km. Between these features at mid-depth offshore of 30 km, there is very little horizontal or vertical motion. Onshore of 30 km, however, parcel displacements are complicated and there is significant across-shelf and vertical motion.

The region of southward alongshelf displacements (Y) increases in both size and magnitude as the parcels are advected farther south over a broader region of the shelf with each forcing period. In contrast, the inshore region of northward displacements shrinks in size and decreases in magnitude. This result is robust for simulations beginning at any point in the forcing period (8.5T, 8.75T, 9T, or 9.25T). Thus, after several periods, parcels at almost all depths from 0–50 km will be displaced south of their initial position, independent of the initial forcing phase. Evidently, the reason for this is that parcels do not remain in the region of the northward upwelling jet, where they would be advected farther northward, but instead move offshore into the broad region of southward velocities (see the mean Lagrangian u and v in Figure 24).

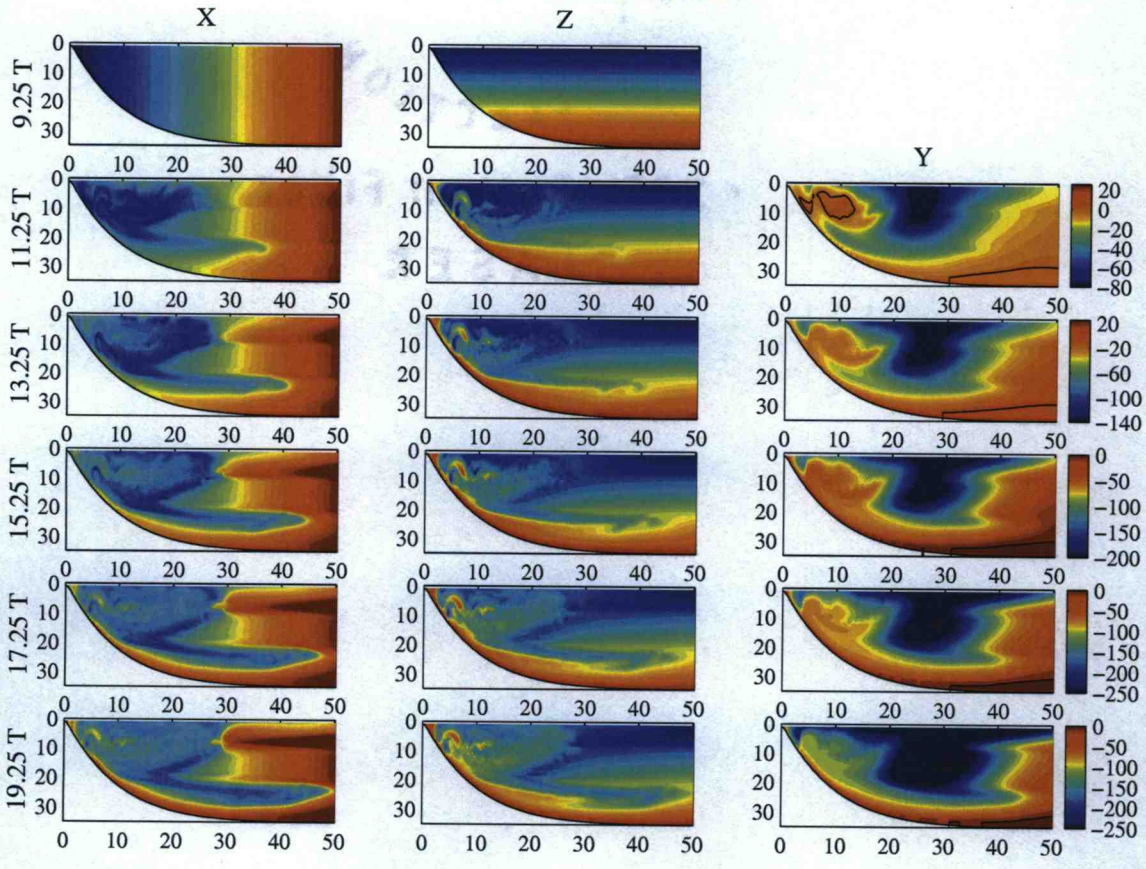

Figure 28. Contours of Lagrangian label fields every two periods during a ten period simulation beginning at t_i=9.25T. The Y label has units of km and the black line marks the 0 contour for Y.

3.5.2 Fluid Parcel Tracking Results

We also investigate parcel displacements over a forcing period using the parcel tracking method introduced in Section 3.3.3 for a simulation with t_i=9.25T and parcels initialized at every grid point on the model domain (Figure 29, top panel). Some regions show net displacements over a period that agree well with the label fields (Figure 27), while other regions are more complicated. Parcels in the bottom 5 m of the shelf move onshore with displacement values that increase as the initial

position of the parcel nears the coast. Offshore displacement, due to the thicker bottom boundary layer during downwelling, of parcels initially between 15-45 km is apparent above the bottom layer. At mid-depth and offshore of 20 km, parcels are shown to move slightly downward over a forcing period. In the surface layer offshore of 30 km, a cell structure is seen with parcels moving offshore above 5 m and onshore from 5-10 m depth. The parcel motion near the coast is complicated with parcel displacements that cross one another and vary in length and direction. It is unclear whether all of this complexity is due to the true motion resolved by the model, or if small errors in the parcel tracking calculation make a contribution. It was determined through testing of the technique that the results are somewhat sensitive to the conditions imposed at the coastal boundary. However, the results of the Lagrangian label analysis also show this region produces significant parcel displacements and complex paths over one period (Figure 27) or ten periods (Figure 28). Thus, we are confident in the general conclusion of complex parcel paths existing in this region, although care must be taken in determining individual parcel trajectories.

3.5.2.1 Parcel Displacement Maps: Due to the near periodicity of the response, we can use a mapping technique to calculate the parcel displacements over many periods without actually tracking them in the model simulation. The map is created from the one period model parcel displacements (Figure 29, top panel). Using a bilinear interpolation, the net displacement of each parcel in x and z may then be iterated forward for as many periods as desired. This mapping technique can thus provide a description of parcel displacements over many periods at very little computational cost. The map is an extremely useful tool that helps determine the qualitative Lagrangian behavior and gives a clear picture of parcel

displacement trends. Implementing the one-period displacement map technique, we effectively approximate the Eulerian flow as periodic. The qualitative accuracy of this approximation is supported by Figures 20 and 23, as well as the bottom panels of Figure 29, which show that the iterated map reproduces the features of the ten-period model parcel displacements reasonably well. The model displacements tend to be larger than those produced from the iterated map in some locations. Again, the complicated region near the coast exhibits the largest quantitative differences because the model displacements are not entirely reproducible from one period to the next in this area (Figure 23), hence the iterated-map trajectories diverge slowly from the model trajectories.

We performed simulations with varying horizontal and vertical resolution to determine the sensitivity of the Eulerian and Lagrangian results on model resolution. For t_i=9.25T, we computed model Eulerian fields, Lagrangian labels, and parcel trajectories over one period with Δx=125 m and 45 σ levels to compare with the basic case resolution of Δx=250 m and 30 σ levels. Parcels were located at each grid point in both simulations. The results of the mean Eulerian fields, Lagrangian label evolution, and 10 period parcel maps were quantitatively similar in both cases.

The Lagrangian results depend on the simulation start time because this determines the phase of the model Eulerian velocity field. We investigate the dependence of the 100-period Lagrangian maps on the simulation start time by plotting selected parcel positions after each period for t_i=8.5T, t_i=8.75T, t_i=9T, and t_i=9.25T (Figure 30). The same structures are seen in all of these maps, however they are located in different across-shelf and, in some cases, vertical, locations. The maps show regions with well-defined periodic motion and regions with a more

complex response to periodic forcing. A rotating cell feature (offshore of 30 km at t_i=8.75T) and the slow downward motion at mid-depth are apparent. The previously described feature with offshore displacement from 20-25 m depth and onshore displacement below is seen. Inshore of 30 km, the parcel displacements do not exhibit any regular patterns. Parcels that upwell to the near surface close to the coast are typically displaced offshore within the complex region. A clear boundary between this region and the offshore surface cell is apparent (e.g., at 30 km offshore at t_i=8.75T) in which parcels above 10 m depth move upward and offshore into the cell.

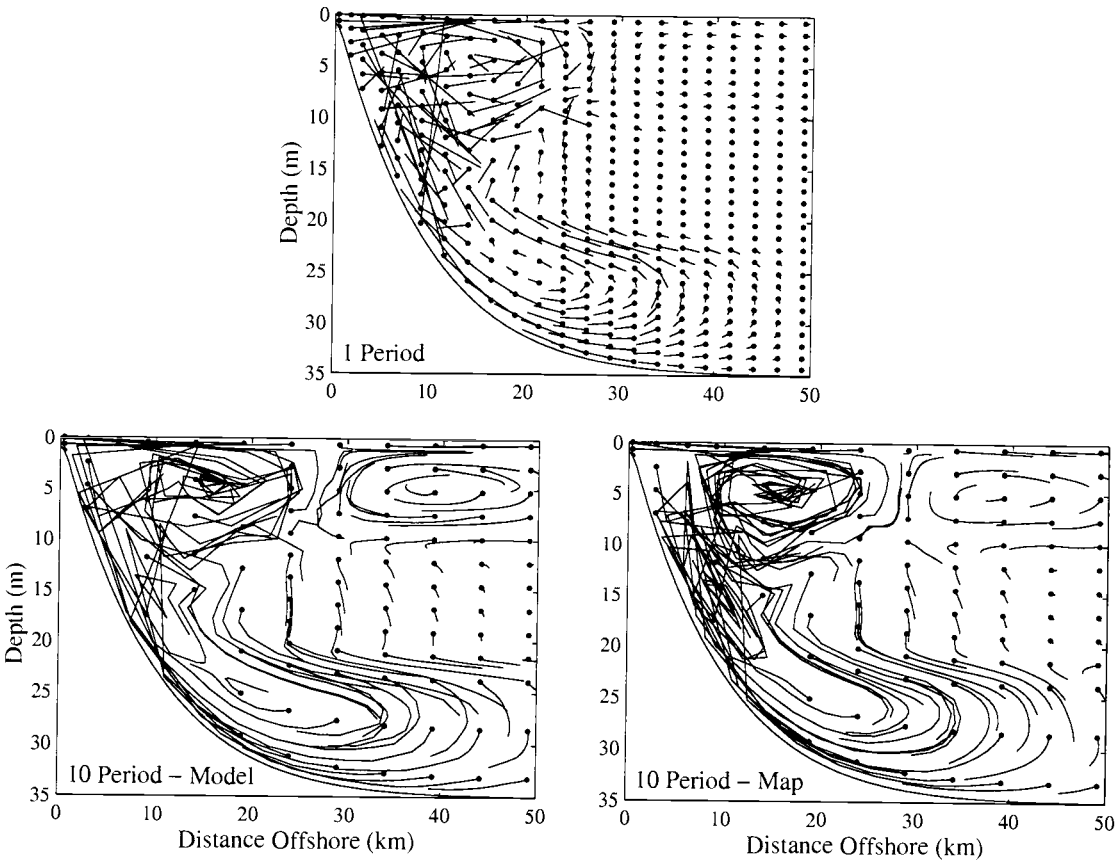

Figure 29. Lagrangian parcel displacements over one period (top) and over ten periods computed from the model (bottom left) and mapping technique (bottom right) for a simulation beginning at t_i=9.25T. The dots denote the initial locations of the parcels.

The evolution of parcels in the cell structure and other parcels on the shelf is explained by the upwelling and downwelling dynamics over a forcing period and can be determined by studying the sequential maps (Figure 30). The surface cell feature is displaced offshore of 30 km for t_i=8.5T and onshore for t_i=9T. For t_i=9.25T, the location is similar to that for t_i=8.75T. The orientation of the boundary between this structure and the complex region inshore also varies. Parcels offshore of 30 km in the top 5 m are displaced onshore about 20 km during the half cycle t=8.5T–9T, and parcels from 5-10 m are displaced about 10 km onshore. From 10-20 m depth, parcels are displaced 5 km offshore and below this, in the bottom boundary layer region, parcels are displaced about 10 km offshore. Near the coast the across-shelf motion is not as clear and vertical motion is significant.

To quantify the motion of the cell feature over a forcing period, consider the trajectory of a single parcel initialized at t_i=8.5T at x=48.875 km, z=-4.0783 m (the approximate center of the offshore surface cell) (Figure 31a). Subject to downwelling forcing initially, the parcel moves 9 km onshore in the first quarter period and 11 km onshore in the second quarter period. After upwelling winds begin at t=9T, the parcel moves offshore 8 km during the third quarter period and another 12 km in the final quarter period. Total vertical displacement over a period is only about 0.2 m. The final position of the parcel is almost exactly the same as its initial position. Thus the net across-shelf displacement of a parcel near the cell center over a period is very small even though it is advected 20 km across the shelf during each phase of the forcing period. Figure 31a shows movement of the cell center and clearly illustrates why the maps constructed at different phases of the forcing cycle have different structures.

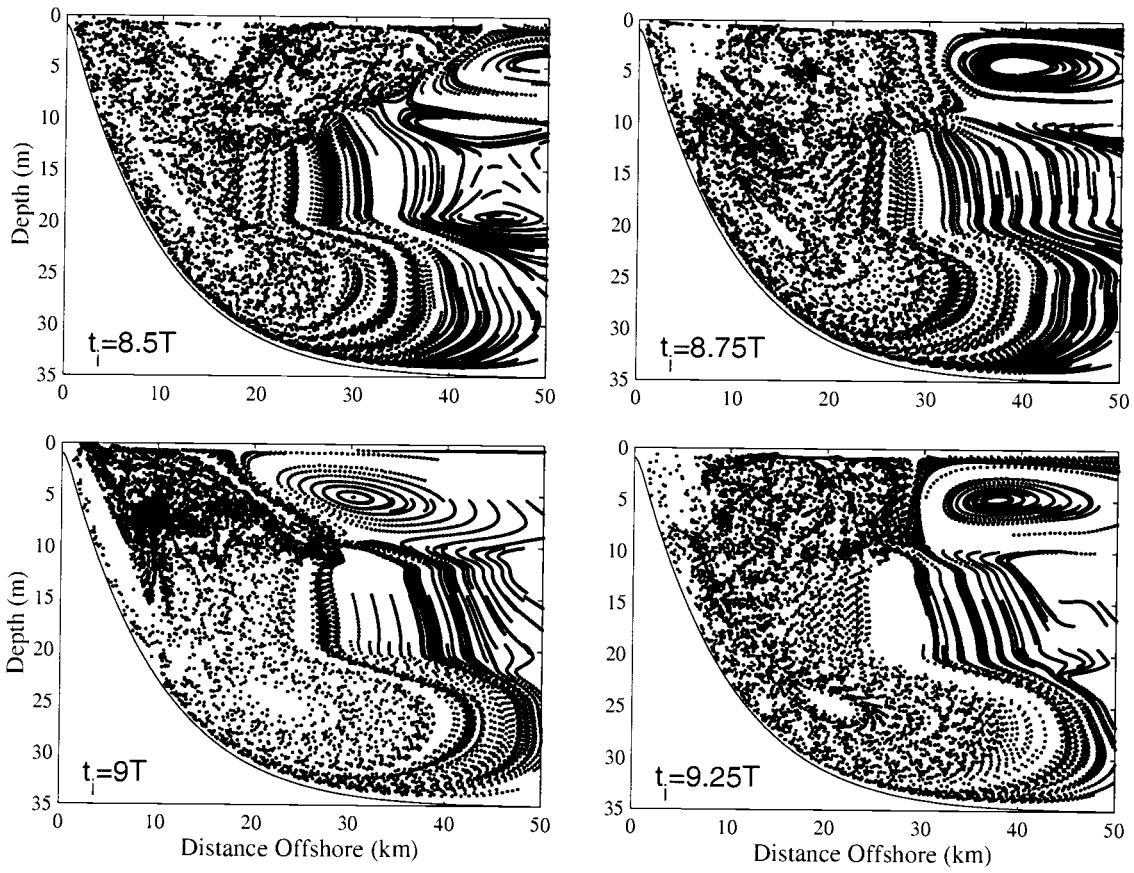

Figure 30. Lagrangian parcel positions after each period predicted by mapping technique over 100 periods for simulations beginning at t_i=8.5T, t_i=8.75T, t_i=9T, and t_i=9.25T.

Consider a second parcel initialized at t_i=8.5T at x=37.375 km, z=-4.0448 m (Figure 31b). The parcel travels about 20 km onshore during downwelling and 20 km offshore during upwelling. The position after one period, at t=9.5T, is about 1 m above the initial position and the position after two periods at t=10.5T is 1 m above that at t=9.5T. The parcel has a net offshore displacement of 1 km during each of these periods. In contrast, the net displacement of the parcel is 1 km onshore over the period from t=9T–10T. Thus, the direction of displacement across the shelf differs for the upwelling half-period (onshore displacement) and the downwelling

half-period (offshore displacement) for parcels in the region just onshore of the cell feature, and the net displacement over a full period depends on the phase of the forcing at initialization due to the net vertical motion and the vertical shear of the time-dependent Eulerian flow.

3.5.2.2 Lyapunov Exponents: Lyapunov exponents quantify exponential rates of divergence or convergence of the trajectories of initially neighboring particles in a flow field. Thus, they provide a measure of the chaos present in a system. The Lagrangian results presented in Sections 3.5.1 and 3.5.2 suggest that the parcel trajectories in the complicated region near the coast are chaotic. We examine this possibility and quantify the degree of chaos present in the wind-forced flows studied here by calculating the largest Lyapunov exponent of the parcel displacement maps.

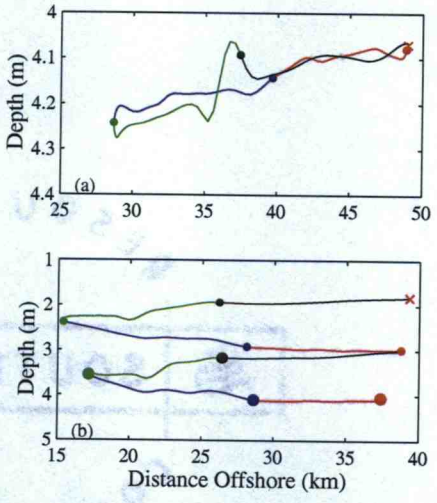

Figure 31. Lagrangian parcel positions (a) during one period for a parcel initialized at t_i=8.5T at x=48.875 km, z=-4.0783 m and (b) during two periods for a parcel initialized at t_i=8.5T at x=37.375 km, z=-4.0448 m. The red dot is the initial position, the blue dot is the position at t=8.75T, green dot at t=9T, and black dot at t=9.25T. The colors repeat for the second period positions in (b) with smaller dots. The final parcel position is given by the red $\times$.

We estimate the largest Lyapunov exponent λ for the two-dimensional periodic map (see e.g. Benettin et al., 1976; Lichtenberg and Lieberman, 1983) from the truncated approximation with finite M as:

$$\lambda = \frac{1}{M\Delta t} \sum_{i=1}^{M} ln \frac{L_i}{L'_{i-1}}, \tag{26}$$

where $L_i = (\Delta x_i^2 + \Delta z_i^2)^{1/2}$ is the distance after the i^{th} cycle between two parcels initially separated by Δx_0 at $t = t_0$ and $L'_i = (\Delta x_i'^2 + \Delta z_i'^2)^{1/2}$ where $\Delta x'_i$, $\Delta z'_i$ are rescaled values of the estimated separations Δx_i, Δz_i given, if $L_i > \Delta x_0$, by $\Delta x'_i = \frac{\Delta x_i}{Li} \Delta x_0$, $\Delta z'_i = \frac{\Delta z_i}{Li} \Delta x_0$ so that $L'_i = L_0 = \Delta x_0$. The calculation of L_i is made after each iterated period for every parcel initialized on the map grid at (x_0, z_0) and a neighboring parcel initialized at $(x_0 + \Delta x_0, z_0)$. If $L_i > \Delta x_0$, the distance between parcels is rescaled such that the neighboring parcel is re-positioned from $(x_i + \Delta x_i, z_i + \Delta z_i)$ to $(x_i + \Delta x'_i, z_i + \Delta z'_i)$ to keep the calculation near linear as parcel separations increase. If $L_i \leq \Delta x_0$, then we do not rescale so that $\Delta x'_i = \Delta x_i$, $\Delta z'_i = \Delta z_i$, and $L'_i = L_i$. The map is then used to determine the positions of the grid of neighboring parcels after any necessary rescaling has been done. The calculation was tested by varying the initial separation distance Δx_0 by $\Delta x_0 = \Delta x_{grid}/n$ (where Δx_{grid}=250 m, the grid resolution of the model and the map), and n=1, 2, 4, 8, 16, 32, 64. We also performed tests with an initial separation in the vertical direction of Δz_0 such that the grid of neighboring parcels was initialized at $(x_0, z_0 + \Delta z_0)$. The largest Lyapunov exponent was estimated for both positive and negative values of $\Delta x_0, \Delta z_0$ and the results were qualitatively similar in all cases. As Δx_0 decreased, the small differences between results for the positive and negative initial separations also decreased.

Estimates for the largest Lyapunov exponent λ are calculated for M=100

forcing periods with $\Delta x_0 = \Delta x_{grid}/64$ (Figure 32). Plots of λ for selected parcels versus $t^{-1} = (i\Delta t)^{-1}$ indicate that the choice of M=100 gives reasonable, but not fully convergent, approximations for the values of λ. Values of λ are largest in the region with complex parcel displacements near the coast and in the bottom 10 m. In these locations, the magnitudes of λ are approximately 6–8. Offshore of 30–40 km from the surface to 25 m depth, values decrease to near zero, indicating regular behavior. Negative values in this region, which presumably would asymptote to zero, are generally small, e.g. the minimum value is -0.75. The boundary at 30 km between large, positive λ in the top 10 m and small λ offshore divides the region of irregular and complicated parcel paths from the regular motion found in the surface cell feature. The location of this boundary is a robust result for any sufficiently large number of periods M. The small λ values below the surface cell feature correspond to the mid-depth region of slow downward parcel motion.

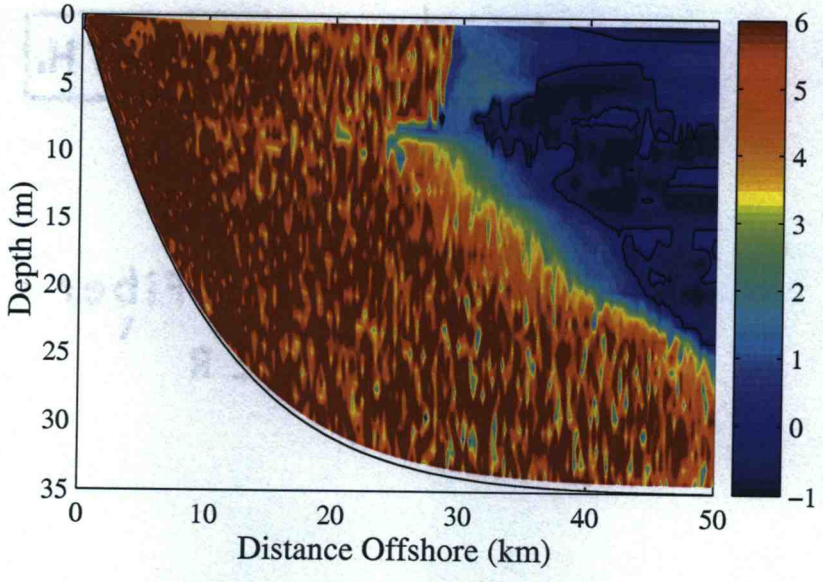

Figure 32. Largest Lyapunov exponent λ computed from the mapping technique after 100 forcing periods beginning at t_i=9.25T. The black line denotes the 0 contour.

3.6 Summary

The Eulerian and Lagrangian dynamics of a wind-forced continental shelf have been studied using a numerical model forced by periodic winds. The mean Eulerian velocities show features from both the upwelling and downwelling phases of the period. Near the surface, there is offshore flow from the coast to 30 km due to upwelling and onshore flow just above due to downwelling. In the bottom layer, onshore flow due to upwelling is in the bottom 5 m, and just above is a region of offshore flow due to downwelling, a result of the thicker bottom boundary layer during downwelling. In the alongshelf momentum balance, nonlinear advection of momentum is stronger during the upwelling phase. This result is linked to the weaker across-shelf and vertical gradients in the alongshelf velocity during downwelling.

Lagrangian motion was analyzed using Lagrangian label fields and a parcel tracking technique. The labels show significant across-shelf, alongshelf, and vertical advection over a period. After several forcing periods, the bottom layer response becomes much more pronounced while the surface layer response weakens. Near the coast, a region of large x and z displacements shows complex patterns in the label fields with variability in parcel trajectories from one period to the next. Net southward displacement increases and net northward displacement decreases in time, leading to the result that all the parcels on the shelf are displaced to the south after many periods. Similar information can be obtained by tracking individual parcels in the traditional manner.

Results have also been obtained by iterating the one-period displacement map for many periods. The map is useful in providing a qualitative assessment of the Lagrangian motion of fluid parcels over many periods. The perspective on parcel

motion over one period gained from the analysis of these iterated maps is valuable as well. By following the progression of maps initialized at different forcing phases, the displacement of parcels in different regions of the shelf can be identified. The rotating surface cell offshore of 30 km appears especially clearly in this analysis. The map also makes possible the calculation of approximate values for the largest Lyapunov exponent, which quantifies to some extent the chaos present in the region of complicated parcel paths near the coast.

Except near the center of the offshore surface cell, parcels generally do not return to their initial location after a period, hence a Stokes drift exists and is maximum in the complex region near the coast. Parcel displacement depends on the initial location and the initial forcing phase. Asymmetries between the upwelling and downwelling responses lead to significant net across-shelf displacements in the surface and bottom layers. The complex motion of Lagrangian parcels in three dimensions leads to interesting results that are not obviously suggested by the Eulerian fields. One clear example is the robust southward alongshelf displacement of all parcels after several periods.

3.7 Acknowledgments

This research was supported by the Office of Naval Research (ONR) Coastal Dynamics Program through grant N00014-02-1-0100. Additional support was provided for R.M.S. by the ONR Ocean Modeling and Prediction Program through ONR grant N00014-98-1-0813 and by the National Science Foundation through NSF grant OCE-9907854.

3.8 References

Austin, J.A. and S.J. Lentz, 1999: The relationship between synoptic weather systems and meteorological forcing on the North Carolina inner shelf, *J. Geophys. Res.*, **104**, 18,159-18,185.

Benettin, G., L. Galgani, and J.M. Strelcyn, 1976: Kolmogorov entropy and numerical experiments, *Phys. Rev. A*, **14**, 2338-2345.

Blumberg, A.F. and G.L. Mellor, 1987: A Description of a Three-Dimensional Coastal Ocean Circulation Model, *Three-Dimensional Coastal Ocean Models*, Coastal and Estuarine Science Series, Vol. 4, N. Heaps Ed., Amer. Geophys. Union, 1-16.

Coulliette, C. and S. Wiggins, 2001: Intergyre transport in a wind-driven, quasigeostrophic double gyre: An application of lobe dynamics, *Nonlin. Proc. Geophys.*, **8**, 69-94.

Galperin, B., L.H. Kantha, S. Hassid, and A. Rosati, 1988: A quasi-equilibrium turbulent energy model for geophysical flows, *J. Atmos. Sci.*, **45**, 55-62.

Haller, G., 2002: Lagrangian coherent structures from approximate velocity data, *Physics of Fluids*,**14**,1851-1861.

Ide, K., D. Small, and S. Wiggins, 2002: Distinguished hyperbolic trajectories in time-dependent fluid flows: analytical and computational approach for velocity fields defined as data sets, *Nonl. Proc. Geophys.*, **9**,237-263.

Kirwan, A.D., M. Toner, and L. Kantha, 2003: Predictability, uncertainty, and hyperbolicity in the ocean, *Int. J. Engin. Sci.*, **41**, 249-258.

Kuebel Cervantes, B.T., J.S. Allen, and R.M. Samelson, 2003: A Modeling Study of Eulerian and Lagrangian Aspects of Shelf Circulation off Duck, North Carolina, *Journal of Physical Oceanography*, **33**, 2070-2092.

Lentz, S.J. and J.H. Trowbridge, 1991: The bottom boundary layer over the northern California shelf, *J. Phys. Oc.*, **21**, 1186-1201.

Lichtenberg, A.J. and M.A. Lieberman, 1983: *Regular and Stochastic Motion*, Springer-Verlag, New York, NY, 499 pp.

Loder, J.W., Y. Shen, and H. Ridderinkhof, 1997: Characterization of Three-Dimensional Lagrangian Circulation Associated with Tidal Rectification over a Submarine Bank, *J. Phys. Oc.*, **27**, 1729-1742.

Mellor, G.L. and T. Yamada, 1982: Development of a Turbulence Closure Model for Geophysical Fluid Problems, *Rev. Geophys. and Space Phys.*, **20**, 851-875.

Miller, P.D., C.K.R.T. Jones, A.M. Rogerson, L.J. Pratt, 1997: Quantifying transport in numerically generated velocity fields, *Physica D*, **110**, 105-122.

Poje, A.C. and G. Haller, 1999: Geometry of Cross-Stream Mixing in a Double-Gyre Ocean Model, *J. Phys. Oc.*, **29**, 1649-1665.

Poje, A.C., M. Toner, A.D. Kirwan, and C.K.R.T. Jones, 2002: Drifter Launch Strategies Based on Lagrangian Templates, *J. Phys. Oc.*, **32**, 1855-1869.

Ridderinkhof, H. and J.W. Loder, 1994: Lagrangian Characterization of Circulation over Submarine Banks with Application to the Outer Gulf of Maine, *J. Phys. Oc.*, **24**, 1184-1200.

Rom-Kedar, V., A. Leonard, and S. Wiggins, 1990: An analytical study of transport, mixing and chaos in an unsteady vortical flow, *J. Fluid Mech.*, **214**, 347-394.

Smolarkiewicz, P.K., 1983: A Simple Positive Definite Advection Scheme with Small Implicit Diffusion, *Mon. Wea. Rev.*, **111**, 479-486.

Weiss, J.B. and E. Knobloch, 1989: Mass transport and mixing by modulated traveling waves, *Phys. Rev. A*, **40**, 2579-2589.

4 Numerical model simulations of continental shelf flows off Northern California

Brandy T. Kuebel Cervantes and J. S. Allen

To be submitted to Deep-Sea Research Part II

The Boulevard, Langford Lane

Kidlington, Oxford OX5 1GB, U.K.

4.1 Abstract

The three-dimensional circulation on the continental shelf off northern California in the WEST (Wind Events and Shelf Transport) experiment region is studied using the primitive equation Regional Ocean Modeling System (ROMS). The simulations are performed with realistic topography and initial stratification in a limited-area domain with a high-resolution grid. Forcing consists of measured wind stress and heat flux values obtained during summer 2001. The general response shows a southward coastal upwelling jet of up to 1 m s^{-1} and a weakening or reversal of currents inshore of the jet when upwelling winds relax. Model results are compared to WEST moored velocity and temperature measurements at five locations, to CODAR surface current observations between Pt. Reyes and Bodega Bay, and to hydrographic measurements along shipboard survey lines. The model performs reasonably well, with the highest depth-averaged velocity correlation (0.81) at the inshore mooring (40 m water depth) and lowest correlation (0.68) at the mid-depth mooring (90 m depth). The model shows generally stronger velocities than those observed, especially at the inshore moorings, and a lack in complete reversal of southward velocities observed when upwelling winds relax. The comparison of surface velocities with CODAR measurements shows good agreement of the mean and the dominant mode of variability. The hydrography compares closely at the southern and northern edges of the survey region (correlation coefficients between 0.90-0.97), with weaker correlations at the three interior survey lines (correlation coefficients between 0.44-0.76). Mean model fields over the summer upwelling period show slight coastal jet separation off Pt. Arena and significant separation off Pt. Reyes. The cape regions also experience relatively strong bottom velocities and nonlinearity in

the surface flow. Across-shelf velocity sections examined along the shelf reveal a double jet structure that appears just north of Bodega Bay and shows the offshore jet strengthening to the south. We examine the dynamics during an upwelling and subsequent relaxation event in May 2001 in which the WEST measurements show evidence of a strong flow response. The alongshelf variability in the upwelling and relaxation response introduced by Pt. Reyes is evident. Analysis of term balances from both the three-dimensional and depth-averaged momentum equations helps to clarify the event dynamics in different regions over the shelf. A clear pattern in the nonlinear advection term is due to the spatial acceleration of the southward jet around the capes of Pt. Arena and Pt. Reyes during upwelling. Results from a three-dimensional Lagrangian analysis of water parcel displacement show the source of upwelled water near the coast south of Pt. Reyes is local, as compared to that north of Pt. Reyes, which has a signature of deeper water from farther north.

4.2 Introduction

As part of the Coastal Ocean Processes (CoOP) program, the Wind Events and Shelf Transport (WEST) project has the overall goal of understanding the role that wind-driven transport plays in biological productivity over the northern California shelf. Through the collection of physical and biological data, WEST investigators hope to answer the interdisciplinary question of how a productive ecosystem develops over a strongly wind-driven shelf. This issue is complex due to the opposing effects of wind-driven transport on productivity. Nutrient supply to the upper layer due to upwelling of cold, nutrient-rich water increases productivity, while vertical mixing and near-surface offshore transport of plankton during upwelling-favorable winds

lead to decreased productivity on the shelf. WEST investigators propose that plankton are retained near the surface on the shelf through both circulation processes and consumption by higher trophic levels, and they expect that field measurements and numerical model results will reveal the roles of these mechanisms.

The region of interest for WEST extends from just south of Pt. Reyes to about 50 km north of Bodega Bay (Figure 33). This is an area that has been studied previously by large observational programs, such as the Coastal Ocean Dynamics Experiment (CODE) (Beardsley and Lentz, 1987) and the Shelf Mixed Layer Experiment (SMILE) (Alessi et al., 1991), and results of those experiments have been used for guidance in design of the WEST field measurements. Moorings deployed at five locations from May 2001–2003 by the WEST project collected measurements of current velocity, temperature, conductivity, pressure, wind, chlorophyll fluorescence, and optical transmissivity (Dever et al., 2004). Additionally, surface heat flux paramenters were measured at the central D090 mooring and fluxes were calculated using the algorithms specified in Beardsley et al. (1998) (E. Dever, personal communication). Land-based coastal radar (CODAR) systems were in operation during May 2001–September 2003 to measure surface currents over the region from Pt. Reyes to Bodega Bay. Ship surveys were also conducted during three summer upwelling periods and two winter downwelling periods between June 2000 and November 2002. These surveys were comprised of both vertical profiles and underway tow-yo sampling of water properties and current velocity (Largier, 2004).

In this study, we model the circulation over the continental shelf and upper slope in the WEST region during May – June 2001. During this period, the winds are

generally upwelling favorable at the central D090 mooring with a mean wind stress magnitude of 0.074 N m^{-2} directed toward 120 T. The magnitude and direction of maximum standard deviation in wind stress are similar to the mean for this period, i.e. 0.052 N m^{-2} and 116 T. This wind stress forces an upwelling circulation that persists throughout the summer with the exception of intermittent 1-3 day periods during which the alongshelf winds relax or reverse. The modeled velocity and hydrographic fields are next compared quantitatively with the WEST data sets. Following the model-data comparisons, we discuss the time mean response, which is dominated over the shelf by an upwelling circulation, and then proceed to focus on the dynamics of a specific upwelling and subsequent relaxation wind event that occurs from May 17 – 23, 2001.

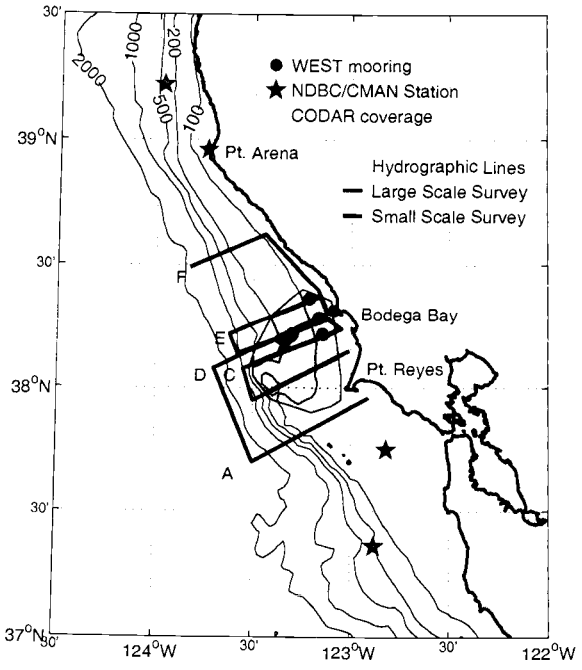

Figure 33. Observational layout for Wind Events and Shelf Transport (WEST) project.

The numerical model description and setup are presented in section 4.3. Comparisons of the model with the three datasets described above are provided in section 4.4. General characteristics of the flow field in response to summer upwelling-favorable winds are discussed in section 4.5. A detailed dynamical analysis of an upwelling and relaxation event is presented in section 4.6 and a summary is provided in section 4.7.

4.3 Model Formulation

The Regional Ocean Modeling System (ROMS) is a hydrostatic primitive equation model with terrain-following vertical coordinates. ROMS is based on the S-Coordinate Rutgers University Model (SCRUM) described by Song and Haidvogel (1994), but has been rewritten to include, for example, high-order advection schemes, accurate pressure-gradient algorithms, and several subgrid-scale parameterizations (Shchepetkin and McWilliams, 2004). We use the embedded Mellor-Yamada 2.5 level turbulence closure scheme (Mellor and Yamada, 1982) as modified in Galperin et al. (1988) and the third-order upstream bias advection scheme for momentum and tracers (Shchepetkin and McWilliams, 1998). The pressure-gradient scheme is a splines density Jacobian, one of three methods developed by Shchepetkin and McWilliams (2003) to minimize the errors associated with computing horizontal pressure gradients with terrain-following coordinates.

The model domain and bathymetry is shown in Figure 34. The model bathymetry is a spatially-filtered version of that obtained from the National Geophysical Data Center GEODAS dataset with 3-second resolution. It is smoothed such that the maximum local slope factor, defined as $|\delta h/h|$ (Mellor et al., 1994), is

no greater than 0.2. This value has been shown to limit the errors associated with the pressure gradient calculation (Barnier et al., 1998; Beckmann and Haidvogel, 1993).

Periodic boundary conditions are used on the northern and southern boundaries and the model bathymetry is adjusted to be equal at these boundaries. The alongshelf length of the domain is 400 km and the across-shelf length is approximately 135 km. The Cartesian (x,y) grid has a resolution of 1.7 km in the alongshelf y direction and between 0.8–1.8 km in the across-shelf x direction with the highest resolution near the coast. In the vertical, we use 40 s-levels with spacing such that there is higher resolution in the surface and bottom layers.

At the coastal boundary, the application of land masking gives a no flux condition on the normal velocity component and a no slip condition on the tangential velocity component. At the offshore boundary, we use a condition of zero normal depth-integrated velocity ($U = 0$) and free slip for the tangential depth-integrated velocity ($V_x = 0$). The free surface satisfies an implicit gravity wave radiation condition (GWI as described in Chapman, 1985), the depth-dependent velocities satisfy a radiation condition, and the tracers and turbulence quantities satisfy a no gradient condition ($T_x = S_x = q_x^2 = 0$). The initial temperature and salinity profiles in Figure 35 are horizontally uniform and are taken from the mean of the central D line CTD survey data. The temperature profile is very similar to that calculated as the mean of April 1981-82 values from the CODE experiment central line. However, the salinity profile from the WEST measurements is less stratified than that from the CODE measurements, which has a value of approximately 33.3 psu near the surface and increases to 33.9 psu at 140 m depth (Huyer, 1984).

The model simulation occurs over 57 days during April 25 – June 20, 2001. We regard the first ten days (April 25 – May 4), during which the WEST measurements are unavailable for model-data comparisons, as a spinup period. Therefore, we calculate time mean fields presented in section 4.5 over 47 days from May 5 – June 20, 2001. Figure 36 shows the wind stress and heat flux time series used to force the model, which are calculated from measurements at the central D090 mooring, then low-pass filtered and applied uniformly at each surface grid point. The alongshelf component τ_y^s has a mean value of -0.064 N m^{-2} and standard deviation of 0.047 N m^{-2}, and the across-shelf component τ_x^s has a mean value of 0.035 N m^{-2} and standard deviation of 0.029 N m^{-2}. The total heat flux has a mean value of 80 W m^{-2} and standard deviation of 56 W m^{-2}. The instruments at D090 were not fully operational prior to May 5, therefore we used a linear regression of the NDBC 13 buoy winds (located just offshore of the D130 mooring) and a linear increase in heat flux from near zero to the first measured value.

The assumption of no spatial variability in the wind field is not accurate, as has been previously shown by wind measurements in the CODE and WEST regions (Beardsley et al., 1987; Dorman and Winant, 1995). An advantage to forcing the numerical model with a spatially-uniform wind field is that we may isolate the topographically-dominated shelf circulation response to upwelling and relaxation in this initial study without the influence of spatially-variable wind forcing. Future modeling studies of this region are planned that will utilize wind stress fields obtained from a high-resolution regional mesoscale atmospheric model after these become available following evaluations with model/data comparisons (C. Dorman, personal communication). The response to spatially-uniform winds should, in any

case, provide a useful benchmark for future investigations that address the specific effects of spatially-variable winds.

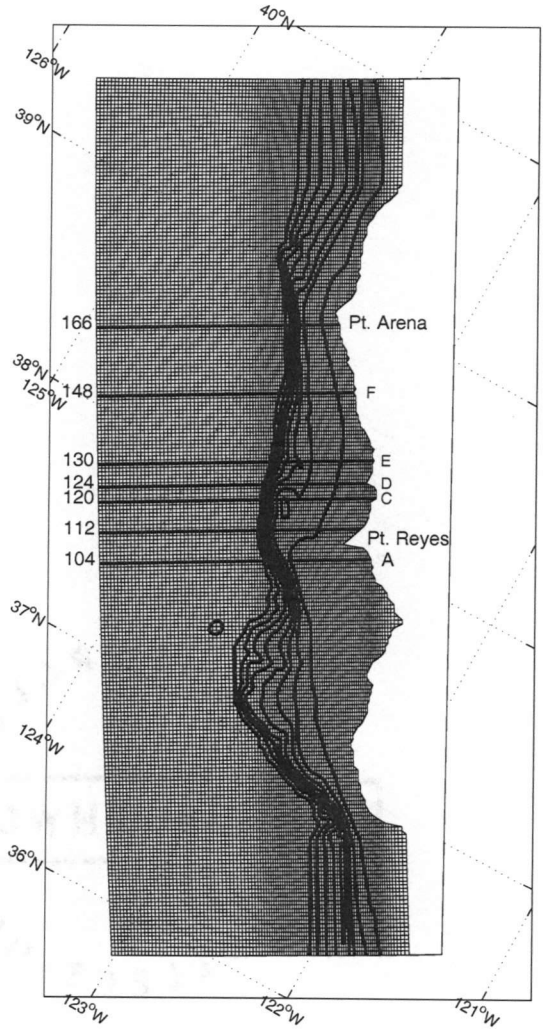

Figure 34. ROMS model domain with grid resolution and bathymetry contours. The grid's alongshelf axis is aligned along 330 T. The horizontal lines show the locations of across-shelf sections, numbered according to alongshelf grid number, that are discussed in section 4.6. Five of these lines correspond to WEST survey lines A-F as shown on the right side. Note that the distance from the offshore boundary to the coastal boundary is approximately 135 km at both ends of the model domain, although the distances appear slightly different due to the map projection. The isobaths shown include 100 m and 200 – 1400 m at intervals of 200 m. Cordell Bank is the topographic feature just south of the C line denoted by the closed 100-m isobath.

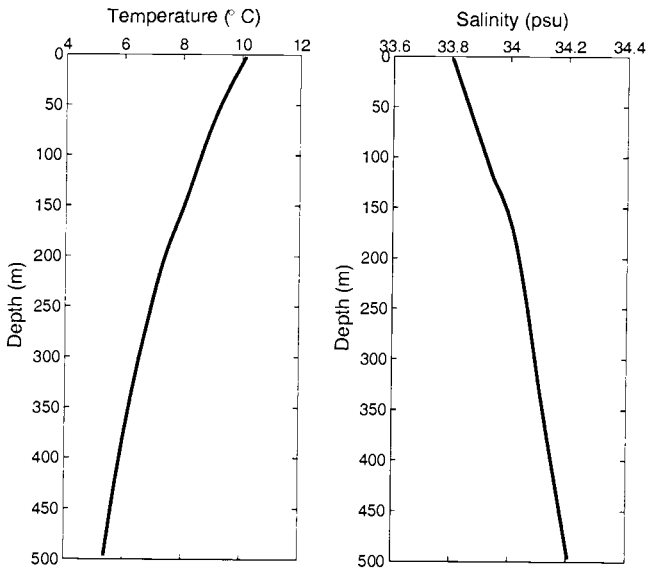

Figure 35. Initial temperature and salinity profiles.

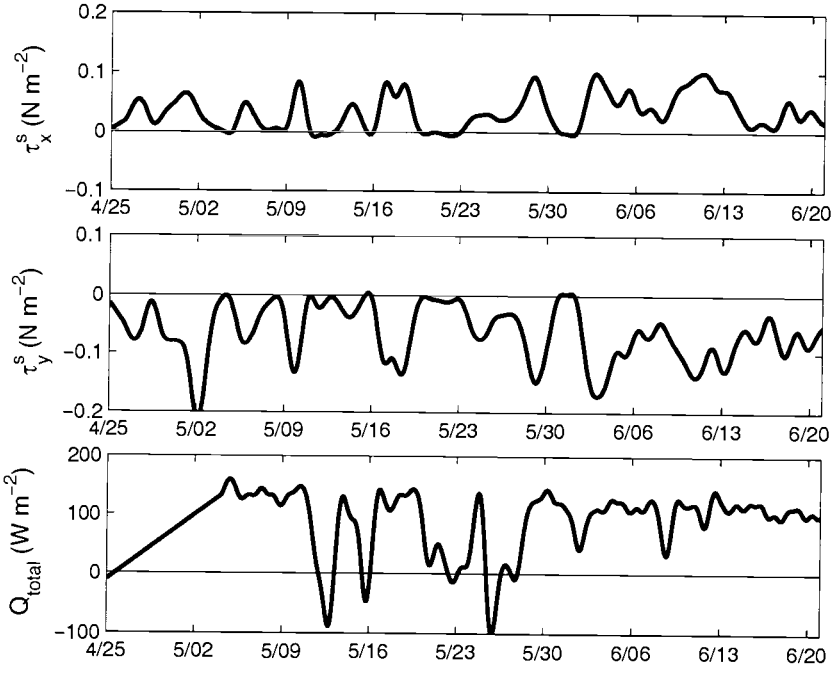

Figure 36. Across-shelf and alongshelf wind stress and total heat flux time series used to force the model. The instruments at D090 were not operational prior to May 5, therefore we used a linear regression of the NDBC 13 buoy winds and a linear increase in heat flux from near zero to the first measured value. Note that the wind stress components have been rotated to the model axis, which is aligned along 330 T. Wind and heat flux measurements from D090 were provided by E. Dever.

4.4 Model/Data Comparisons

4.4.1. Moored velocity and temperature observations

In order to verify the model's ability to represent the wind-driven shelf flow in this region, we conduct model-data comparisons with the available WEST observations. The first such comparison is with the moored velocity and temperature time series. Figure 37 shows depth-averaged velocities from the observations and the model at the D Line moorings. The depth-averaged velocities are computed over the depths of the mooring instruments. The wind stress vectors used to force the model are also plotted at the top. The time period shown is the entire duration of the model simulation (April 25 – June 20, 2001), including the spinup. However, because the moored time series are not available until May 5, correlations between the model and mooring observations are computed over May 5 – June 20. The complex correlation is highest at the inshore mooring (0.81), however the phase angle shows a fairly significant counterclockwise rotation of the modeled currents as compared to the observed D040 currents (23.44°). The correlation is lowest at the central D090 mooring (0.68), but the phase angle is very small (1.07°), indicating that the model does get the direction of the velocity fluctuations correct at this location. Correlations at the other 90-m moorings, C090 and E090 (not shown) are 0.64 with 7.73° phase angle and 0.57 with 6° phase angle, respectively. The correlation and phase angle at D130 (0.74 and 12.34°) lie between those at D040 and D090, and the root mean square error (rmse) at this location is significantly smaller in the alongshelf direction than at the other two moorings. The discrepancies between the model and observed time series are evidently due to the larger model velocity magnitudes during upwelling forcing (especially at D040 and D090) and the lack of a

significant reversal in the modeled velocities when upwelling winds relax (especially at D090 and D130). The model performs well at depth at the two offshore moorings due to decreased model velocities that match the observations more closely than at the surface (not shown).

We also compare the near-surface temperature time series at the D Line moorings for the same time period (Figure 38). The modeled temperature at the D040 and D090 moorings is 1-4 degrees cooler than the observations, with this difference a maximum during wind relaxation events when the observed temperature increases by 1-2 degrees. Thus, the model temperature has a weaker relaxation response than the observed temperature as expected from the weaker velocity relaxation response. The connection between observed northward velocities during relaxation and observed warming at the D line is likely the northward advection of warm, fresh water from San Francisco Bay, an input that is neglected in this modeling study.

Time mean depth-averaged velocity vectors from the observations and the model at the WEST mooring locations show the mean modeled velocities are larger than the mean observed velocities at all mooring locations except D130 (Figure 39). The first mode EOF, which explains 86% of the variance in both the model and observations, shows the model does better at matching the magnitude of the variability in the observations with a slight difference in phase. The phase and magnitude difference in the first mode EOF is greatest at D040. The time series of the EOFs have a correlation of 0.88. The observed amplitude is consistently higher than the model, with the biggest difference when the sign is positive. This corresponds to the observed reversal of velocities when upwelling winds relax, a

response that the model fails to represent completely as discussed earlier.

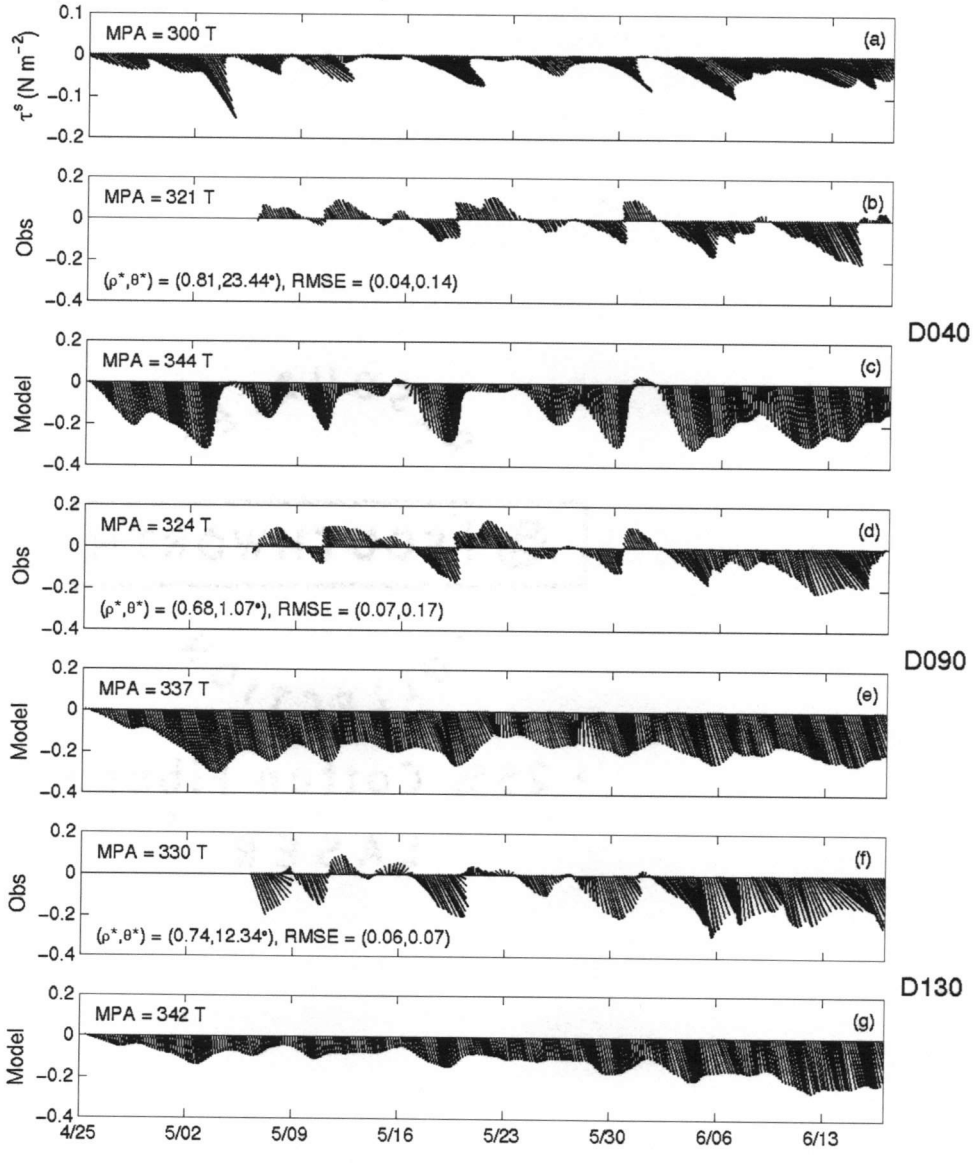

Figure 37. Time series of $\boldsymbol{\tau}^{\mathrm{S}}$ (a) and observed and modeled depth-averaged currents (m s^{-1}) at D040 mooring (b-c), D090 mooring (d-e), and D130 mooring (f-g). Major principal axes (MPA), magnitude of the complex correlation coefficient (ρ^*), phase angle (θ^*), and root mean square error for (u,v) are provided at each location. The 95% significance level for the velocity correlations is 0.51. The depths of the current meters range from 5 m to 33 m, 76 m, and 109 m, respectively, at D040, D090, and D130, with 2 m between each instrument. Moored velocity measurements were provided by E. Dever.

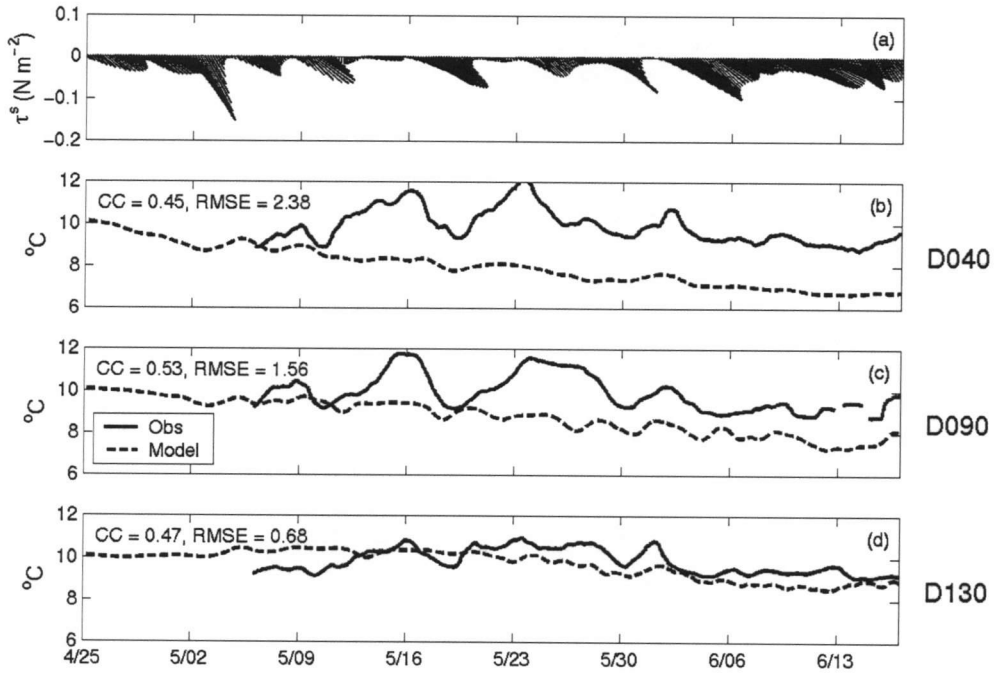

Figure 38. Time series of $\boldsymbol{\tau}^{S}$ (a) and observed and modeled near-surface temperatures at D040 mooring (b), D090 mooring (c), and D130 mooring (d). Correlation coefficients and root mean square error are provided at each location. The 95% significance level for the temperature correlations is 0.71. The depths of the temperature sensors range from 5 m to 30 m, 70 m, and 50 m, respectively, at D040, D090, and D130, with 5 m between each instrument. Moored temperature measurements were provided by E. Dever.

Further comparison between the moored velocity observations and the model is made by computing space-lagged correlation coefficients between model velocity components and between observed velocity components at the mooring locations (Table 4). The observed and modeled depth-averaged velocities (averaged over the measurement depths) are rotated to their respective principal axes calculated from the depth-averaged currents to objectively determine local values of the alongshelf and across-shelf velocity components. The observed correlations are shown in bold. For both the model and the observations, alongshelf correlations are computed for C090, D090, and E090 and across-shelf correlations for D040, D090, and D130.

The modeled and observed velocities have generally higher correlations alongshelf between the 90-m moorings than across-shelf on the D line. Alongshelf velocity correlations for v are high for both the model and observations at the 90-m moorings. The modeled response shows a lower u correlation for D090 – E090 (0.44) and C090 – E090 (0.08) than for C090 – D090 (0.73), whereas the observed correlation is similar between these pairs. Observed u correlations between D040 and the offshore D moorings are small and negative. The model correlations, however, are similar for all three D mooring pairs. This result illustrates a complexity in the observed flow at the inshore mooring location that is not captured by the model.

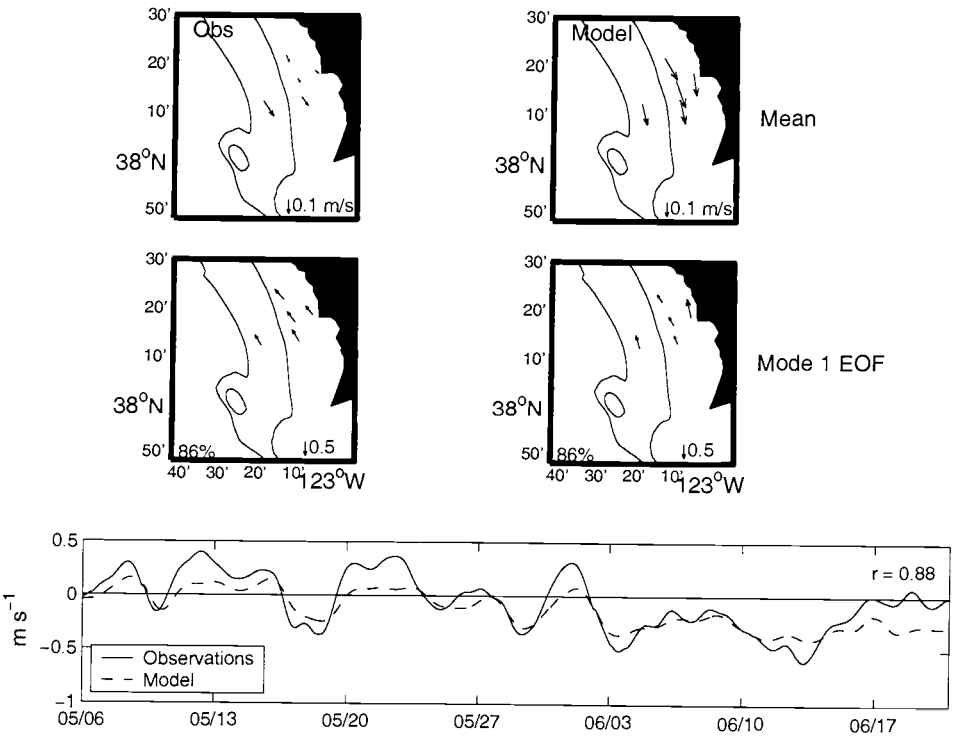

Figure 39. Mean (top) and mode 1 EOF (middle) of depth-averaged velocities from the mooring observations (left) and the model (right). The amplitude time series of the observed (solid line) and modeled (dashed line) mode 1 EOF is also shown at the bottom with the correlation coefficient. The 100-m and 200-m isobaths are provided.

Table 4. Summary of space-lagged correlation coefficients for observed (bold text) and modeled depth-averaged alongshelf velocity (v) and across-shelf velocity (u) at the mooring locations. The alongshelf and across-shelf velocities are determined by rotating to the principal axes of the depth-averaged currents. The time period over which the correlations are computed is the same as for the model-data comparisons presented in Figures 37, 38, and 39, May 5 – June 20, 2001. The 95% significance level for the correlations shown below is 0.51.

	D040		D090		D130		C090		E090	
	v	u	v	u	v	u	v	u	v	u
D040			**0.48**	**-0.01**	**0.38**	**-0.08**				
D090	0.70	0.66			**0.65**	**0.50**	**0.95**	**0.61**	**0.93**	**0.61**
D130	0.75	0.58	0.57	0.54						
C090			0.95	0.73					**0.94**	**0.51**
E090			0.91	0.44			0.85	0.08		

4.4.2. CODAR surface velocity observations

Daily-averaged surface velocities in the CODAR region (see Figure 33) are available from May 4 – June 20, 2001. We compare the modeled surface velocities over the same region in Figure 40. Shown are the complex correlation and phase, the time mean surface velocities, and the mode 1 EOFs from the CODAR observations and the model. Note the 100-m and 200-m isobaths are plotted for reference. The correlations are between 0.6 – 0.8 over much of the coverage area, with the exception of a few patchy areas at the north and south and near Cordell Bank, the topographic feature offshore of Pt. Reyes where the 100-m contour is closed. Phase angles are small in the middle of the CODAR region, with higher values around the edges. The

mean velocities are very similar offshore of the 100-m isobath, but near the coast, the modeled velocities are stronger. This pattern is consistent with the discussion of Figures 37 and 39 in which the depth-averaged velocity magnitudes at D130 are comparable, but the modeled velocities at the inshore moorings are stronger than the observed velocities. The root mean square errors between the observed and modeled mean surface velocities are 0.06 m s^{-1} and 0.11 m s^{-1} for the east/west and north/south components, respectively. The structure of the observed and modeled mode 1 EOFs is similar over the entire CODAR region.

The modal amplitudes (bottom) are highly correlated, with a correlation of 0.79. To attempt to determine if the mode 1 EOF represents the wind-driven mode, we compute cross-correlations between the wind stress components and the observed and modeled mode 1 time series. Significant agreement is found between τ_y^s and the mode 1 amplitudes, with zero-lag correlations of 0.88 and 0.63 for the observed and modeled modes, respectively. With the mode 1 amplitude lagging τ_y^s by one day, the model correlation increases to 0.66. Cross-correlations of τ_x^s with the mode 1 amplitudes are small at all time lags. We conclude that the mode 1 EOFs represent the dominant coherent wind-driven variability.

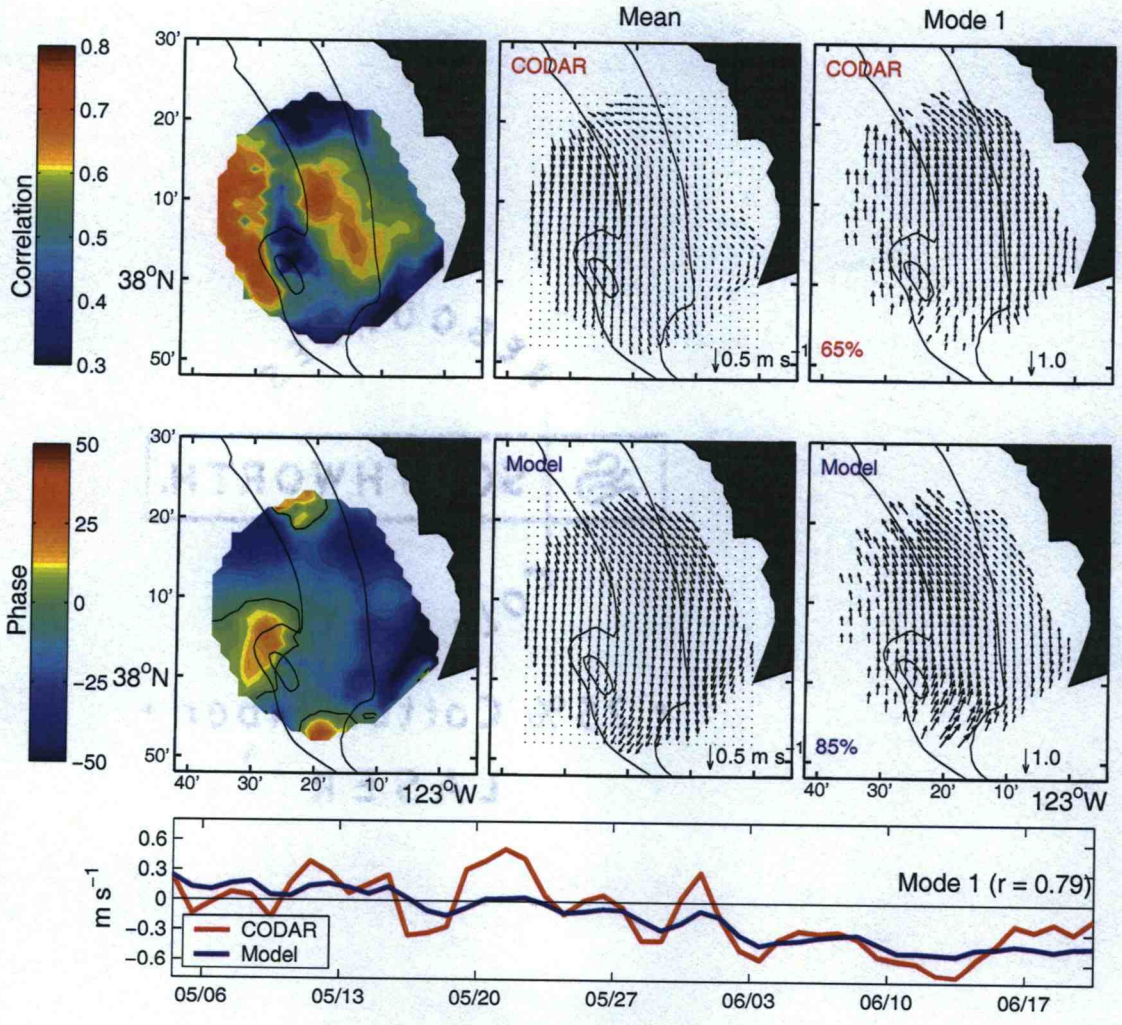

Figure 40. Magnitudes of complex correlation coefficients and phase angles (left) between modeled and observed surface currents, time mean surface velocity vectors (middle), and dominant mode 1 EOF (right) of surface currents from the CODAR observations (top) and the model (middle). The percentage of total variance explained by the mode 1 EOF is displayed in the lower left corner of each panel. The amplitude time series of the observed (red) and modeled (blue) EOFs are also shown at the bottom with the correlation coefficient. The 100-m and 200-m isobaths are shown in black. CODAR surface velocities were provided by D. Kaplan.

4.4.3. Shipboard hydrographic observations

Shipboard surveys following the large scale and small scale survey plans shown in Figure 33 allow an opportunity for model-data comparisons. The large scale survey encompasses WEST lines A, D, and F, while the small scale survey covers lines B, C, D, and E. In Figure 41, we compare two lines from a single CTD survey to the modeled potential density σ_θ during the event period we will later focus our discussion on. The modeled and observed σ_θ fields show similar characteristics. At the D line, a region of slightly downward-tilted isopycnals is found about 40 km offshore, as well as upwelled isopycnals at the surface from the coast to 30 km offshore in both the model and observations. The F line comparison is also similar, with the exception of an observed bulge of low density water extending from the surface to almost 100 m depth between 15 – 30 km offshore. This feature is possibly related to an output of warm, fresh water from San Francisco Bay that enters the study region when upwelling winds relax to near zero on May 20.

Figure 41 also shows scatter plots of all the observations available for each of these survey lines (five surveys in May/June on the D line and one survey on the F line). The correlation is very high on the F line (0.97) and the regression line has a slope near one (0.91). The correlation is lower on the D line (0.76) and more scatter is found, however the rmse values are similar at the two sites. The results for comparisons along lines A, C, and E (not shown), computed for one survey on lines A and E and two surveys on line C, have a high correlation (0.9) on the A line, while the C and E lines are much lower (0.51 and 0.44, respectively). A similar comparison between the modeled potential density and that observed with the tow-yo instrument, which encompasses the large scale survey lines A, D, and F,

yields a high correlation on the F line (0.93) and lower correlations on the A and D lines (0.54 and 0.53, respectively). The model clearly captures the density structure well at the northern end of the study region where the flow is relatively simple compared to that just north of Pt. Reyes and Cordell Bank, where the three interior survey lines are located. Somewhat surprising, perhaps, is the high correlation on the A line, where the model flow is quite complicated as we will illustrate.

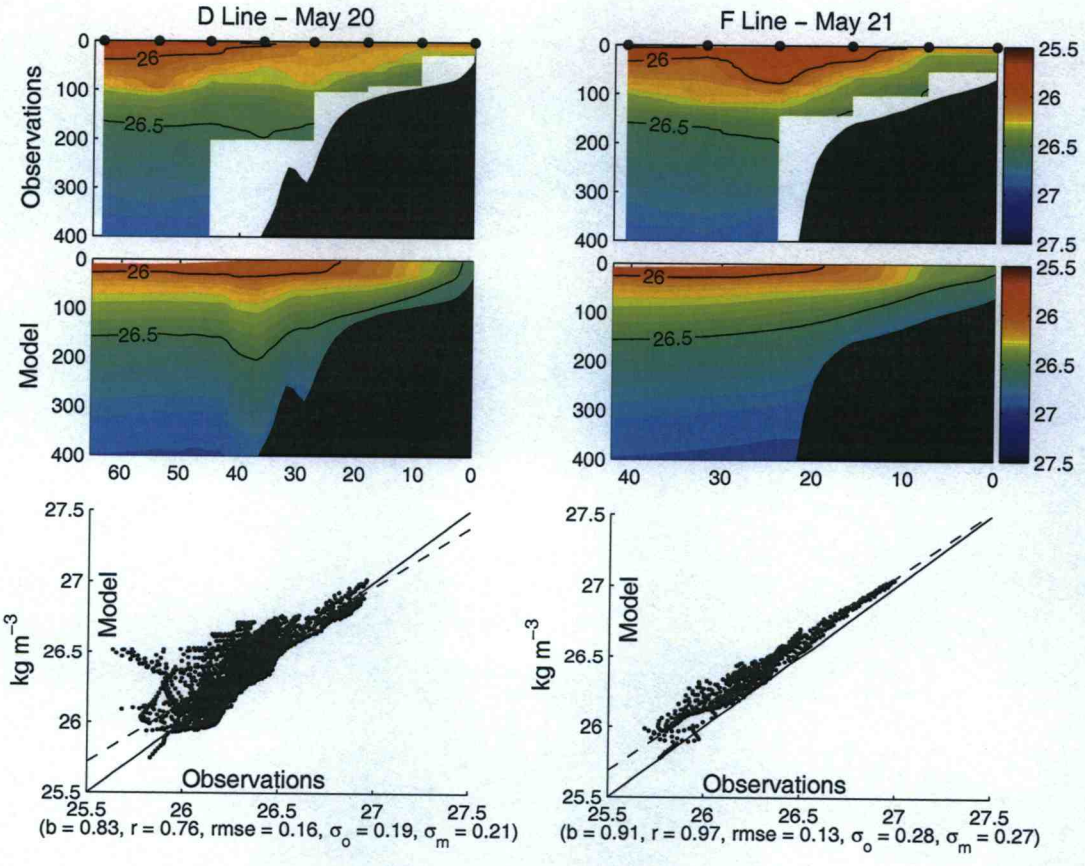

Figure 41. Potential density sections from CTD observations (top) and model (middle) along the D Line on May 20 (left) and the F Line on May 21 (right). Note the difference in the horizontal scales. At the bottom are scatter plots of all potential density observations compiled from five surveys during May/June for the D Line and one survey for the F Line. Provided below the scatter plots are the slope of the regression line (b), correlation coefficient (r), root mean square error (rmse), and variance from the observations (σ_o) and the model (σ_m). Hydrographic data were provided by N. Garfield.

4.5 Characteristics of Upwelling Season Response

We are interested in the mean wind-driven response of the shelf flow over the model simulation period. The winds are dominantly upwelling-favorable (Figure 36), however several relaxation events lasting 1–3 days occur during May and June 2001. The modeled shelf response at the surface can be seen in the region from Pt. Reyes to Pt. Arena in Figure 42. Clearly, the fields demonstrate that the upwelling response dominates the time mean. The surface velocity vectors show the location of the coastal upwelling jet, which separates slightly from the coast off Pt. Arena and significantly off Pt. Reyes, approximately following the 100-m isobath in both cases. Separation of the coastal upwelling jet from Pt. Reyes is a feature that has been previously discussed in the numerical model results of Gan and Allen (2002a). The largest variability in the velocity amplitude is off the capes and along the 200-m isobath. The variability is high off Pt. Arena and Pt. Reyes because the flows are complicated due to interactions with the variable coastline and bathymetry. Gan and Allen (2002a,b) found that, due to these interactions, the coastal capes in this area play a dominant role in the alongshelf variability of upwelling.

Another region of significant southward velocities at the surface offshore of the 200-m isobath is also apparent south of Pt. Reyes. This corresponds to a bifurcation in the separated coastal jet with an inshore portion of the jet following the 100-m isobath and another portion turning offshore, crossing isobaths, and returning southward about 60 km offshore. This double jet structure will be discussed in further detail later in this section.

The mean surface temperature field displays an upwelling response with the coldest water near the coast and increasing temperature offshore. An area of

relatively cold water is also found south of Pt. Reyes. The standard deviation of temperature shows high variability offshore of and south of Pt. Reyes due to the relatively large signal observed during upwelling relaxation in this region.

The coastal jet location is more obvious in the mean depth-averaged velocity than at the surface because velocities at depth decrease significantly offshore of the 200-m isobath (Figure 43). Overlaid on the depth-averaged velocity vectors are transport streamfunction contours, illustrating how the flow follows the coastline north of Pt. Reyes, where it veers offshore following the 100-m isobath. The transport is greatly decreased inshore of the 100-m isobath south of Pt. Reyes and a cyclonic recirculation area is found 50 km south of Cordell Bank between the regions of southward velocities associated with the bifurcated jet.

Bottom velocities have an onshore component under the coastal jet due to the bottom Ekman flow. Purely onshore bottom flow is found just south of Pt. Reyes. Consistent with the distribution of large bottom velocity, the bottom stress and bottom turbulent kinetic energy values are highest off Pt. Reyes and Pt. Arena. The turbulent kinetic energy variable (tke) is computed using the Mellor-Yamada level 2.5 closure scheme ($tke = 1/2q^2$). Nonlinearity in the surface flow is indicated off Pt. Reyes and Pt. Arena by the relatively large magnitudes of the surface relative vorticity divided by the Coriolis parameter f, which gives a measure of the local Rossby number. These results all point to the high spatial variability and complexity associated with the coastal jet separation. Mean potential density σ_θ at the bottom shows the isopycnals are approximately aligned with bathymetry contours with somewhat lower values inshore of the 100-m isobath south of Pt. Reyes. Although this pattern does not change significantly over the simulation period, bottom σ_θ

values on the shelf become greater over time due to the mean onshore bottom flow.

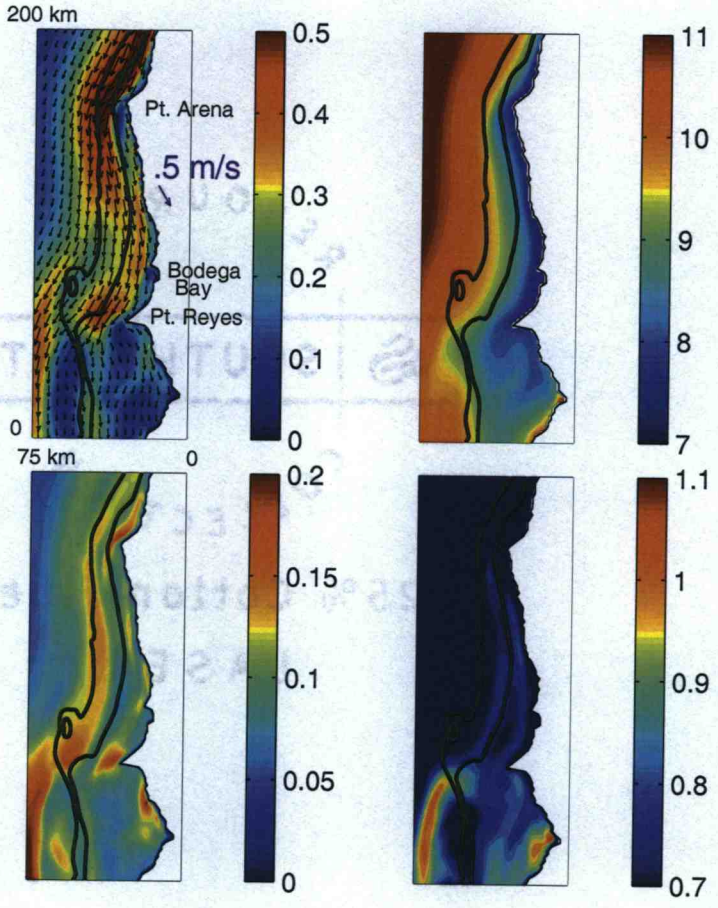

Figure 42. Time mean surface velocity vectors with magnitudes in color (upper left), surface temperature (° C) (upper right), standard deviation of the vector amplitudes (m s^{-1}) (lower left), and standard deviation of temperature (lower right) over the region from Pt. Reyes to Pt. Arena. The 100-m and 200-m isobaths are shown in black.

Sections of time mean alongshelf velocity v and potential density σ_θ at the locations shown in Figure 34 illustrate the significant variability in structure due to the flow response to the variable shelf geometry and coastline shape at different alongshelf locations (Figure 44). North of the F line (line 166), a coastal jet with a

defined core extends about 200 m deep and 30 km offshore, with slightly northward velocities inshore. Along the F line (line 148), the jet widens and shallows to about 100 m depth. Continuing south to the E line (line 130), the existence of two separate jet structures begins to develop, with stronger velocities in the inshore jet. Evidence in Figures 42 and 43 of weaker surface and depth-averaged velocities between the 100-m and 200-m isobaths at this location was discussed previously. The double jet feature, however, is better defined and more visible in the sections than in the horizontal velocity fields. The double jet can be seen in Figure 44 at each subsequent section south of line 130, with southward velocity increasing in the offshore jet and becoming larger than that inshore at Pt. Reyes and along the A line (lines 112 and 104). The jets move offshore between lines 112 and 104 due to separation off Pt. Reyes as shown in Figure 43. Areas with zero or slightly northward velocity are found along the continental slope between the two jets at all sites. A region of northward velocity from 5–20 km offshore at the A line illustrates the relaxation response that is strongest south of Pt. Reyes. The relaxation contribution to the time mean also causes slightly northward velocities near the coast just south of Pt. Arena (line 166), where a relaxation response is present, but much weaker than that south of Pt. Reyes.

The E line (line 130) is located about 10 km north of Cordell Bank, so it is possible that upstream influence of the bank causes this double jet velocity structure, which strengthens to the south as the isobaths are modified significantly by the presence of the bank (see Figure 34). Other indications of upstream influence of Cordell Bank will be discussed later in connection with Lagrangian calculations presented in section 4.6.2. Attempts to find evidence of a similar jet structure in the

observations, both from WEST and from other northern California programs such as CODE, did not lead to any conclusive results. It is unclear, however, whether an appropriate comparison could be made from these observations due to their limited coverage areas. The southernmost CODE survey line is just north of the E line, and the WEST CODAR region does not extend offshore of the 200-m isobath around Cordell Bank and Pt. Reyes. WEST shipboard ADCP surveys during May 2001 (M. Roughan, personal communication) are available at the A, D, and F lines, but only for a few days. The ADCP measurements do not always extend far enough onshore or offshore to capture the necessary range for a comparison. However, one ADCP survey on May 26 that extends offshore along the D line (line 124) shows negative v velocity on the shelf, a region of near zero v just offshore at the shelf break (30 km from the coast), and surface-intensified negative v from about 32 – 50 km from the coast. The model v, sampled in the same manner as the observations, has a similar across-shelf structure. This is clearly a qualitative comparison, but one which shows that relevant available observations are not inconsistent with the model results.

Time mean density fields do not exhibit as noticeable a transformation between alongshelf locations, although the region of upwelled isopycnals extends farther offshore as the location progresses south from line 166 to line 104. This difference between sections is largest at the A line (line 104), where the 26.3 kg m^{-3} isopycnal surfaces approximately 40 km offshore, as compared to 15–25 km offshore at lines 166–112. The contrast in across-shelf density front location illustrates that more dense water is upwelled at the surface over a larger expanse of the shelf south of Pt. Reyes, where the alongshelf coastal jet is displaced offshore relative to its location north of Pt. Reyes.

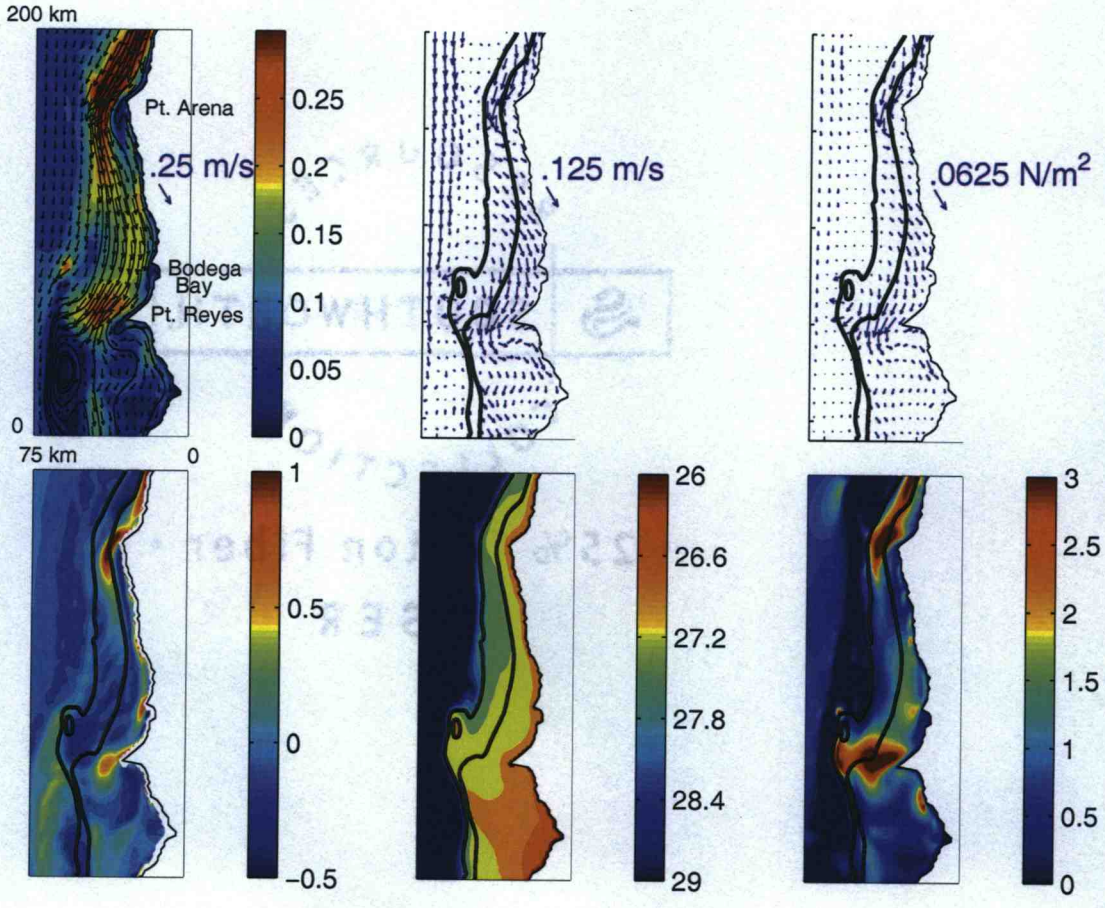

Figure 43. Time mean depth-averaged velocity vectors with magnitudes in color and contours of transport streamfunction in black (upper left), bottom velocity vectors (upper middle), bottom stress vectors $\boldsymbol{\tau}^{\mathrm{b}}$ (upper right), surface relative vorticity ζ divided by f (lower left), bottom potential density σ_θ in kg m^{-3} (lower middle), and bottom turbulent kinetic energy (tke) in 10^{-4} m^2 s^{-2} (lower right).

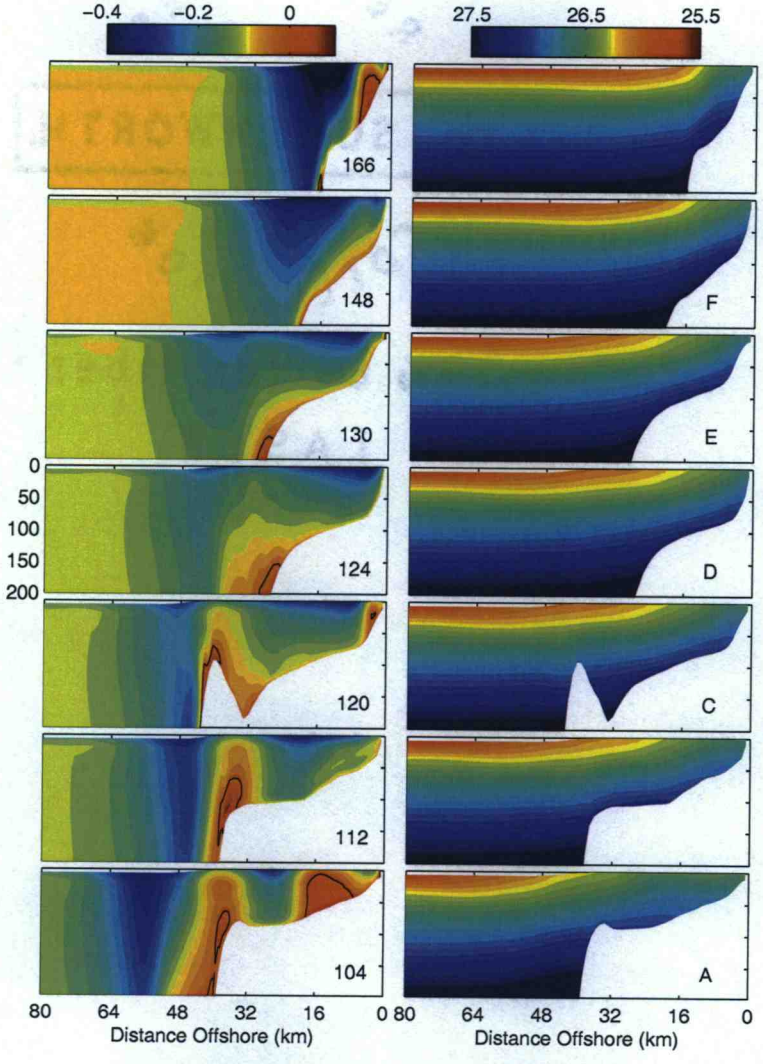

Figure 44. Sections of time mean alongshelf velocity v in m s^{-1} (left) and potential density σ_θ in kg m^{-3} (right) plotted as a function of depth (m) and distance offshore (km). The zero v contour is shown in black. The alongshelf grid numbers shown in Figure 34 are in the lower right corner of each v section and corresponding WEST survey lines are in the lower right corner of each σ_θ section.

4.6 Dynamical Analysis of Upwelling and Relaxation Wind Event

4.6.1. Eulerian analysis

We now focus our discussion on a specific wind event from May 17 – 23, 2001 during which the wind stress begins as upwelling-favorable and greater than 0.1 N m^{-2} until May 19, at which time it decreases to near zero on May 20. Both components of the wind stress remain near zero until May 23 (see Figure 36). The modeled upwelling and relaxation response during this event is representative of those throughout the summer simulation period. This analysis also allows a contrast between upwelling and relaxation conditions over a typical event time scale. Shown in Figure 45 are surface velocity vectors, surface temperature, and surface elevation η fields on May 18, 20, and 22. The wind stress during the event is provided at the top for reference. The location of the core of the alongshelf coastal upwelling jet on May 18 is between the 100-m and 200-m isobaths north of Pt. Arena and approximately along the 100-m isobath south of Pt. Arena. The jet separates from the coast south of Pt. Arena and to a greater extent south of Pt. Reyes. Surface temperatures are coldest and surface elevations are lowest near the coast due to upwelling, with the coldest water north of Bodega Bay and a large region of cold water with low η found south of Pt. Reyes from the coast to the 100-m isobath.

On May 20, surface velocities decrease everywhere except in the coastal jet region. Surface temperatures decrease between Pt. Reyes and Bodega Bay due to the southward advection of cold water from north of Bodega Bay. Surface elevations decrease near the coast by 2-3 cm. May 22 shows the flow response to wind relaxation with a decrease in surface velocities everywhere, a warming of surface temperatures near the coast, and an increase in surface elevation near the coast.

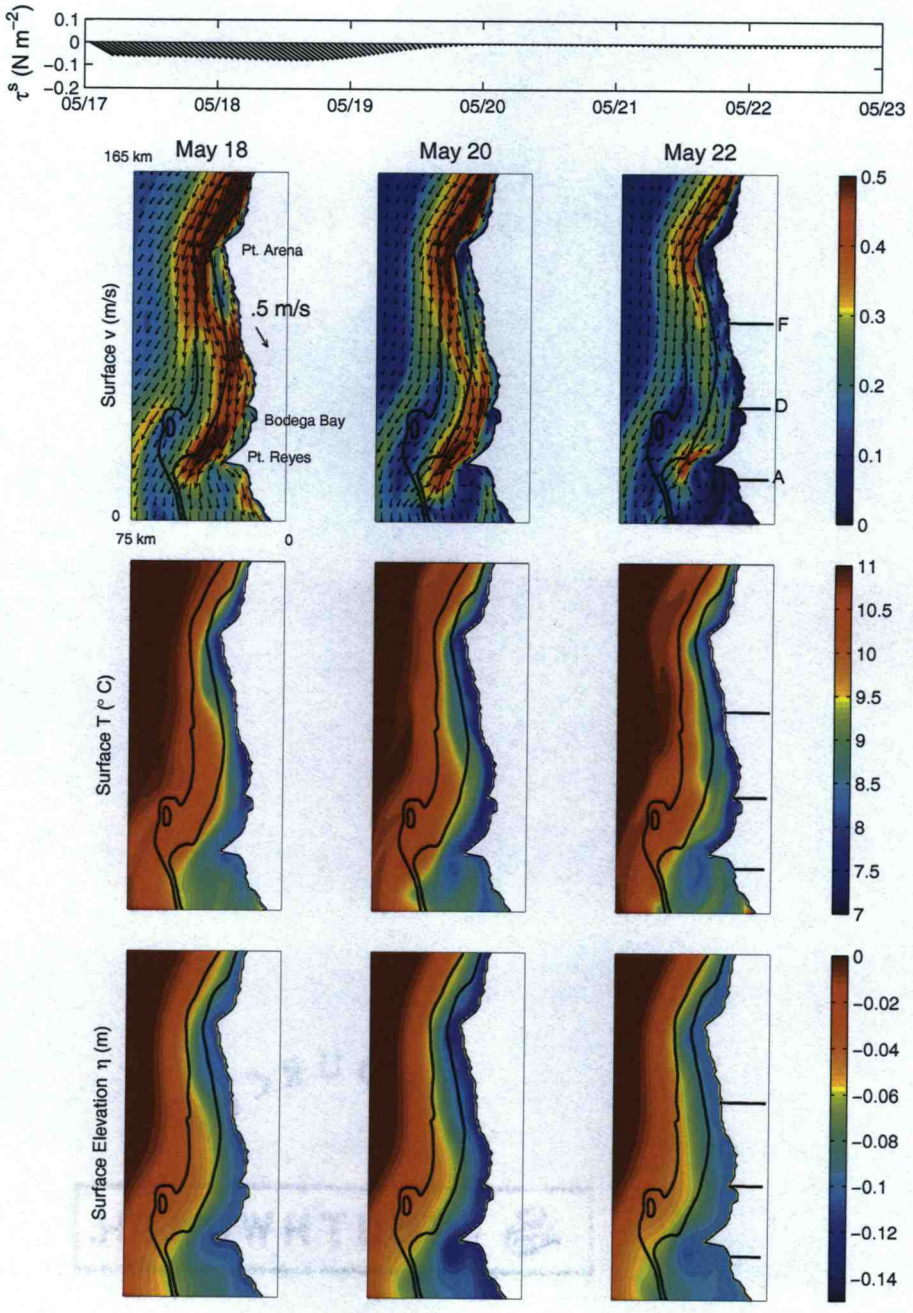

Figure 45. Daily-averaged surface velocity vectors with magnitudes in color (top), surface temperature (middle), and surface elevation (η) fields over the region from Pt. Reyes to Pt. Arena on May 18, 20, and 22. The wind stress during the event period is given at the top. Three section locations along the A, D, and F lines that will be detailed in Figures 49, 50, and 53 are shown as black lines.

In order to examine the dynamics of this event in more detail, we study fields of the depth-averaged velocity and alongshelf momentum term balance in Figures 47 and 46. We write the momentum equation for the depth-averaged alongshelf flow in the y direction as

$$\frac{\partial V}{\partial t} + U\frac{\partial V}{\partial x} + V\frac{\partial V}{\partial y} - G^y - F^y + fU + \frac{1}{\rho_0}\frac{\partial p}{\partial y} - \frac{1}{\rho_0 D}\tau_s^y + \frac{1}{\rho_0 D}\tau_b^y = 0, \qquad (27)$$

where $(U,\ V)$ are the depth-averaged currents in the $(x,\ y)$ directions, τ_s^y and τ_b^y are the y components of the surface and bottom stress, respectively, G^y is the dispersion term, F^y is the horizontal diffusion term, f is the Coriolis parameter, and D is the water depth. We refer to the terms $\frac{\partial V}{\partial t}$ as acceleration, $U\frac{\partial V}{\partial x} + V\frac{\partial V}{\partial y} - G^y - F^y$ as advection, $fU + \frac{1}{\rho_0}\frac{\partial p}{\partial y}$ as the ageostrophic pressure gradient, $\frac{1}{\rho_0 D}\tau_s^y$ as wind stress, and $\frac{1}{\rho_0 D}\tau_b^y$ as bottom stress.

The depth-averaged velocity is southward with magnitudes of 0.2–0.3 m s^{-1} in the coastal jet, which is shown to separate off Pt. Arena and Pt. Reyes. Weaker velocities are found in the lee of the capes. The bifurcation of the jet, as apparently caused by upstream influence of Cordell Bank, is also shown with weak velocities directly over and north of the bank. Velocities increase near the capes on May 20, then decrease everywhere on May 22 following two days of near zero winds. On May 18, bottom stress values are high near the coast due to forcing of appreciable currents in the shallower water depths and off Pt. Reyes and Pt. Arena because bottom velocities are relatively large near the capes. Wind stress values are large everywhere on the shelf due to the spatial uniformity of the wind forcing. As the winds decrease on May 20, bottom stress values decrease near the coast and the wind stress is near zero everywhere. Bottom stress weakens further on May 22 while wind stress values increase slightly near the coast.

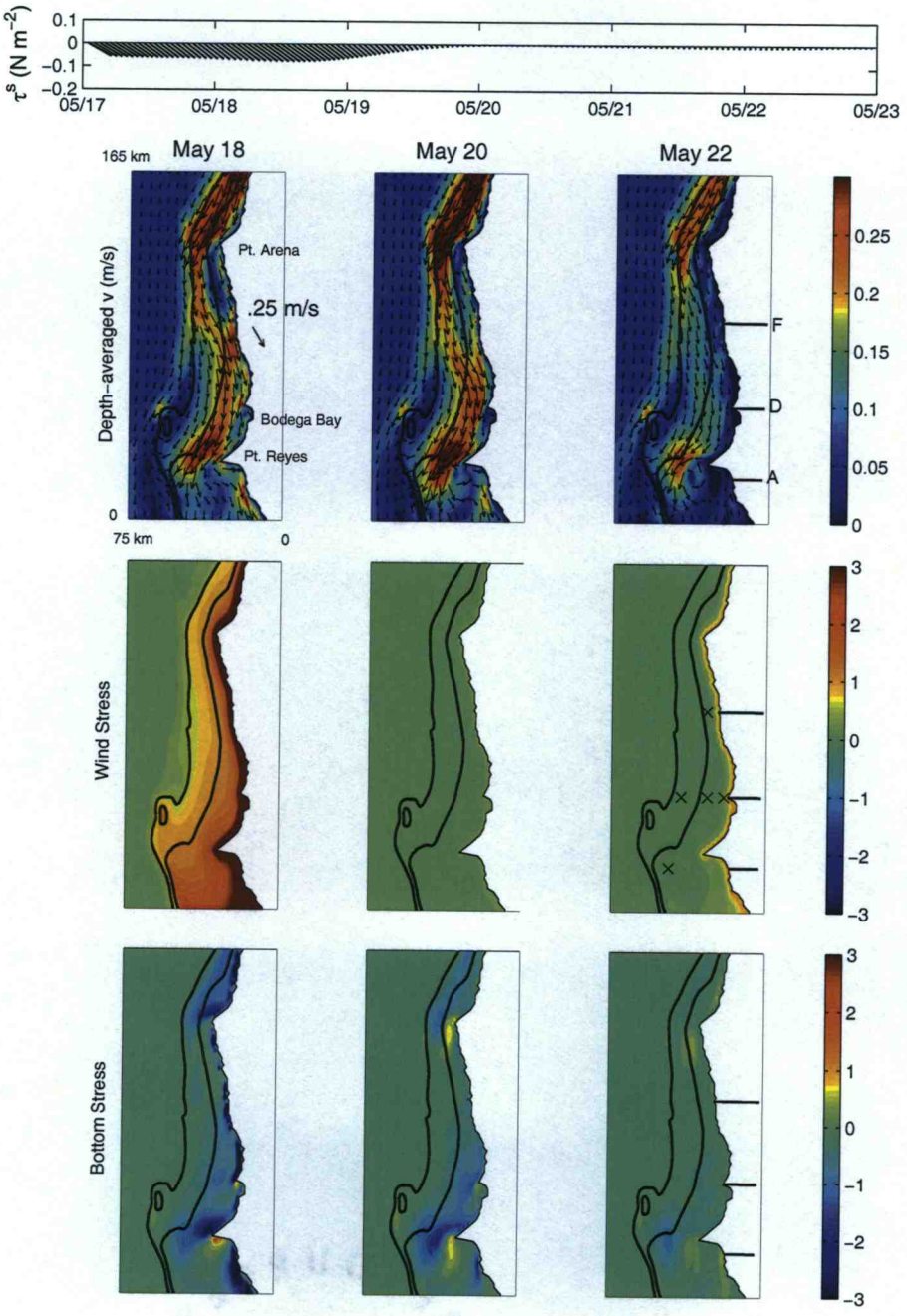

Figure 46. Depth-averaged velocity vectors and magnitudes in color (top), alongshelf surface stress term (middle) and alongshelf bottom stress term (bottom) from the depth-averaged alongshelf momentum balance over the region from Pt. Reyes to Pt. Arena on May 18, 20, and 22. The terms are on the left-hand side of the equation and oriented along the model y-axis. The units for each term are 10^{-6} m s^{-2}. The locations of the time series shown in Figure 48 are marked with a black $\times$ in the middle right panel.

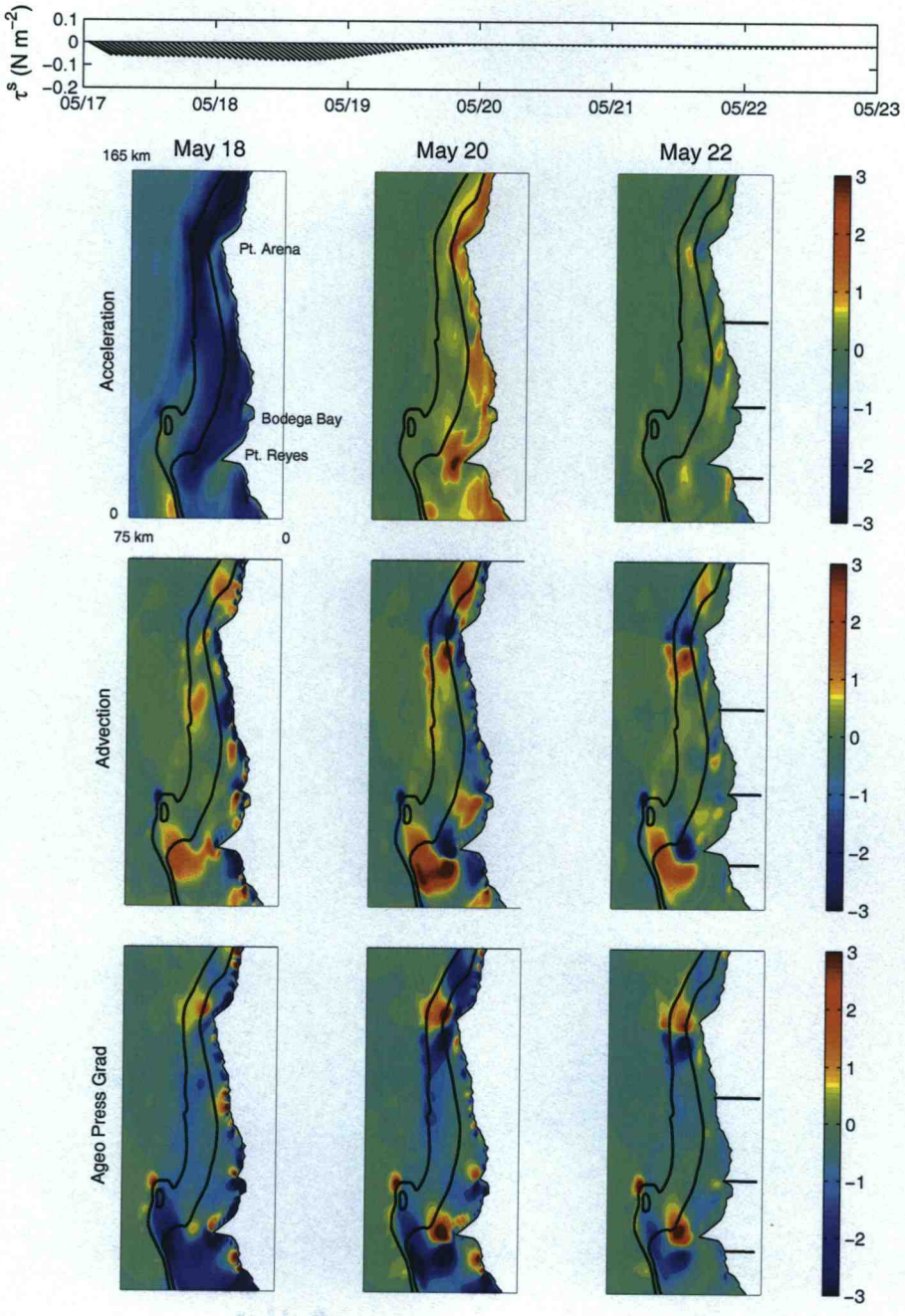

Figure 47. Acceleration term (top), nonlinear advection term (middle), and ageostrophic pressure gradient term (bottom) from the depth-averaged alongshelf momentum balance over the region from Pt. Reyes to Pt. Arena on May 18, 20, and 22. The terms are on the left-hand side of the equation and oriented along the model y-axis. The units for each term are 10^{-6} m s^{-2}.

In Figure 46, large negative acceleration on May 18 is due to the continued strengthening of the southward coastal jet caused by upwelling wind stress forcing. In the advection term, we see a spatial pattern of negative advection values offshore and north of Pt. Arena and Pt. Reyes and positive advection values to the south. This corresponds to southward spatial acceleration of the southward coastal jet off the capes and southward spatial deceleration south of the capes. The advection terms are balanced primarily by the opposite-signed ageostrophic pressure gradient term. Note the characteristic spatial variation of the advection and ageostrophic pressure gradient terms around Pt. Reyes and Pt. Arena also occurs on a smaller scale off Bodega Head, the small cape at the northern end of Bodega Bay in the center of the WEST study area.

As the winds decrease, the acceleration term switches sign on May 20 over the shelf and the alongshelf velocity field decelerates. The regions of large advection and ageostrophic pressure gradient off the capes increase in area and magnitude on May 20. All three terms in Figure 46 then weaken on May 22.

The characteristics of the alongshelf pressure gradient pattern are of interest because the alongshelf topographic and coastline variability associated with Pt. Reyes and Pt. Arena are important factors in the dynamics of the shelf flow response. Gan and Allen (2002a) found a similar alongshelf pressure gradient distribution during upwelling-favorable winds in numerical modeling studies of this region. They explain the pattern as a response to decreased surface elevation south of the capes, which is related to increased velocities around the capes. In addition to a geostrophic balance in the across-shelf direction, which leads to lower surface elevation in regions of increased alongshelf velocities, nonlinear advection contributes significantly near

Pt. Reyes and Pt. Arena. This leads to a gradient wind-like balance with a nonlinear centrifugal force term V^2/R that is important due to increased V and decreased radius of curvature R around the capes. Thus, the surface elevation response is tied to the alongshelf velocity through the across-shelf momentum balance, and the modified surface elevation field serves to intensify the alongshelf pressure gradient. In this study, we find similar results in daily plots of surface elevation η (Figure 45) and in the ageostrophic pressure gradient and nonlinear advection terms from the across-shelf momentum balance (not shown). The surface elevation is low near the coast and south of Pt. Reyes and an across-shelf ageostrophic pressure gradient balances a relatively large nonlinear advection term near Pt. Reyes and also near Pt. Arena. Throughout the event, surface elevation is a minimum in the region south of Pt. Reyes on May 20, and correspondingly, depth-averaged velocity vectors are largest just off Pt. Reyes and Pt. Arena on May 20 (Figure 46). In support of the previous argument, the change in η and depth-averaged velocity from May 18 – 20 is consistent with the strengthening of the alongshelf nonlinear advection and ageostrophic pressure gradient terms.

Time series of the modeled depth-averaged alongshelf momentum terms at the locations of the D line moorings and at 90 m depth on the A and F lines allow us to investigate further the dynamics as they develop in response to the variable winds and the differences as a function of shelf location (Figure 48). Several upwelling events occur during the period shown, including the event that is the focus of this discussion. At all five moorings, the characteristics during upwelling forcing include a positive surface stress term that forces a negative acceleration of the upwelling jet followed by a negative bottom stress. The relative magnitude of the bottom

stress decreases as the depth increases from D040 to D130. The major qualitative difference between the dynamics at D040 and the offshore moorings is the sign of the ageostrophic pressure gradient and advection terms. At D040, the advection is negative, and is balanced by a positive ageostrophic pressure gradient, presumably reflecting a southward spatial acceleration of the nearshore alongshelf current around Bodega Head, similar to the more intense behavior found off Pt. Reyes and Pt. Arena (Figure 46) during upwelling wind forcing. In contrast, generally positive advection terms are found at the other four moorings, illustrating the southward spatial deceleration of the coastal jet as it moves offshore to adjust to the presence of Pt. Reyes. The ageostrophic pressure gradient is generally negative, balancing positive wind stress and advection and also positive acceleration when it occurs during wind relaxation events. The ageostrophic pressure gradient term has the highest zero-lag correlation with the wind stress term (correlation coefficients of 0.42–0.78) and the advection term (correlation coefficients of 0.51–0.9) at all five moorings, with the exception of F090, which has a very low correlation between the advection and ageostrophic pressure gradient at all lags.

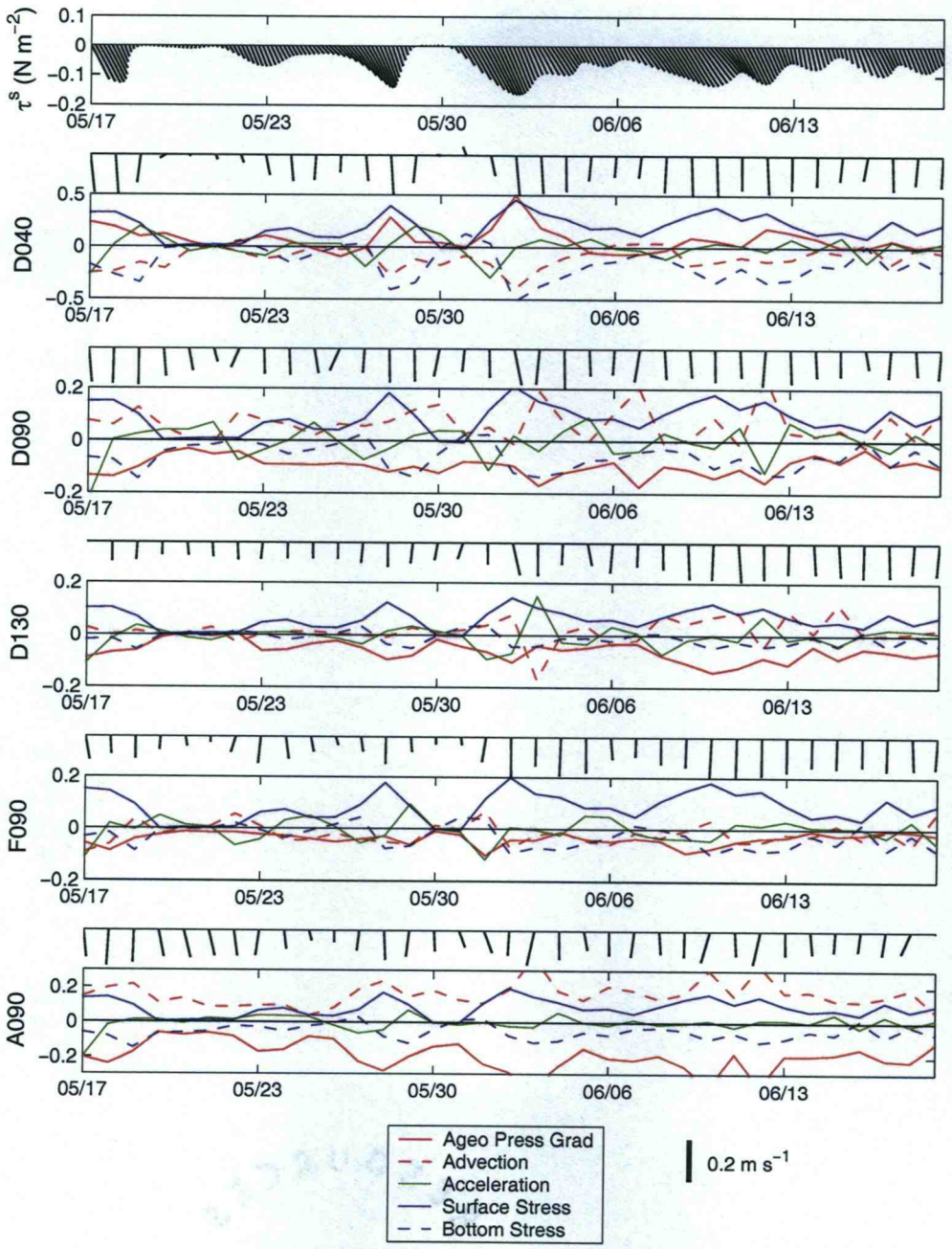

Figure 48. Time series of depth-averaged alongshelf momentum balance terms (10^{-5} m s^{-2}) at the D line moorings and at 90 m on the A and F lines from May 17 – June 20. The terms are on the left-hand side of the equation and are rotated to the direction of the time mean depth-averaged velocity at each mooring (337 T at D040, 335 T at D090, 342 T at D130, 354 T at A090, and 306 T at F090). Time series of corresponding depth-averaged velocity vectors (relative to the same direction) from these locations are also shown. The scale for the velocity vectors is given at the bottom. Note the different vertical scale for the time series of terms at D040 and A090.

Alongshelf variability is also illustrated by the different responses at A090, F090, and D090. To the north, F090 shows similar wind stress and acceleration magnitudes, but smaller ageostrophic pressure gradient and advection terms, reflecting smaller effects of alongshelf topographic variability. The lack in correlation between the pressure gradient and advection time series also points to a significantly different response than that in the regions of influence of capes, as represented by the other time series. To the south, the terms at A090 show considerably larger ageostrophic pressure gradient and nonlinear advection terms. These terms are dominant in this region because of the influence of Pt. Reyes on the alongshelf advection processes and on the alongshelf pressure gradient field, as discussed previously. Acceleration, surface stress and bottom stress play a smaller role in the balance. The bottom slope is very small in this portion of the shelf at the A line, so that a wide range of sites, all with depths of 85 – 90 m, produce quantitatively different alongshelf momentum balances, but with the common characteristic that the dominant balance is between the nonlinear advection term and the ageostrophic pressure gradient. The A line dynamics therefore cannot be identified by approximate water depth, but rather across-shelf location must also be considered in interpreting the momentum balance time series.

Also of interest is the variability of the flow response (Figure 49) and the dynamical balances (Figure 50) across sections at the A, D, and F lines. The structure of the alongshelf velocity and density during the event is quite different at these locations, as expected from the time mean fields discussed in Figure 44. The F line (line 148) shows a coastal jet that weakens from May 20 to May 22 with near-zero velocities inshore on May 22. The upwelled isopycnals also retreat

slightly toward the coast following the relaxation of upwelling winds. The jet region is characterized (Figure 50) by positive advection, reflecting southward spatial deceleration in the slightly onshore-directed coastal jet (Figure 46). Nonlinear advection is balanced by a negative ageostrophic pressure gradient which also, through the Coriolis force, balances vertical diffusion in the surface and bottom boundary layers. The acceleration term (not shown) is about one half the magnitude of the other terms and has a spatial pattern similar to the nonlinear advection term with opposite sign. This corresponds to increasing southward velocities when the jet strengthens on May 18.

At the D line (line 124), the velocity structure is more complex due to the strong inshore jet and weaker offshore jet with northward velocities at depth in between. The momentum term balance shows a pattern of negative advection corresponding to southward spatial acceleration (balanced by a positive pressure gradient) on the offshore side of the weaker offshore jet, and positive advection corresponding to southward spatial deceleration (balanced by a negative pressure gradient) on the inshore side. In contrast, the dynamical structure of the stronger inshore jet is similar to that at the F line. This result leads to the conclusion that the inshore portion of the bifurcated jet matches the signature of the coastal upwelling jet north of Pt. Reyes, whereas the offshore portion of the bifurcated jet exhibits different dynamics and a generally weaker dynamical response in the momentum balance fields.

At the southernmost A line (line 104), the complexity increases as velocities in the offshore jet are as strong as those in the inshore jet. Both jets are displaced offshore relative to their D line locations due to separation off Pt. Reyes, and a

region of significant northward velocities is found inshore. The density front is 30 km offshore and relatively dense water covers the broad shallow shelf inshore, illustrating the effectiveness of the upwelling shelf circulation at the A line. The bottom boundary layer under the inshore jet is also displaced offshore at the A line relative to the D and F lines (Figure 50). Large negative vertical diffusion, corresponding to onshore flow, is also found in the water column on May 20 and 22 on the inshore side of the southward coastal jet, about 20–25 km offshore. Inshore below the region of northward velocities near the coast is positive vertical diffusion in the bottom layer, corresponding to offshore flow. Hence, convergence in the bottom boundary layer could lead to the considerable vertical diffusion values that extend upwards into the water column at the boundary between the southward and northward velocities. The advection and ageostrophic pressure gradient fields on the shelf, which have maximum values on May 20, show significant vertical and horizontal structure. This includes large positive advection in the region of strong northward velocities within about 20 km of the coast (corresponding to northward spatial acceleration), which is balanced by a negative (northward) pressure gradient force. The advection and pressure gradient terms switch sign progressing offshore into the region of the nearshore coastal jet, then once again between the two jets where alongshelf velocities are near zero, and a final time in the region of the offshore jet. This pattern reflects the spatial acceleration and deceleration associated with the complex velocity structure on the shelf and slope just south of Pt. Reyes. The magnitude of these terms in the offshore jet region is weaker than that inshore, as discussed previously along the D line.

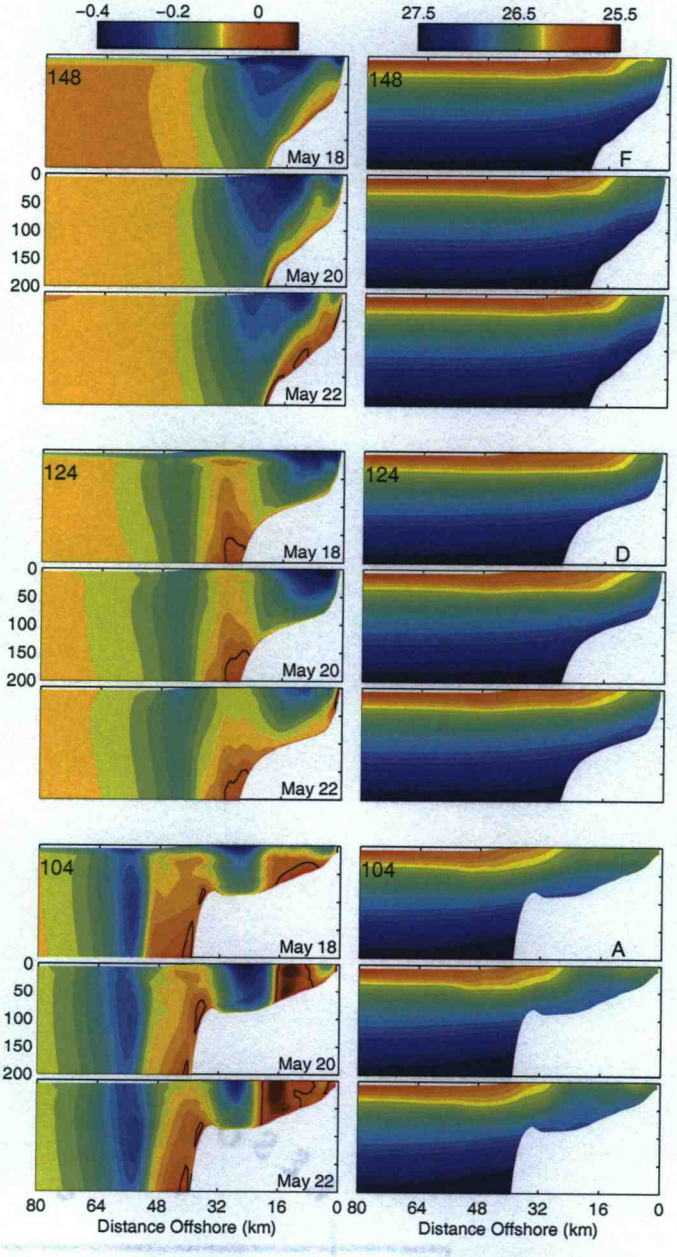

Figure 49. Sections of alongshelf velocity v (left) and potential density σ_θ (right) along the F (line 148 – top), D (line 124 – middle), and A (line 104 – bottom) lines on May 18, 20, and 22. The zero v contour is shown in black.

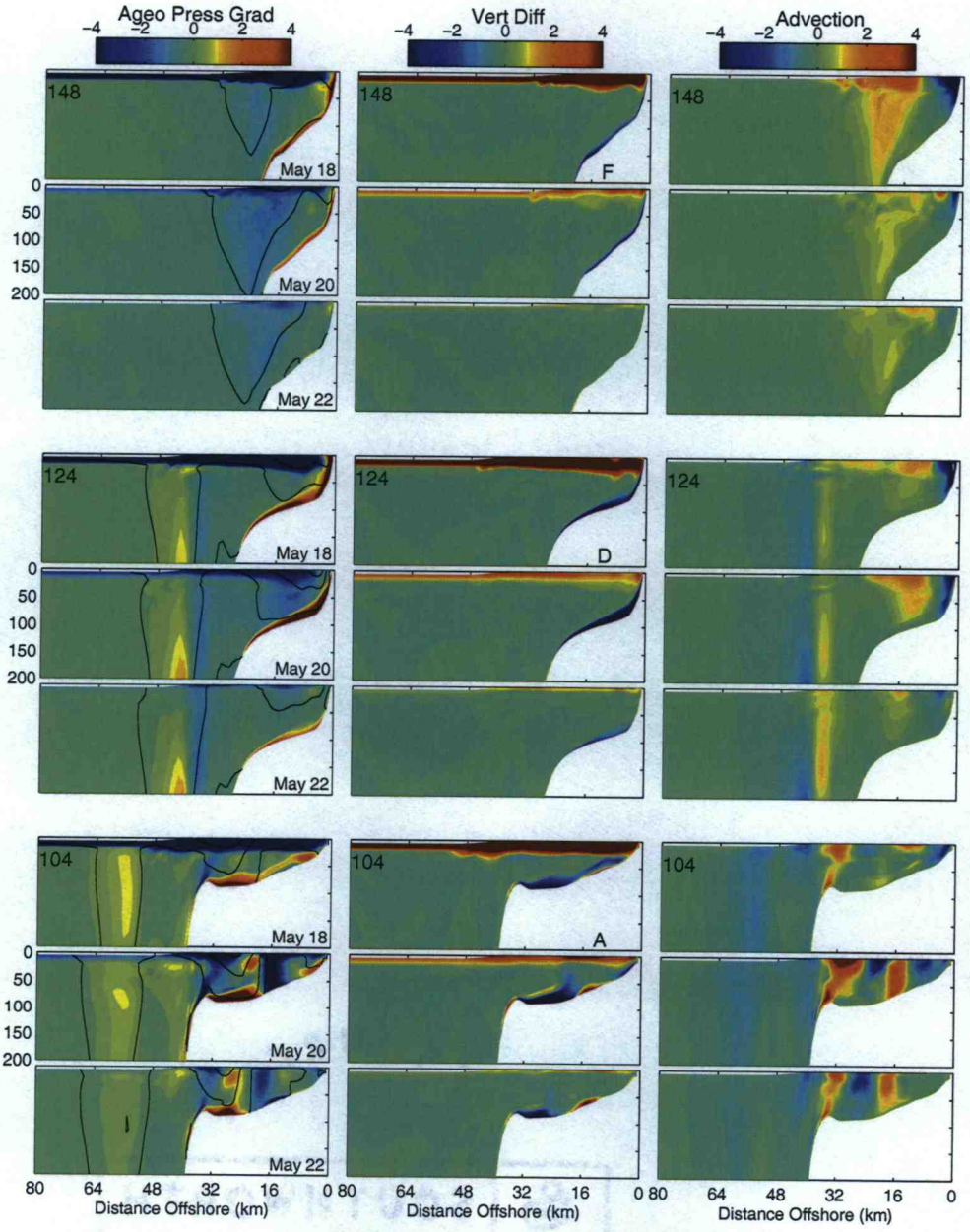

Figure 50. Sections of the alongshelf momentum term balance, including the ageostrophic pressure gradient (left), vertical diffusion (middle), and advection (right) on May 18, 20, and 22. The section locations are the same as in Figure 49. Contours of v with a 0.1 m s^{-1} contour interval are shown in black over the pressure gradient contours. The terms are on the left-hand side of the equation and are rotated to the direction of the cross-sectional average of the time mean (over the entire simulation period) depth-averaged velocity (319 T on line 148, 342 T on line 124, and 325 T on line 104). The units for each term are 10^{-6} m s^{-2}.

4.6.2. Lagrangian analysis

Lagrangian fluid motion is calculated using two different techniques. The first approach involves computing parcel trajectories by solving the differential equations

$$\frac{dx}{dt} = u, \qquad \frac{dy}{dt} = v. \tag{28}$$

Parcels are indexed by their initial positions at every (x, y) grid point. In the vertical, parcels are initialized at the center of the grid cell next to the surface and remain at this depth throughout the simulation. Numerical solutions to (28) are calculated utilizing a fourth-order Milne Predictor Hamming Corrector scheme. The time step used for the Predictor-Corrector scheme is the model internal time step. The updated positions obtained from the solutions to (28) are recorded daily for each initial parcel position.

In addition to tracking individual water parcels, we utilize a second technique that provides Lagrangian trajectories for a continuous field of parcels. This approach involves the definition of three Lagrangian label fields that are advected by the model velocities (Kuebel Cervantes et al., 2003). The Lagrangian labels, $X(x, y, z, t)$, $Y(x, y, z, t)$, and $Z(x, y, z, t)$, satisfy the following equations:

$$\frac{DX}{Dt} = 0, \qquad \frac{DY}{Dt} = 0, \qquad \frac{DZ}{Dt} = 0, \tag{29}$$

where $\frac{D}{Dt} = \frac{\partial}{\partial t} + u\frac{\partial}{\partial x} + v\frac{\partial}{\partial y} + w\frac{\partial}{\partial z}$. The initial conditions are

$$X(x, y, z, t = 0) = x, \quad Y(x, y, z, t = 0) = y, \quad Z(x, y, z, t = 0) = z. \tag{30}$$

For calculations without errors, i.e., those performed in the limit of vanishing spatial grid sizes and time steps, the Lagrangian parcel trajectories obtained from both techniques would be equivalent.

In this application of the Lagrangian labels, the initial Y and Z labels are a function of their initial alongshelf and vertical location, respectively, as in (30). To aid in the physical interpretation, however, the X label is initialized as the water depth h,

$$X(x, y, z, t = 0) = h(x, y). \tag{31}$$

This allows a ready assessment of across-isobath displacement of water parcels, which we refer to as onshore/offshore displacement in the following discussion. The labels X, Y, and Z are calculated as fields on the model grid with the third-order upstream bias advection scheme. Since the model also includes a parameterization of small-scale turbulence, these Lagrangian parcel trajectories comprise only the resolved part of the full fluid motion represented in the model.

Examination of the time evolution of the label fields helps to provide insight into the Lagrangian characteristics of the flow. Surface distributions of the Y label and of the Lagrangian parcels, both initialized on May 17, are shown in Figure 51. The colorbar indicates values from 100 – 400 km, measured as distance from the southern boundary of the model domain. The alongshelf locations of the surface parcels (bottom) have been color-coded to allow a comparison of the evolution of the surface Y label (top) and the parcels. A striking feature in Figure 51 is the significant southward advection in the region of the coastal jet, with parcels being advected up to 100 km southward by May 22. The structure shows a well-defined split in the trajectories that occurs near Cordell Bank, with significant southward advection both offshore of the bank and inshore along the 100-m isobath. In regions inshore of the 100-m isobath, on Cordell Bank, and south of Pt. Reyes, the southward surface advection is decreased. Just off Pt. Reyes, a cyclonic recirculation region is apparent

due to the interaction of northward flow south of the cape and the southward coastal jet. This cyclonic recirculation is also evident in velocity and temperature fields in Figure 45. This feature is located inshore of the recirculation region found in the mean depth-averaged velocity field (Figure 43).

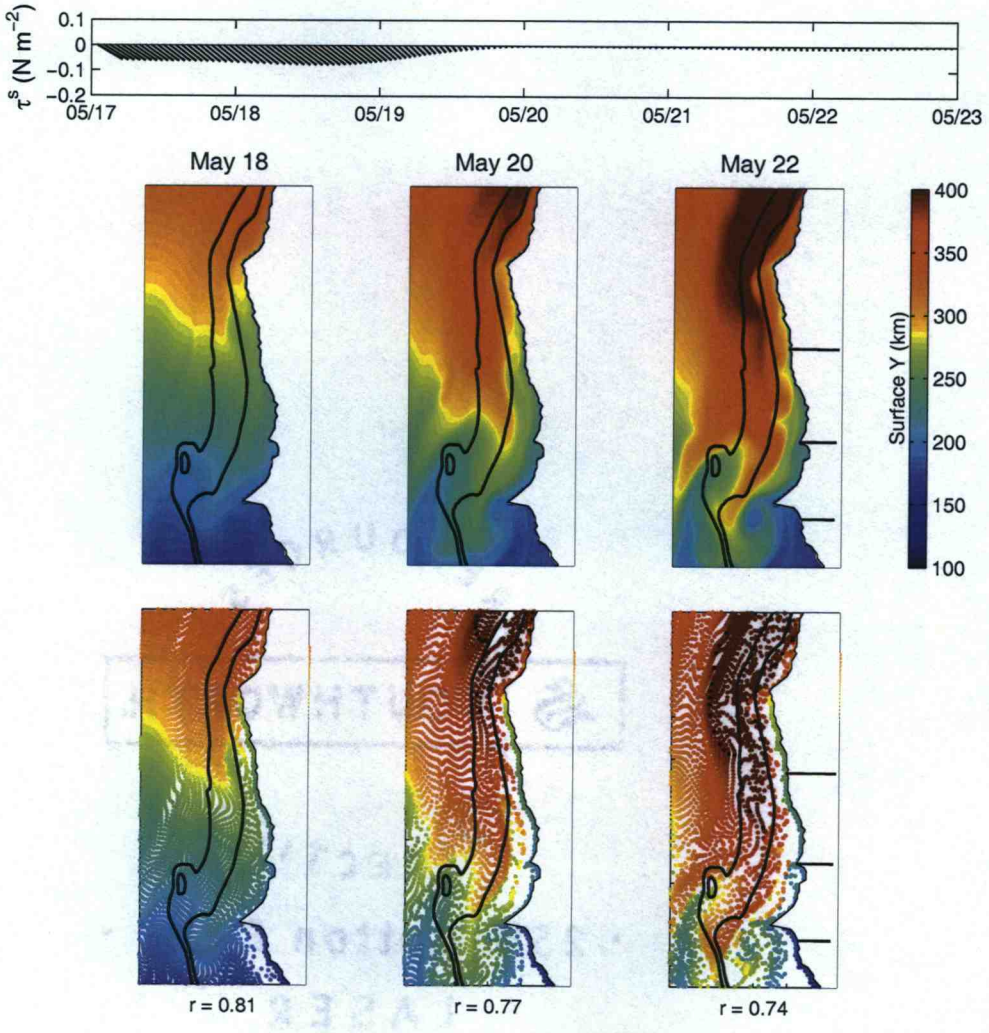

Figure 51. Surface Y Lagrangian label in km (top) and Lagrangian parcels (bottom) initialized on May 17 and plotted on May 18, 20, and 22. Spatial correlation coefficients between the labels and the parcels are given for each day at the bottom. The colorbar indicates values from 100 – 400 km, measured as distance from the southern boundary of the model domain. The initial Y values at the southern and northern boundaries of the region plotted are 150 km and 320 km, respectively. The locations of the A, D, and F lines are indicated in the right Y panel.

The evolution throughout the event is shown most clearly in the Y label fields, but the parcel tracking shows a very similar response. Spatial correlations between the Y label and the parcels computed at the parcel locations range from 0.99 on May 18 to 0.95 on May 22. The comparison in Figure 51 is evidence that the two techniques perform consistently and provides a quantitative check on the ability of the Lagrangian methods.

Depth-averaged values of the ΔX and ΔY Lagrangian label displacements and surface values of ΔZ are shown in Figure 52 during the event. The label displacements are calculated as $\Delta X(x,y,z,t) = X(x,y,z,t=0) - X(x,y,z,t)$, $\Delta Y(x,y,z,t) = Y(x,y,z,t=0) - Y(x,y,z,t)$, and $\Delta Z(x,y,z,t) = Z(x,y,z,t) - Z(x,y,z,t=0)$ where the time of initialization $t = 0$ corresponds to May 17. Recall that the X Lagrangian label is initialized as water depth (31) so that positive values of ΔX, ΔY, and ΔZ denote onshore, southward, and upward displacements, respectively. On May 18, the ΔY displacement is relatively small, but by May 20, areas of southward advection are found in the region of the coastal jet. ΔY values are small south of Pt. Reyes, due to the coastal jet separation, and are small inshore of the jet near the coast. Southward ΔY displacements increase significantly from May 20 to May 22, however the pattern remains much the same. A large region of onshore displacement (positive ΔX) just offshore of the 200-m isobath is apparent near the F line on May 18, with offshore displacement (negative ΔX) to the north and south. Velocity fields on May 16 and 17 (not shown) indicate evidence for a cyclonic eddy-like circulation south of Pt. Arena that weakens as the southward alongshelf currents intensify on May 18. Velocities along the F line are onshore at the southern edge of this eddy, apparently leading to the onshore displacement seen

in ΔX at this location. The negative regions just off the shelf break are caused by offshore velocities due to the coastal jet separation off Pt. Reyes and Pt. Arena. The positive ΔX patch is advected southward and distorted on May 20 – 22. Inshore of the 100-m isobath between Pt. Reyes and Pt. Arena, the ΔX values are generally positive, reflecting net onshore displacement.

Surface ΔZ shows upwelling of water from about 40 m depth in a few locations near the coast on May 18. Significantly more water from depth is found on May 20 and May 22, with initial depths greater than 60 m from the coast to about 10 km offshore everywhere north of Pt. Reyes. The response south of Pt. Reyes shows that the spatial pattern of upwelling is complex and extends offshore in response to the separated coastal jet, rather than being contained in a cohesive region near the coast, and that water upwells to the surface from shallower depths there than north of Pt. Reyes. Note the effects of the cyclonic recirculation south of Pt. Reyes discussed previously with reference to Figure 51. This feature is associated with upwelling of water from the north and offshore transport of water parcels (positive ΔY and ΔZ and negative ΔX).

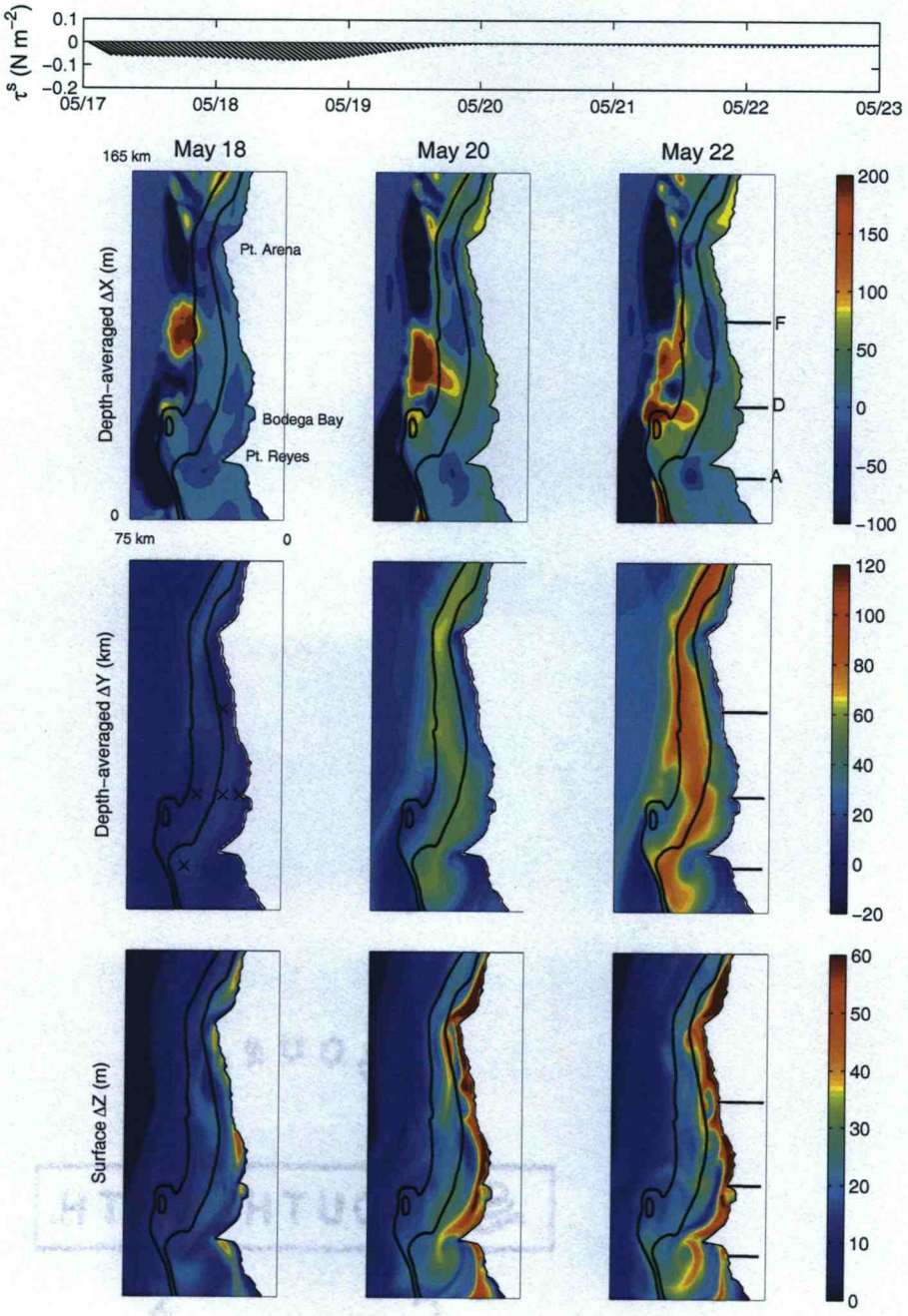

Figure 52. Depth-averaged Lagrangian label displacements ΔX (top) and ΔY (middle), and surface ΔZ (bottom) over the region from Pt. Reyes to Pt. Arena on May 18, 20, and 22. The differences ΔX, ΔY, and ΔZ are calculated as defined in the text so that positive values denote onshore, southward, and upward displacements, respectively. The locations of the A, D, and F lines are indicated in the right panels and the locations of the time series shown in Figures 54 and 55 are marked with a black $\times$ in the middle left panel.

A Lagrangian investigation corresponding to the discussion of Figures 49 and 50 in section 4.6.1 is presented with sections of all three Lagrangian label displacement fields along the A, D, and F lines during the upwelling and relaxation event (Figure 53). The ΔY Lagrangian label displacement shows a structure very similar to the alongshelf velocity, with the largest southward displacement corresponding to the jet location at all three sections. Upwelling of parcels occurs across the shelf, with upward displacements of up to 60 m in ΔZ. Offshore displacements indicated by negative ΔX occur in the region of the upwelling jet, with the largest values at the surface due to the surface Ekman flow, and decreasing values with depth. Large patches of onshore displacement are found on the shelf at the F line (148) on May 18 and at the D line (124) on May 22, corresponding to the feature discussed in Figure 52. At the A line (104), the region of offshore displacements is a striking feature that is clearly centered over the offshore upwelling jet core. The ΔX response at the A line is caused by the coastal jet separation off Pt. Reyes, so that water in the jet is advected southward and offshore. Because the depth rapidly increases offshore of 100 m at the A line, the ΔX values are large just off the shelf break, although the actual offshore advection distance is 20 km or less. On the shelf at the A line, values of the label displacements are smaller than those at the D and F lines. A conclusion of the analysis of Figure 53 is that the source of upwelled water near the coast at the D and F lines is farther north and deeper than that at the A line, given the larger values of ΔY and ΔZ. Hence, water that is upwelled on the shelf just south of Pt. Reyes is from a more local source because the presence of the cape significantly impacts the upwelling dynamics through jet separation. As shown in Figure 49, the upwelling circulation that occurs at the A line is effective at bringing

more dense water to the surface across the entire shelf.

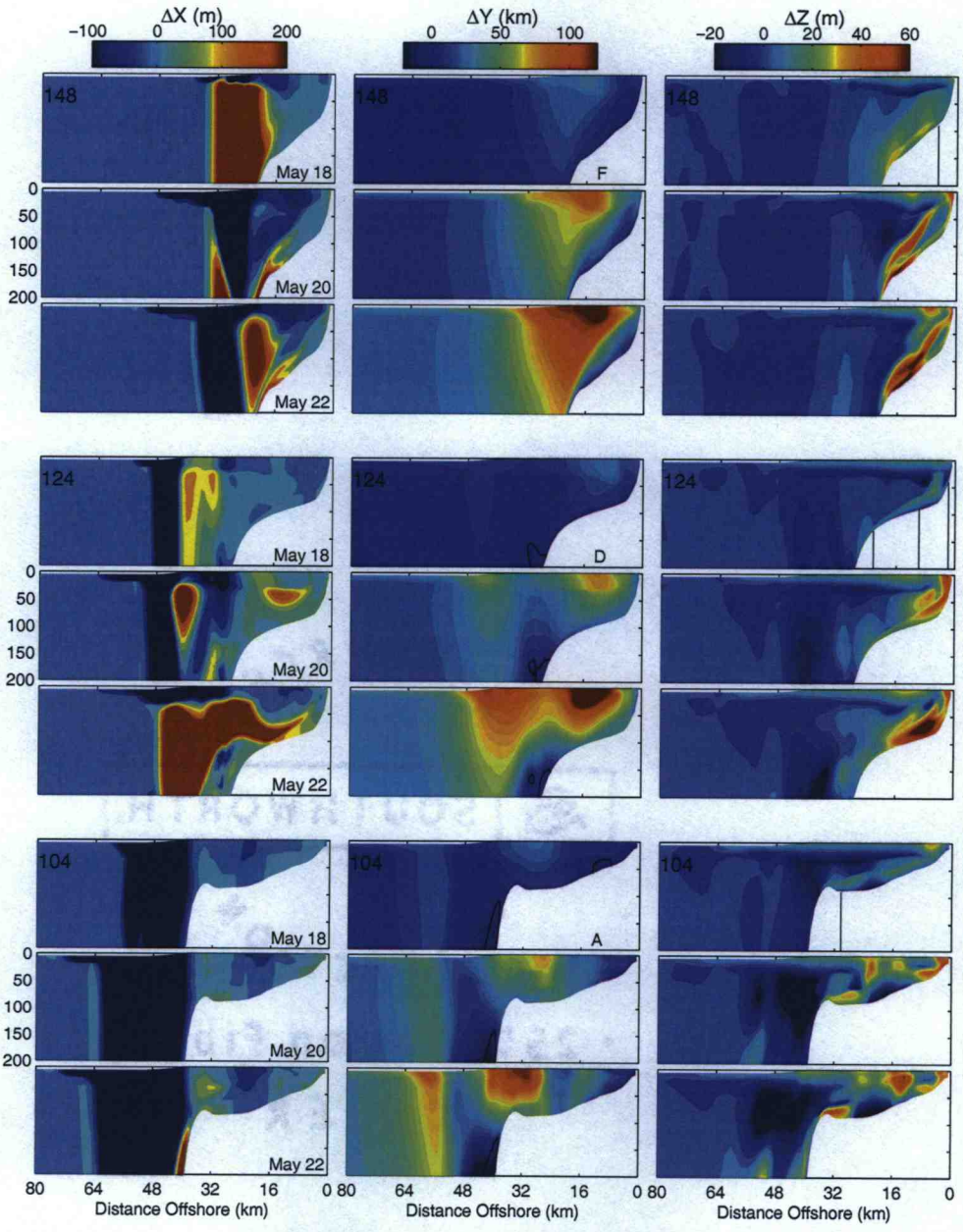

Figure 53. Sections of Lagrangian label displacements ΔX (left), ΔY (middle), and ΔZ (right) on May 18, 20, and 22. The differences ΔX, ΔY, and ΔZ are calculated as defined in the text so that positive values denote onshore, southward, and upward displacements, respectively. The section locations are the same as in Figure 49. The zero ΔY contour is shown in black. The locations of the D040, D090, and D130 time series plotted in Figure 54 and the A090 and F090 time series plotted in Figure 55 are shown as black lines in the far right column.

In order to further explore the question of how the Lagrangian dynamics vary as a function of across-shelf distance, we plot contours of all three Lagrangian label displacements, as well as v and σ_θ, as a function of depth and time during the event at the D line moorings (Figure 54). Significant upwelling of deeper and more dense water from about 40 km to the north occurs at D040. At D090, upwelling of water from about 80 km to the north occurs but the deeper water does not surface as at D040. The appearance of water from offshore is seen in ΔX at 40 m depth on May 19. This patch of offshore water corresponds to a small positive ΔX region at the D line on May 20 in Figure 53 and the onshore spreading of the large positive ΔX region in Figure 52. The water appears to be upwelled, as shown by its location at the upper edge of the upwelled water in ΔZ. With regard to Lagrangian displacements, the upwelling response at D090 is clearly more complex than at D040.

At D130, there are distinct contrasts with the inshore moorings. Noticeable upwelling is not evident in either ΔZ or σ_θ, but further evidence of the onshore patch of water discussed previously is found. ΔX shows that water from offshore (and 100 km to the north as shown by ΔY) is advected into the site at 40 m depth on May 21 and displaced downward to 100 m depth by May 23. Because there is no corresponding signal in ΔZ, this water is not upwelled from depth.

A final illustration of the alongshelf variability of the Lagrangian characteristics is provided by time series of v, σ_θ, ΔX, ΔY, and ΔZ at 90 m depth along the A and F lines (Figure 55). The alongshelf velocity v is weaker than at D090, especially at the F line, where v is near zero below about 20 m over much of the event period. Deeper isopycnals reach the surface at 90 m depth at the F line than at the D line, but upwelling in the isopycnals at the A line is much less evident. The A090 location

is on the edge of the density front, just inshore of the signature of Cordell Bank (see Figure 49). The density front is farther offshore at the A line than at the northern lines, as discussed previously. Thus, upwelling occurs over much of the shelf region at the A line (Figures 52 and 53), but the evolution throughout the event is relatively weak at this 90-m location. The structure of the ΔY time series is similar at all three locations, especially at the A and D lines. Note that the location of A090 is offshore of the region of locally upwelled water on the A line discussed previously and it shows a significant signal in ΔY. While ΔY displacements are comparable between the A, D, and F lines during the event, the ΔX and ΔZ responses are quite different. ΔZ displacements are generally complex at all three locations. ΔZ shows that water at depth after May 19 is upwelled from shallower depths on the F line as compared to the A and D lines. As shown in Figure 53, deep water is upwelled at F, however it doesn't reach as far inshore. ΔX shows that significantly less across-isobath motion occurs at 90-m depth at the A and F lines than at the D line. The A and F lines do not show evidence at 90 m of the large patch of onshore-displaced water that is prevalent at the D line in Figures 52, 53, and 54.

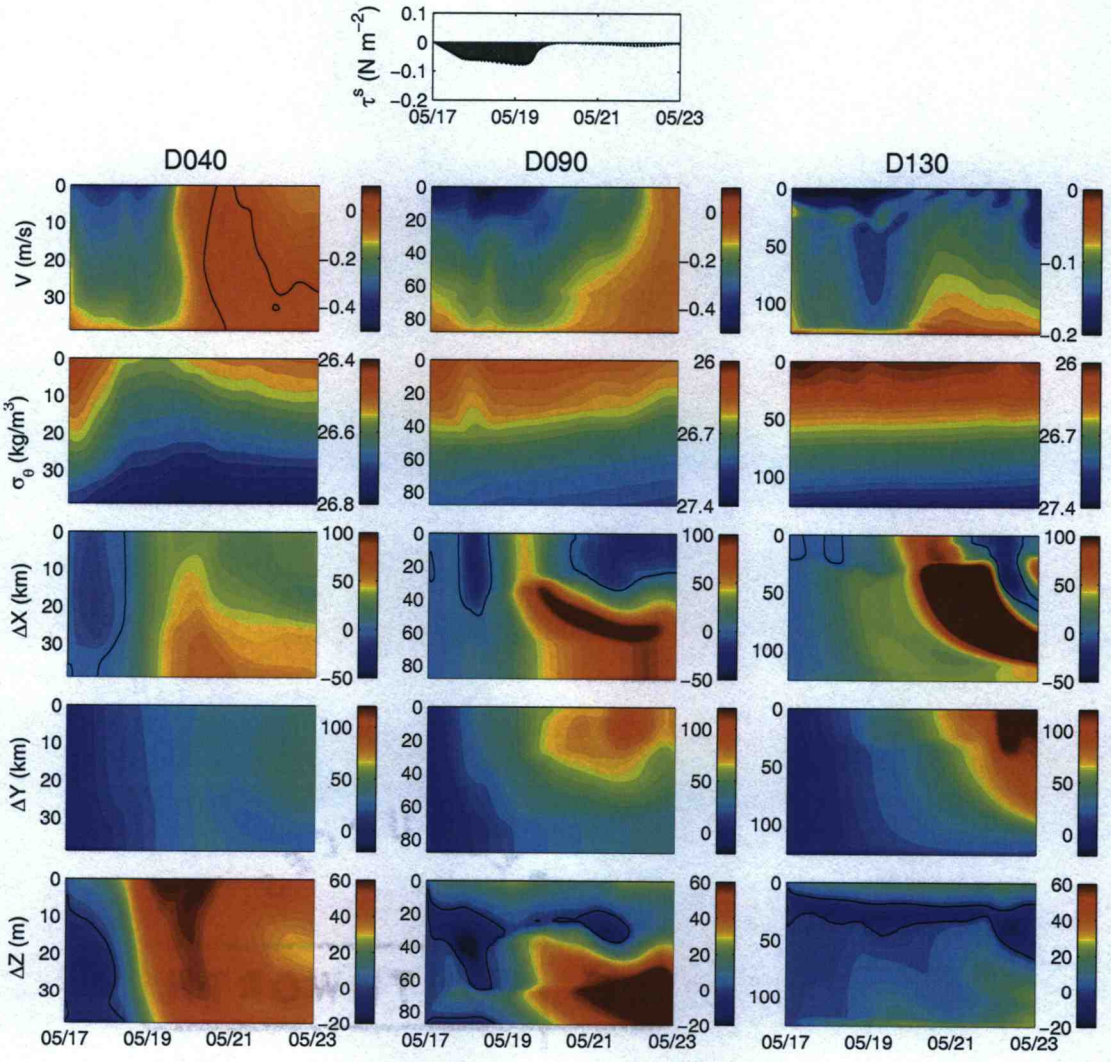

Figure 54. Time series of v (row 1), σ_θ (row 2), Lagrangian label displacements ΔX (row 3), ΔY (row 4), and ΔZ (row 5) at the D line moorings from May 17 – 23. Zero contours are shown in black.

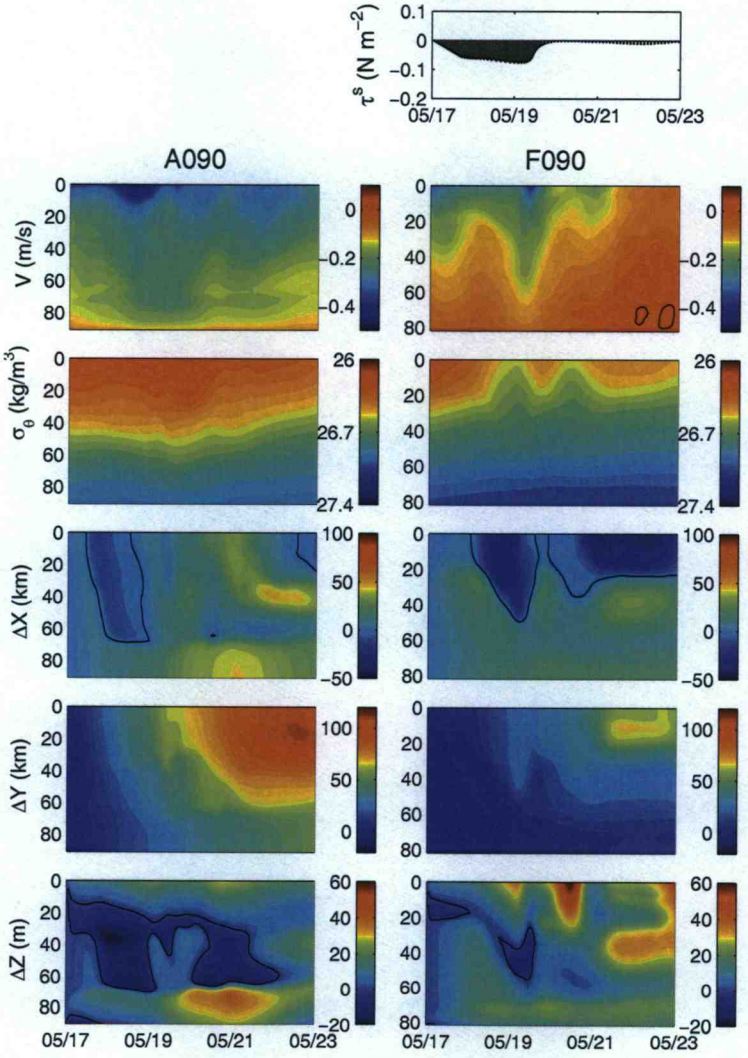

Figure 55. Time series of v (row 1), σ_θ (row 2), Lagrangian label displacements ΔX (row 3), ΔY (row 4), and ΔZ (row 5) at 90 m depth along the A line (left) and the F line (right) from May 17 – 23. Zero contours are shown in black.

The main results from the three-dimensional Lagrangian analysis discussed in this section are summarized here. The influence of the double jet structure on the southward displacement of parcels over the shelf is clearly shown to produce greater southward displacement along the 100-m isobath and offshore of Cordell Bank. Directly over the bank and near the coast, southward displacement is decreased. Alongshelf variability in fluid parcel displacement is also introduced by the presence of Pt. Arena and Pt. Reyes. Offshore of these capes, parcels are advected off the shelf due to the offshore-directed velocities associated with the separation of the coastal upwelling jet. A cyclonic recirculation feature detected south of Pt. Arena prior to the event discussed leads to a large patch of onshore-displaced parcels that first appears near the F line and is displaced southward and distorted in time. This behavior shows directly that eddy-like structures that develop in the coastal jet as a result of flow-topography interactions can have a significant impact on across-shelf transport. South of Pt. Reyes, the upwelling response of the fluid parcels contrasts from that north of Pt. Reyes in that water upwelled near the coast is from a more local source and the spatial pattern of upwelling is variable rather than occurring in a defined region near the coast. Across-shelf variability in the response of water parcels along the D line is also evident, including decreased vertical displacement of upwelled water parcels and increased southward displacement of parcels in the offshore direction.

4.7 Summary

We have presented a modeling application using the Regional Ocean Modeling System (ROMS) with the objective of studying and understanding the wind-driven

flows off Northern California in the region of the Wind Events and Shelf Transport (WEST) project. In this modeling effort, we set out to answer questions about flow variability across and along the shelf, flow complexities introduced by Cordell Bank, and the source of upwelled water in the region. To address these questions, we used both an Eulerian and a Lagrangian approach and focused analysis on an upwelling and relaxation wind event that is representative of those occurring throughout the summer in this region.

Numerous model-data comparisons suggest that the model performs reasonably well in this region, with high correlations between modeled and measured depth-averaged velocities at the mooring locations, surface velocities in the CODAR region, and potential density along survey lines. A weakness of the model is the inability to fully capture the reversal of southward velocities that is observed following relaxation of upwelling winds.

The mean circulation over the period of May 5 – June 20, 2001 is dominated by an upwelling response, including a southward coastal jet of up to 1 m s^{-1} that separates from the coast off Pt. Arena and Pt. Reyes. The capes are regions of nonlinearity in the surface flow and significant turbulence near the bottom. Sections of alongshelf velocity at several locations reveal significant alongshelf variability and the existence of a distinct double jet structure that develops just north of Bodega Bay. Upstream influence of Cordell Bank is postulated to be the cause for this double jet.

With regard to the time variability of the flow, we have focused attention on a specific upwelling and subsequent relaxation wind event. Flows around Pt. Reyes show a different response north and south due to interactions of the shelf flow

with the highly variable coastline shape and shelf geometry. South of Pt. Reyes, the upwelling circulation is effective in bringing relatively cold, dense water to the surface over the entire shelf. Relaxation of upwelling winds causes the development of northward velocities south of Pt. Reyes and near the coast between Pt. Reyes and Pt. Arena. Depth-averaged momentum balance terms illustrate the importance of the alongshelf topographic and coastline variability in causing a negative nonlinear advection offshore of Pt. Reyes and Pt. Arena, balanced by positive ageostrophic pressure gradient. This pattern is due to the spatial acceleration of the velocity around the capes.

Variability in the across-shelf direction is also investigated through time series of the depth-averaged alongshelf momentum balance terms at the D line moorings. The response is similar at 90 m and 130 m, however at 40 m the dynamics are different as shown by the opposite sign of the nonlinear advection and ageostrophic pressure gradient terms resulting from the small cape structure of Bodega Head. Differences in the D090 time series and those at 90-m depth along the A and F lines again point to the importance of variability of the topography and coastline on the details of the depth-averaged momentum balance. At F090, a region with relatively similar topography along the shelf, the advection and ageostrophic pressure gradient terms are small compared to the wind stress, while at A090, just south of Pt. Reyes, these terms constitute the dominant balance.

The Lagrangian shelf characteristics and their relationship to the Eulerian fields throughout the wind event are also discussed. We show the upwelling and relaxation response at D040 is strong as compared to the offshore moorings using time series of v, σ_θ, and Lagrangian label displacements ΔX, ΔY, and ΔZ. The Lagrangian

displacement fields are a useful tool in determining the response of water parcels to upwelling wind forcing. Alongshelf sections and area maps of ΔX, ΔY, and ΔZ also show the source of upwelled water near the coast at the A line is local, as compared to that north of Pt. Reyes, which has a signature of deeper water from farther north. This result once again points to a fundamentally different upwelling response north and south of Pt. Reyes, and gives further evidence of the significance of the coastline shape in the behavior of the shelf flow.

4.8 Acknowledgments

This research was supported by the National Science Foundation Coastal Ocean Processes (CoOP) program under grant OCE-9907854. The authors are grateful to the WEST program investigators for valuable interactions and specifically to E. Dever, D. Kaplan, and N. Garfield for making their data available for model comparisons. In particular, we thank E. Dever for insightful discussions of shelf circulation processes in the WEST region. We also thank J. Barth, R. Miller, and R. Samelson for helpful comments.

4.9 References

Alessi, C.A., S.J. Lentz, and R.C. Beardsley, 1991: Shelf Mixed Layer Experiment (SMILE) Program Description and Coastal and Moored Array Data Report, *Tech. Rep. WHOI-91-39*, Woods Hole Oceanogr. Inst., Woods Hole, MA.

Barnier, B., P. Marchesiello, A. Pimenta de Miranda, M. Coulibaly, and J.M. Molines, 1998: A sigma-coordinate primitive equation model for studying the circulation in the South Atlantic, Part I: Model configuration with error estimates, *Deep Sea Res., Part I*, **45**, 543-572.

Beardsley, R.C., E.P. Dever, S.J. Lentz, and J.P. Dean, 1998: Surface heat flux variability over the northern California shelf, *Journal of Geophysical Research*, **103**, 21553-21586.

Beardsley, R.C., C.E. Dorman, C.A. Friehe, L.K. Rosenfeld, and C.D. Winant, 1997: Local atmospheric forcing during the Coastal Ocean Dynamics Experiment, 1. A Description of the marine boundary layer and atmospheric conditions over a northern California upwelling region, *Journal of Geophysical Research*, **92**, 1467-1488.

Beardsley, R.C. and S.J. Lentz, 1987: The Coastal Ocean Dynamics Experiment collection: An introduction, *J. Geophys. Res.*, **192**, 1455-1463.

Beckmann, A. and D.B. Haidvogel, 1993: Numerical simulation of flow around a tall isolated seamount, Part I: Problem formulation and model accuracy, *J. Phys. Oc.*, **23**, 1736-1753.

Chapman, D.C., 1985: Numerical treatment of cross-shelf open boundaries in a barotropic coastal ocean model, *J. Phys. Oc.*, **15**, 1060-1075.

Dever, E.P., C.E., Dorman, and J.L. Largier, 2004: Surface boundary layer variability during upwelling off northern California (in preparation).

Dorman, C.E. and C.D. Winant, 1995: Buoy observations of the atmosphere along the west coast of the United States, 1981-1990, *J. Geophys. Res.*, **100**, 16029-16044.

Galperin, B., L.H. Kantha, S. Hassid, and A. Rosati, 1988: A quasi-equilibrium turbulent energy model for geophysical flows, *J. Atmos. Sci.*, **45**, 55-62.

Gan, J. and J.S. Allen, 2002a: A modeling study of shelf circulation off northern California in the region of the Coastal Ocean Dynamics Experiment: Response to relaxation of upwelling winds, *J. Geophys. Res.*, **107**, 3123, doi:10.1029/2000JC000768.

Gan, J. and J.S. Allen, 2002b: A modeling study of shelf circulation off northern California in the region of the Coastal Ocean Dynamics Experiment 2. Simulation and comparisons with observations, *J. Geophys. Res.*, **107**, 3184, doi:10.1029/2001JC001190.

Huyer, A, 1984: Hydrographic Observations along the CODE Central Line off Northern California, 1981, *J. Phys. Oc.*, **14**, 1647-1658.

Kuebel Cervantes, B.T. and J.S. Allen, 2003: A Modeling Study of Eulerian and Lagrangian Aspects of Shelf Circulation off Duck, North Carolina, *J. Phys. Oc.*, **33**, 2070-2092.

Largier, J.L., 2004: Wind Events and Shelf Transport, WWW Page, http://www.ccs.ucsd.edu/coop/west.

Mellor, G.L, T. Ezer, and L.-Y. Oey, 1994: The pressure gradient conundrum of sigma coordinate ocean models, *J. Atmos. Oceanic Technol.*, **11**, 1126-1134.

Mellor, G.L. and T. Yamada, 1982: Development of a Turbulence Closure Model for Geophysical Fluid Problems, *Rev. Geophys. and Space Phys.*, **20**, 851-875.

Shchepetkin, A.F. and J.C. McWilliams, 1998: Quasi-monotone advection schemes based on explicit locally adaptive dissipation, *Mon. Wea. Rev.*, **126**, 1541-1580.

Shchepetkin, A.F. and J.C. McWilliams, 2003: A method for computing horizontal pressure-gradient force in an oceanic model with a nonaligned vertical coordinate, *J. Geophys. Res.*, **108**, 3090, doi:10.1029/2001JC001047.

Shchepetkin, A.F. and J.C. McWilliams, 2004: The regional oceanic modeling system (ROMS): a split-explicit, free-surface, topography-following-coordinate oceanic model, *Ocean Modeling*, in press, doi:10.1016/j.ocemod.2004.08.002.

Song, Y.T. and D.B. Haidvogel, 1994: A semi-implicit ocean circulation model using a generalized topography-following coordinate system, *J. Comp. Phys.*, **115**, 228-244.

5 Summary

Wind-driven continental shelves are regions of high biological productivity because upwelling brings nutrient-rich waters to the surface. Thus, the importance of understanding the dynamics of the coastal ocean is recognized as an interdisciplinary problem. This has led to the organization of large observational efforts, including CoOP ISS and CoOP WEST, which are discussed here. Both studies had primary goals of learning how physical processes impact productivity and distribution of lower trophic level species on continental shelves.

The numerical modeling studies presented in this dissertation focus on the regions of interest in the ISS and WEST projects and address questions that the observational programs were set up to answer. Chapter 2 presents the two-dimensional upwelling and downwelling responses forced by real ISS winds during both stratified (August) and unstratified (October) conditions. The two periods show contrasting results due to different forcing and stratification. The nonlinear advection terms contribute significantly to the alongshelf momentum balance in depths less than 10 m during upwelling, but not during downwelling. Downwelling events during October are also characterized by a decreased transport relative to the theoretical Ekman transport in the surface and bottom layers. The dynamics of a strong downwelling event during 4–5 September are discussed in detail and shown to be in general agreement with those from the idealized modeling study of Austin (1998).

A Lagrangian label advection technique is also introduced in Chapter 2 and utilized to obtain information about the three-dimensional Lagrangian characteristics of the modeled flows. The Lagrangian label fields compare reasonably well to a parcel

tracking technique for the mean motion over the months of August and October. The results show significant advection in all three dimensions and complicated patterns during August due to fluctuating alongshelf winds. This conclusion motivates further investigation in Chapter 3 of the Lagrangian characteristics of two-dimensional flows forced by periodic alongshelf winds. The fluid parcel paths over a period show features from both the upwelling and downwelling forcing phases, as do the mean Eulerian velocities. Asymmetries between upwelling and downwelling surface and bottom layer thicknesses produce clear signals in the parcel paths.

The periodicity of the forcing allows for the technique of iterating the one-period parcel displacement map for many periods. By following the progression of maps initialized at different times in the forcing period, the displacements of parcels in different regions of the shelf are determined. The complexity of the Lagrangian motion near the coast, which is apparent after just one period, is quantified by calculation of the largest Lyapunov exponent from the map. This complicated region is characterized by a Lyapunov exponent greater than one and is clearly separated from a more regular surface cell feature offshore.

Chapter 4 encompasses a three-dimensional modeling study of the wind-driven flow in the region of the CoOP WEST experiment. The model is forced by observed winds and heat flux for the summer 2001 period. An extensive comparison of modeled fields to the WEST observations shows reasonably high correlations that vary with shelf location. The mean circulation is dominated by the upwelling response, with a surface-intensified coastal jet that separates from the coast off Pt. Reyes and less significantly off Pt. Arena. Just north of Bodega Bay, a double jet develops and strengthens to the south.

The primary focus of Chapter 4 is the discussion of the shelf response to an upwelling and subsequent relaxation wind event. Flows around Pt. Reyes are complex and show a different response north and south due to interactions of the shelf flow with the highly variable coastline shape and shelf geometry. South of Pt. Reyes, upwelling is effective and brings cold, dense water to the surface over the entire shelf. Depth-averaged momentum balance terms illustrate the importance of the alongshelf topographic and coastline variability in causing a negative nonlinear advection offshore of Pt. Reyes and Pt. Arena, balanced by positive ageostrophic pressure gradient. This pattern is due to the spatial acceleration of the velocity around the capes and the ageostrophic pressure gradient is intensified by an associated decrease in surface elevation south of the capes.

Area maps of Lagrangian label displacements ΔX, ΔY, and ΔZ show the effect of the coastal jet separation off Pt. Reyes on water parcel motion. Combined with alongshelf sections of the label displacements, the maps also reveal that the source of upwelled water near the coast at the A line is local, as compared to that north of Pt. Reyes, which has a signature of deeper water from farther north. This result once again points to a fundamentally different upwelling response north and south of Pt. Reyes, and gives further evidence of the significance of the coastline shape in the behavior of the shelf flow.

Across-shelf variability of the Eulerian and Lagrangian fields is also investigated. Time series of the depth-averaged alongshelf momentum balance terms on the D line show the response is similar at 90 m and 130 m, however at 40 m the dynamics are different as shown by the opposite sign of the pressure gradient and advection terms. This is due to the small cape structure at the north end of Bodega Bay.

Also at D040, the upwelling and relaxation response is stronger and less complex than at the offshore moorings, illustrated with time series of v, σ_θ, and the three Lagrangian labels. The Lagrangian dynamics throughout the event are discussed as they relate to the Eulerian upwelling and relaxation response. As in Chapters 2 and 3, the two Lagrangian techniques employed in Chapter 4 prove to be a useful tool in determining the response of water parcels to upwelling wind forcing.

Bibliography

Alessi, C.A., S.J. Lentz, and R.C. Beardsley, 1991: Shelf Mixed Layer Experiment (SMILE) Program Description and Coastal and Moored Array Data Report, *Tech. Rep. WHOI-91-39*, Woods Hole Oceanogr. Inst., Woods Hole, MA.

Alessi, C.A., S.J. Lentz, and J. Austin, 1996: Coastal Ocean Processes Inner-Shelf Study: Coastal and moored physical oceanographic measurements, *Tech. Rep. WHOI-96-06*, Woods Hole Oceanogr. Inst., Woods Hole, MA, 142 pp.

Allen, J.S., P.A. Newberger, and J. Federiuk, 1995: Upwelling circulation on the Oregon continental shelf, Part I: Response to idealized forcing, *J. Phys. Oceanogr.*, **25**, 1867-1889.

Allen, J.S. and P.A. Newberger, 1996: Downwelling circulation on the Oregon continental shelf, Part I: Response to idealized forcing, *J. Phys. Oceanogr.*, **26**, 2011-2035.

Austin, J.A., 1998: Wind-driven Circulation on a Shallow, Stratified Shelf, *Ph.D. Thesis*, MIT/WHOI, 246 pp.

Austin, J.A., 1999: The role of the alongshore wind stress in the heat budget of the North Carolina inner shelf, *J. Geophys. Res.*, **104**, 18,187-18,203.

Austin, J.A. and S.J. Lentz, 1999: The relationship between synoptic weather systems and meteorological forcing on the North Carolina inner shelf, *J. Geophys. Res.*, **104**, 18,159-18,185.

Austin, J.A. and S.J. Lentz, 2002: The Inner Shelf Response to Wind-driven Upwelling and Downwelling, *J. Phys. Oceanogr.*, **32**, 2171-2193.

Barnier, B., P. Marchesiello, A. Pimenta de Miranda, M. Coulibaly, and J.M. Molines, 1998: A sigma-coordinate primitive equation model for studying the circulation in the South Atlantic, Part I: Model configuration with error estimates, *Deep Sea Res., Part I*, **45**, 543-572.

Beardsley, R.C., E.P. Dever, S.J. Lentz, and J.P. Dean, 1998: Surface heat flux variability over the northern California shelf, *Journal of Geophysical Research*, **103**, 21553-21586.

Beardsley, R.C., C.E. Dorman, C.A. Friehe, L.K. Rosenfeld, and C.D. Winant, 1997: Local atmospheric forcing during the Coastal Ocean Dynamics Experiment, 1. A Description of the marine boundary layer and atmospheric conditions over a northern California upwelling region, *Journal of Geophysical Research*, **92**, 1467-1488.

Beardsley, R.C. and S.J. Lentz, 1987: The Coastal Ocean Dynamics Experiment collection: An introduction, *J. Geophys. Res.*, **192**, 1455-1463.

Beckmann, A. and D.B. Haidvogel, 1993: Numerical simulation of flow around a tall isolated seamount, Part I: Problem formulation and model accuracy, *J. Phys. Oc.*, **23**, 1736-1753.

Benettin, G., L. Galgani, and J.M. Strelcyn, 1976: Kolmogorov entropy and numerical experiments, *Phys. Rev. A*, **14**, 2338-2345.

Blumberg, A.F. and G.L. Mellor, 1987: A Description of a Three-Dimensional Coastal Ocean Circulation Model, *Three-Dimensional Coastal Ocean Models*, Coastal and Estuarine Science Series, Vol. 4, N. Heaps Ed., Amer. Geophys. Union, 1-16.

Bray, N.A. and C.L. Greengrove, 1993: Circulation over the shelf and slope off northern California, *J. Geophys. Res.*, *98*, 18119-18146.

Brink, K.H. and T.J. Cowles, 1991: The Coastal Transition Zone Program, *J. Geophys. Res.*, **96**, 14637-14648.

Butman, C.A., 1994: CoOP: Coastal Ocean Processes Study - Interdisciplinary approach, new technology to determine coupled biological, physical, geological processes affecting larval transport on inner shelf, *Sea Technol.*, **35**, 44-49.

Chapman, D.C., 1985: Numerical treatment of cross-shelf open boundaries in a barotropic coastal ocean model, *J. Phys. Oc.*, **15**, 1060-1075.

Chen, C. and R.C. Beardsley, 1998: Tidal mixing and cross-frontal particle exchange over a finite amplitude asymmetric bank: A model study with application to Georges Bank, *J. Mar. Res.*, **56**, 1163-1201.

Coulliette, C. and S. Wiggins, 2001: Intergyre transport in a wind-driven, quasigeostrophic double gyre: An application of lobe dynamics, *Nonlin. Proc. Geophys.*, **8**, 69-94.

Dever, E.P., 1997: Wind-Forced Cross-Shelf Circulation on the Northern California Shelf, *J. Phys. Oceanogr.*, **27**, 1566-1580.

Dever, E.P., C.E., Dorman, and J.L. Largier, 2004: Surface boundary layer variability during upwelling off northern California (in preparation).

Dorman, C.E. and C.D. Winant, 1995: Buoy observations of the atmosphere along the west coast of the United States, 1981-1990, *J. Geophys. Res.*, **100**, 16029-16044.

Federiuk, J. and J.S. Allen, 1995: Upwelling circulation on the Oregon continental shelf, Part II: Simulations and comparisons with observations, *J. Phys. Oceanogr.*, **25**, 1843-1866.

Galperin, B., L.H. Kantha, S. Hassid, and A. Rosati, 1988: A quasi-equilibrium turbulent energy model for geophysical flows, *J. Atmos. Sci.*, **45**, 55-62.

Gan, J. and J.S. Allen, 2002a: A modeling study of shelf circulation off northern California in the region of the Coastal Ocean Dynamics Experiment: Response to relaxation of upwelling winds, *J. Geophys. Res.*, **107**, 3123, doi:10.1029/2000JC000768.

Gan, J. and J.S. Allen, 2002b: A modeling study of shelf circulation off northern California in the region of the Coastal Ocean Dynamics Experiment 2. Simulation and comparisons with observations, *J. Geophys. Res.*, **107**, 3184, doi:10.1029/2001JC001190.

Haller, G., 2002: Lagrangian coherent structures from approximate velocity data, *Physics of Fluids*,**14**,1851-1861.

Huyer, A, 1984: Hydrographic Observations along the CODE Central Line off Northern California, 1981, *J. Phys. Oc.*, **14**, 1647-1658.

Ide, K., D. Small, and S. Wiggins, 2002: Distinguished hyperbolic trajectories in time-dependent fluid flows: analytical and computational approach for velocity fields defined as data sets, *Nonl. Proc. Geophys.*, **9**,237-263.

Kirwan, A.D., M. Toner, and L. Kantha, 2003: Predictability, uncertainty, and hyperbolicity in the ocean, *Int. J. Engin. Sci.*, **41**, 249-258.

Kuebel Cervantes, B.T., J.S. Allen, and R.M. Samelson, 2003: A Modeling Study of Eulerian and Lagrangian Aspects of Shelf Circulation off Duck, North Carolina, *Journal of Physical Oceanography*, **33**, 2070-2092.

Large, W.G. and S. Pond, 1981: Open Ocean Momentum Flux Measurements in Moderate to Strong Winds, *J. Phys. Oceanogr.*, **11**, 324-336.

Largier, J.L., 2004: Wind Events and Shelf Transport, WWW Page, http://www.ccs.ucsd.edu/coop/west.

Lentz, S.J., 2001: The Influence of Stratification on the Wind-Driven Cross-shelf Circulation over the North Carolina Shelf, *J. Phys. Oceanogr.*, **31**, 2749-2760.

Lentz, S.J., R.T. Guza, S. Elgar, F. Feddersen, and T.H.C. Herbers, 1999: Momentum balances on the North Carolina inner shelf, *J. Geophys. Res.*, **104**, 18,205-18,226.

Lentz, S.J. and J.H. Trowbridge, 1991: The bottom boundary layer over the northern California shelf, *J. Phys. Oc.*, **21**, 1186-1201.

Lichtenberg, A.J. and M.A. Lieberman, 1983: *Regular and Stochastic Motion*, Springer-Verlag, New York, NY, 499 pp.

Loder, J.W., Y. Shen, and H. Ridderinkhof, 1997: Characterization of Three-Dimensional Lagrangian Circulation Associated with Tidal Rectification over a Submarine Bank, *J. Phys. Oc.*, **27**, 1729-1742.

Malhotra, N., I. Mezic, and S. Wiggins, 1998: Patchiness: A New Diagnostic for Lagrangian Trajectory Analysis in Time-Dependent Fluid Flows, *Int. J. Bifurcation and Chaos*, **8**, 1053-1093.

Mellor, G.L. and T. Yamada, 1982: Development of a Turbulence Closure Model for Geophysical Fluid Problems, *Rev. Geophys. and Space Phys.*, **20**, 851-875.

Mellor, G.L, T. Ezer, and L.-Y. Oey, 1994: The pressure gradient conundrum of sigma coordinate ocean models, *J. Atmos. Oceanic Technol.*, **11**, 1126-1134.

Miller, P.D., C.K.R.T. Jones, A.M. Rogerson, L.J. Pratt, 1997: Quantifying transport in numerically generated velocity fields, *Physica D*, **110**, 105-122.

Poje, A.C. and G. Haller, 1999: Geometry of Cross-Stream Mixing in a Double-Gyre Ocean Model, *J. Phys. Oc.*, **29**, 1649-1665.

Poje, A.C., M. Toner, A.D. Kirwan, and C.K.R.T. Jones, 2002: Drifter Launch Strategies Based on Lagrangian Templates, *J. Phys. Oc.*, **32**, 1855-1869.

Rennie, S.E., J.L. Largier, and S.J. Lentz, 1999: Observations of a pulsed buoyancy current downstream of Chesapeake Bay, *J. Geophys. Res.*, **104**, 18,227-18,240.

Ridderinkhof, H. and J.W. Loder, 1994: Lagrangian Characterization of Circulation over Submarine Banks with Application to the Outer Gulf of Maine, *J. Phys. Oc.*, **24**, 1184-1200.

Rom-Kedar, V., A. Leonard, and S. Wiggins, 1990: An analytical study of transport, mixing and chaos in an unsteady vortical flow, *J. Fluid Mech.*, **214**, 347-394.

Send, U., R.C. Beardsley, and C.D. Winant, 1987: Relaxation from upwelling in the Coastal Ocean Dynamics Experiment, *J. Geophys. Res.*, **92**, 1683-1698.

Shchepetkin, A.F. and J.C. McWilliams, 1998: Quasi-monotone advection schemes based on explicit locally adaptive dissipation, *Mon. Wea. Rev.*, **126**, 1541-1580.

Shchepetkin, A.F. and J.C. McWilliams, 2003: A method for computing horizontal pressure-gradient force in an oceanic model with a nonaligned vertical coordinate, *J. Geophys. Res.*, **108**, 3090, doi:10.1029/2001JC001047.

Shchepetkin, A.F. and J.C. McWilliams, 2004: The regional oceanic modeling system (ROMS): a split-explicit, free-surface, topography-following-coordinate oceanic model, *Ocean Modeling*, in press, doi:10.1016/j.ocemod.2004.08.002.

Smolarkiewicz, P.K., 1983: A Simple Positive Definite Advection Scheme with Small Implicit Diffusion, *Mon. Wea. Rev.*, **111**, 479-486.

Song, Y.T. and D.B. Haidvogel, 1994: A semi-implicit ocean circulation model using a generalized topography-following coordinate system, *J. Comp. Phys.*, **115**, 228-244.

Taylor, G.I., 1953: Dispersion of solute matter in solvent flowing slowly through a tube, *Proc. Roy. Soc.* (London), Series A, **219**, 186-203.

Taylor, G.I., 1954: The dispersion of matter in turbulent flow through a pipe, *Proc. Roy. Soc.* (London), Series A, **223**, 446-468.

Waldorf, B.W., J.L. Largier, S. Rennie, J. Austin, and C. Greengrove, 1995: Coastal Ocean Processes (CoOP) pilot project data report: R/V *Cape Hatteras* shipboard measurements; underway, CTD, and ADCP data August 1994, *Tech. Rep. SIO Ref. Ser. 95-29*, Scripps Inst. of Oceanogr., La Jolla, CA, 419 pp.

Waldorf, B.W., J.L. Largier, S. Rennie, and J. Austin, 1996: Coastal Ocean Processes (CoOP) pilot project data report: R/V *Cape Hatteras* shipboard measurements; underway, CTD, and ADCP data October 1994, *Tech. Rep. SIO Ref. Ser. 96-9*, Scripps Inst. of Oceanogr., La Jolla, CA, 407 pp.

Weiss, J.B. and E. Knobloch, 1989: Mass transport and mixing by modulated traveling waves, *Phys. Rev. A*, **40**, 2579-2589.

Wing, S.R., L.W. Botsford, J.L. Largier, and L.E. Morgan, 1995: Spatial structure of relaxation events and crab settlement in the northern California upwelling system, *Mar. Ecol. Prog. Ser.*, **128**, 199-211.